

The Martian Moon Phobos

A Geodetic Analysis of its Motion, Orientation, Shape, and
Physical Parameters

vorgelegt von
Diplom-Ingenieur
Konrad Willner
aus Herzberg/Elster

Von der Fakultät VI - Planen Bauen Umwelt
der Technischen Universität Berlin
zur Erlangung des akademischen Grades
Doktor der Ingenieurwissenschaften
Dr.-Ing.

genehmigte Dissertation

Promotionsausschuss:

Berichter: Prof. Dr. phil. nat. Jürgen Oberst
Berichter: Prof. Veronique Dehant

Tag der wissenschaftlichen Aussprache: 08. Juli 2009

Berlin 2009

D 83

Eidesstattliche Erklärung

Ich versichere, dass ich die vorliegende Dissertation selbstständig und nur unter Verwendung der angegebenen Quellen und Hilfsmittel angefertigt habe. Wörtlich oder dem Sinn nach aus anderen Werken entnommene Stellen sind unter Quellenangabe kenntlich gemacht.

Konrad Willner

Berlin im Dezember 2009

Acknowledgements

I would like to thank all my colleagues at the DLR Berlin, my friends and my family for the overwhelming support I received during the entire time of this study.

Special thanks go to Prof. Dr. Jürgen Oberst, who made this study possible and furthered the study through fruitful discussions. Also many thanks to Prof. Dr. Dr. Lothar Gründig for the support at the Technical University of Berlin.

I am grateful to Dr. Hauke Hussmann and Dipl.-Phys. Marita Wählich who helped never-tiring to improve the thesis during countless discussions.

This study was funded by the German Research Foundation (Deutsche Forschungsgemeinschaft).

To the greatest little boy

and

Suse

Kurzfassung

Mars wird von zwei Monden umkreist, Deimos und Phobos. Der größere, Phobos, umrundet Mars mit einem durchschnittlichen Abstand von ca. 6000 km über der Marsoberfläche, tief in dem Gravitationsfeld des Planeten.

Auf der Grundlage der neuen hochauflösenden Bilder des Super Resolution Channels (SRC) und der High Resolution Stereo Camera (HRSC), welche Teil der Europäischen Raummission Mars Express (MEX) sind, wurde eine eingehende Studie des unregelmäßig geformten Mondes Phobos durchgeführt, um offene Fragen seiner orbitalen Bewegung, seiner Form sowie physikalischer Kenngrößen zu klären.

Parameter von Bahnmodellen für Phobos wurden in Frage gestellt nachdem große Diskrepanzen zu astrometrischen Beobachtungen von Phobos festgestellt wurden. Aus Vorbeiflug-Bildern von Phobos und aus Beobachtungen von Phobos' Schatten auf der Marsoberfläche wurden in dieser Studie astrometrische Beobachtungen abgeleitet und ausgewertet. Ergebnisse der Schattenbeobachtungen zeigen eine weite Streuung mit großen Unsicherheiten im Vergleich zu den Bahnmodellen, während die Vorbeiflugbeobachtungen mit den Bahnmodellen innerhalb der Fehlergrenzen übereinstimmen. Die Kontinuität und Systematik der Differenzen zwischen Beobachtungen und Vorhersagen lassen darauf schließen, dass Phobos seiner vorhergesagten Position etwa 2 km voraus ist.

Basierend auf einem Kontrollpunktnetz wurde die Figur von Phobos mittels verschiedener Techniken – durch ein digitales Oberflächenmodell (DOM) und durch Kugelflächenfunktionen – modelliert. Die 665 Kontrollpunktkoordinaten im Phobos-festen Koordinatensystem wurden aus Beobachtungen in 53 SRC und 16 Viking Orbiter Bildern berechnet. Die Berechnung der Objektpunktkoordinaten erfolgte über einen Bündelblockausgleich mit einer durchschnittlichen Genauigkeit von ± 17 m. Das Kontrollnetz stellte sich als wichtiges Werkzeug zur Beobachtung der Amplitude der erzwungenen Libration – einer der Rotation von Phobos überlagerten Schwingung, die aufgrund von Interaktionen mit dem Gravitationsfeld des Mars und der unregelmäßigen Form entsteht – heraus.

Auf der Grundlage von Stereobildern der HRSC und von Viking Orbiter Bildern wurde ein globales DOM berechnet. SRC und Viking Bilder wurden genutzt, um eine genaue Karte von Phobos zu erstellen.

Zur Berechnung von physikalischen Kenngrößen wurden die Koeffizienten einer Kugelflächenfunktion anhand der Kontrollpunkte bis Grad und Ordnung 17 berechnet. Mittels des analytischen Ausdrucks wurden das Volumen, die mittlere Dichte und die Trägheitsmomente neu bestimmt. Ein Volumen von 5689 km^3 und eine dazu korrespondierende mittlere Dichte von $1,85 \text{ g/cm}^3$ wurden berechnet, welche in guter Übereinstimmung mit bisherigen Abschätzungen sind. Die Trägheitsmomente wurden anfänglich unter der Annahme einer homogenen Massenverteilung berechnet. Die Hauptträgheitsmomente können in Relation zu der Amplitude der erzwungenen Libration gesetzt werden, welche mit dem beobachteten Wert innerhalb der Fehlergrenzen überein stimmt.

Durch einfache Zwei-Schicht-Modelle konnte die modellierte Amplitude nur unter Annahme extremer Modellparameter mit der Beobachtung in Übereinstimmung gebracht werden. Dieses deutet auf eine komplexere Massenverteilung im Inneren von Phobos hin.

Abstract

Mars is accompanied by two small natural satellites. Deimos, the smaller of the two, is orbiting at a greater distance from Mars while Phobos revolves around the planet at a mean altitude of approximately 6,000 km with respect to the Martian surface, deep in the gravity field of the planet.

An in-depth study of the irregular shaped moon Phobos was commenced due to remaining questions on its orbital motion, shape, and physical parameters based on new high resolution images of the Super Resolution Channel (SRC) and the High Resolution Stereo Camera (HRSC) which are part of the European Mars Express Mission (MEX).

Parameters of ephemerides models were questioned after the finding of large discrepancies of Phobos' position to astrometric observations. During the course of this study astrometric measurements were made in fly-by images of Phobos and through observations of Phobos' shadow on the Martian surface. While results of the latter analysis led to largely scattered differences compared to orbit prediction models with high uncertainties, the fly-by observations were in agreement with the ephemerides models within the error bands. Offsets were rather consistent and systematic indicating that Phobos is ahead of its predicted position by approximately 2 km.

To be able to model the irregular shape of Phobos by means of different techniques – namely a digital terrain model and a model based on spherical harmonic functions – a new global control point network was established. The 665 object point coordinates with respect to the Phobos body-fixed coordinate frame were determined through observations in 53 SRC and 16 Viking Orbiter images. Coordinates of the object points were computed by means of a least-squares bundle block adjustment. The overall accuracy was estimated to be in the order of ± 17 m. The control network proved to be a valuable tool to observe the forced libration amplitude – a superimposed oscillation on the rotation of Phobos due to interactions between the irregularly shaped Phobos and the gravity field of Mars.

A global digital terrain model (DTM), which is based on stereo images of the HRSC and Viking Orbiter images, was computed and was used to ortho-rectify SRC and Viking images. Based on the ortho-rectified images an accurate map of Phobos was prepared.

Since the DTM representation of Phobos' shape is rather inefficient to obtain physical parameters, the coefficients of the surface spherical harmonic function to degree and order 17 were determined through the control point coordinates. The analytical expression for Phobos was used to re-estimate the volume, bulk density of Phobos and the moment of inertia tensor. A volume of 5689 km^3 and a corresponding bulk density of 1.85 g/cm^3 were determined. The results were in good agreement, but significantly improved accuracy compared to previous estimates of these values.

The moments of inertia were primarily computed assuming a homogeneous mass distribution within Phobos. The principle moments of inertia can be put in relation to the forced libration amplitude. The modeled forced libration amplitude agrees well with the observed value within its error bounds.

Applying simple two layer mass distribution models, exact agreement between observation and model of the forced libration amplitude could only be achieved assuming extreme model parameters. This suggests a more complex mass distribution within Phobos.

Contents

Kurzfassung	1
Abstract	2
1 Motivation	6
2 The Martian Moon Phobos	8
2.1 The Origin	8
2.2 The Orbit	8
2.3 The Figure	10
3 Missions to Mars	12
3.1 Missions to Phobos and Deimos	12
3.2 Camera Systems of Different Space Missions	14
3.2.1 The Viking Orbiter Cameras	14
3.2.2 The Mars Orbiter Camera	15
3.2.3 The High Resolution Stereo Camera	16
3.2.4 The Super Resolution Channel	17
4 Reference Systems and Tools	20
4.1 Time	20
4.2 Reference Frames	20
4.2.1 The Phobos Reference Frame	22
4.3 Surfaces and Maps	24
4.4 Planetary Image Data	24
4.5 Software	25
5 Astrometric Observations	27
5.1 Previous Astrometric Observations	27
5.2 Shadow Observations	28
5.2.1 Determination of the 3D - Coordinates	31
5.2.2 Determination of Time	31
5.2.3 Stellar Coordinates of Phobos	33
5.2.4 Reconstruction of the Shadow	34
5.2.5 Results - Shadow Observations	36
5.3 Fly-by Observations	37
5.3.1 Fly-by Images	37

5.3.2	Pointing Verification	38
5.3.3	Center of Mass Measurements	40
5.3.4	Results	42
5.4	Validation of Orbit Models	43
5.5	Secondary Results	45
6	Control Point Network on Phobos	47
6.1	Previous Control Networks	47
6.2	Determination of Control Point Coordinates	48
6.2.1	Available Image Data	48
6.2.2	Point Measurements	50
6.2.3	Computation of Coordinates	51
6.2.4	Results	52
7	Global Shape Model	55
7.1	Global Digital Terrain Model	56
7.1.1	Improving the Orientation	57
7.1.2	Matching	59
7.1.3	DTM Generation	62
7.1.4	Controlled Ortho-Image Mosaic and Global Map	65
7.2	Spherical Harmonic Function Model	66
7.2.1	Evaluation of the Data Set	67
7.2.2	Computation	68
7.2.3	Interpretation of the Coefficients	70
8	Physical Parameters of Phobos	72
8.1	Volume	72
8.2	Bulk Density	73
8.3	Moments of Inertia	74
8.3.1	Theory	74
8.3.2	Computation of the Tensor	75
8.4	Forced Libration Amplitude	77
8.4.1	Observation	77
8.4.2	Modeling	78
9	Discussion and Conclusions	81
9.1	Motion in the Orbit	81
9.2	Shape and Physical Parameters	82

9.3 Outlook	85
List of Abbreviations	86
List of Symbols	87
List of Figures	89
List of Tables	91
Bibliography	92
A Shadow Observations	100
B Astrometric Observations	101
C Coefficients of the Spherical Expansion Model	103
D Phobos Map	104

1 Motivation

Phobos is the larger of the two natural satellites of our neighboring planet Mars. Since its discovery Phobos' irregular shaped body and its motion in its orbit have been the subject of interest and analysis (Batson et al., 1992; Thomas et al., 1992). The origin of Phobos and the second Martian moon Deimos is still debated (Burns, 1992; Singer, 2007). However, it is anticipated that an in depth study of its long term motion may provide clues for its evolution and origin. Before an attempt to answer this question can be made, some properties of Phobos such as its interaction with the Martian gravity field, its mass and mass distribution should be significantly constrained.

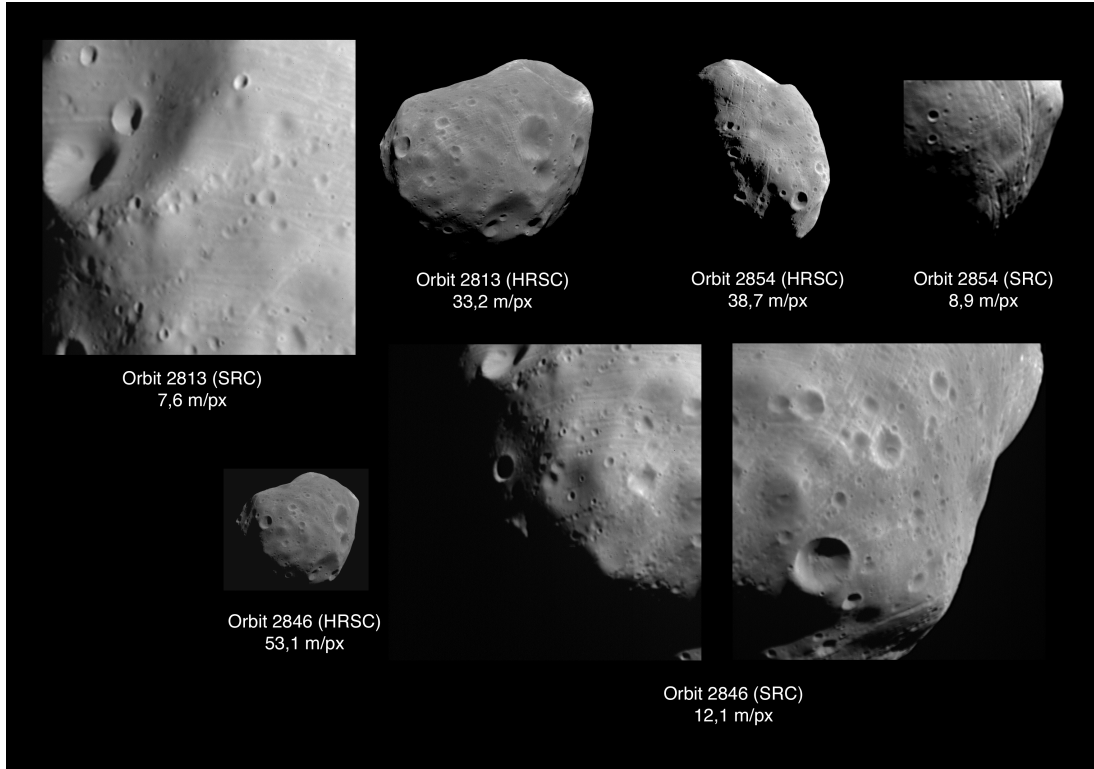


Figure 1: Samples of Phobos images obtained by the High Resolution Stereo Camera and Super Resolution Channel on Mars Express. Image resolutions vary due to different fly-by distances.

Recent observations of Phobos through the Super Resolution Channel (SRC) of the High Resolution Stereo Camera (HRSC) on board the European Mars Express (MEX) mission (see Fig. 1 for examples) provide an opportunity to determine some of these properties with better constraints as previous estimations.

This study covers three major topics – 1) the determination of Phobos' position in its orbit, 2) the computation of a global control point network, 3) the modeling of Phobos' shape. Solutions or results of each of these topics are used for further analysis to determine the desired information (cf. Figure 2).

A first goal of this study was to determine the difference between orbit models released in 2006 and 2007 (Jacobson and Rush, 2006; Lainey et al., 2007) and the observed position. To extend the observation period for long-term studies of Phobos' motion, observations of the Phobos shadow in the Mars Observer Camera (MOC) were considered as an independent control of Phobos' position against the stellar sky. Besides, fly-by observations obtained by the Super Resolution Channel of the HRSC were analyzed to obtain accurate positional information.

Primarily it was expected to be able to observe secular or temporal accelerations of Phobos in the results of the astrometric observations. The main perturbation effecting Phobos' orbit is the, possibly time variant, Martian $J_2(t)$ gravity coefficient. A long term observation of Phobos' position could allow to draw conclusions on the time variance of this coefficient. Furthermore, an improvement of the orbit prediction models was anticipated. Results of an orbit fit to astrometric observations – which was not scope of this study – often include solutions for gravity field coefficients, libration amplitudes and mass estimations for Phobos.

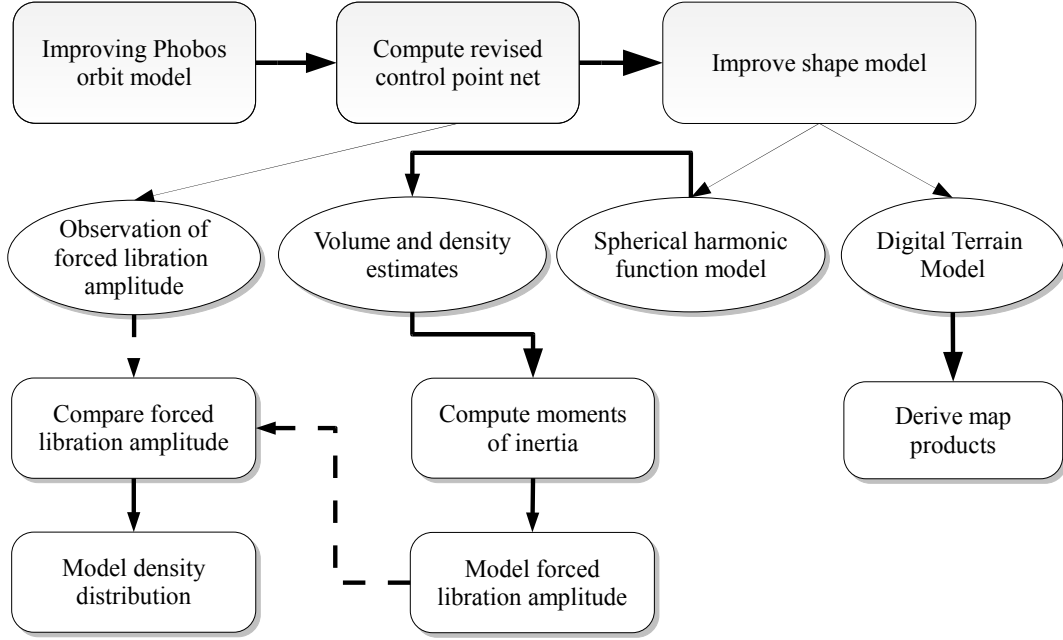


Figure 2: Outline of this study. Improved orbit prediction models allow for a more accurate Control point network analysis. The control point network can then in turn be used to determine properties of Phobos and to derive cartographic products through shape modeling.

Secondly, a global control point network was necessary to (a) observe the libration motion of Phobos and (b) to be able to derive improved shape models. The determination of the control point coordinates relied on improved orbit models.

In the third part of this study two different shape models were determined. For cartographic purposes a global digital terrain model was computed, based on HRSC stereo images and tied to the control point network. To determine physical parameters such as the volume, bulk density, and moments of inertia, coefficients of a spherical harmonic function were determined.

Space missions, imaging systems and special tools are described in the first part of this thesis. The subsequent sections deal with the three main components of this study (Fig. 2). These are the astrometric observations of Phobos, the determination of the global control point network and the modeling of the shape of Phobos. The improved physical parameters of Phobos', based on the results of this study, are described in a separate section. In the concluding summary results are discussed and an outlook is given.

2 The Martian Moon Phobos

The name of Mars has its origins in the Roman mythology, the God of Rome, which was later equated to the Greek god Ares, the god of war. The god of war is accompanied by two sons, fear - Phobos - and horror - Deimos, as is Mars symbolically by its two moons. The natural Martian satellite orbiting closer to Mars is called Phobos and the one orbiting at a greater distance is called Deimos (Fig 3).

Phobos and its smaller companion Deimos were discovered in 1877 by Asaph Hall, an astronomer at the United States Naval Observatory in Washington. Both are very irregular bodies. While Deimos is mostly only observed from greater distance by spacecraft due to its further distance to Mars, Phobos was observed from close range during many space missions launched to explore Mars.

2.1 The Origin

The origin of the Martian moons is still debated. Currently three possible theories to explain the origin of Phobos (and Deimos) have been proposed. The first is that the moons are captured satellites from the outer asteroid belt. This would agree to observable physical properties such as the albedo (Burns, 1992, and references therein). The spectral reflectivity of Phobos and asteroids from the outer asteroid belt are similarly low suggesting that it is originating from a region at 2.8 to 3.3 AU. However, according to dynamic models a capture and subsequent orbit evolution, leading to the currently observed orbit, can not be accomplished. To bring a hyperbolic orbit into a circular orbit, which happens during a capture, an energy loss is required. This is usually explained by aerodynamic drag caused by a nebula surrounding the planet shortly after it formed (Burns, 1992). However, as the drag changes the orbit rapidly, the question is, what prevented Phobos from moving too close to Mars? Only very special conditions would explain the capture. Thus, a second theory, according to the dynamical aspects, is a primordial formation close to the parent planet (Bursa et al., 1990) is the more likely origin of the Martian moons. A third possibility could be a capture of a larger object which was later fractioned with Phobos and Deimos being the remnants of this primary body. Singer (2007) argues that the two moons would be the smaller parts of the fractioning process.

2.2 The Orbit

The motion of Phobos and Deimos in their orbits has been studied for over 130 years by earth-based and spacecraft-based observations (Morley, 1989). While earth-based observations are only possible during Mars oppositions which occur approximately every second Earth year, greater opportunities to observe Phobos from close range via spacecraft data acquisition have greatly increased the available data to the scientific community in the recent past.

Orbit prediction models (further on also referred to as orbit models), which are fitted to observations of the body in its orbit, have been developed to ever greater accuracies such that the orbit model of Phobos is now one of the most accurate known in the solar system (Sinclair, 1989; Jacobson and Rush, 2006; Lainey et al., 2007).

However, in 1999 astrometric observations made from Mars lander vehicles and through remote sensing instruments on spacecraft exploring Mars revealed discrepancies between

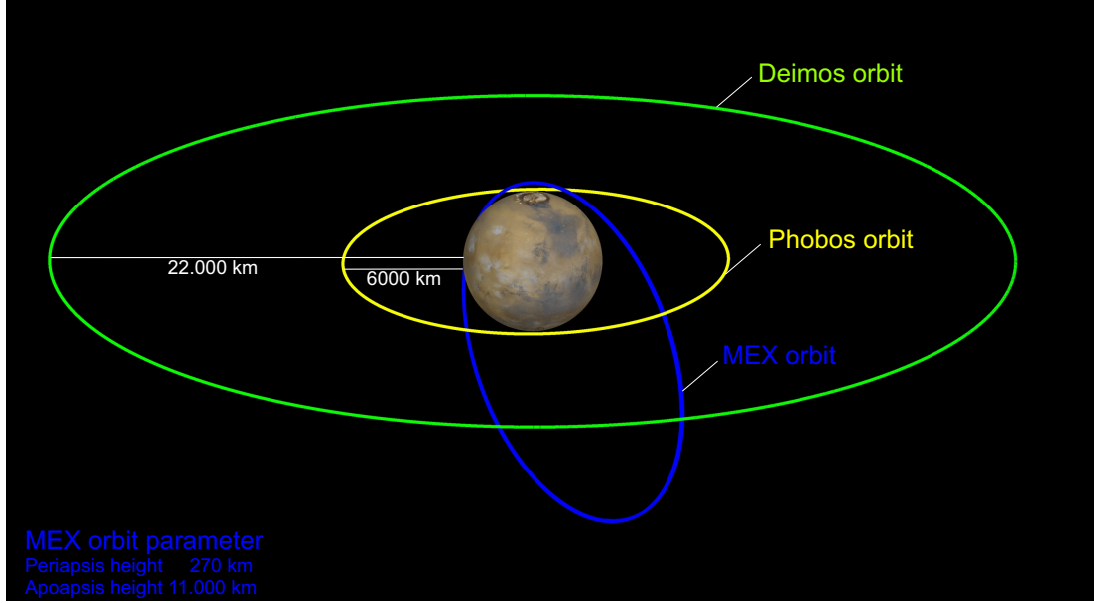


Figure 3: The orbits of Deimos, Phobos and Mars Express about Mars as in August 2008.

ephemeris tables and Phobos' observed position. Observations differed to orbit models between 5 and 12 km (Banerdt and Neumann, 1999; Thomas et al., 1999) attesting that Phobos was ahead of its predicted position.

Whilst discrepancies between orbit models and Phobos' observed position were subsequently confirmed (Neumann et al., 2004; Oberst et al., 2006), the reasons remain unclear. Phobos is orbiting Mars in a near circular, near equatorial orbit with an inclination of 1.075° with respect to the Martian equator (Table 1). The mean distance to the center of Mars is only 9375 km. It is dynamically tied to the gravity field of Mars and so physical and dynamical properties of Phobos may also constrain parameters of Mars. As a consequence, Phobos' motion in its orbit has been studied ever since its discovery (Morley, 1989). Especially the long-term orbital evolution is of interest to scientists since it may reveal seasonal changes in the gravity field parameters of Mars (Lainey et al., 2007; Lainey, 2007) (cf. Section 5).

Table 1: Estimates of Phobos' properties as currently published.

Property	Value
Mean Distance to Mars	9375 km
Radii ^a	$13.4 \times 11.2 \times 9.2$ km
GM ^b	$0.0007158 \pm 0.0000005 \text{ km}^3/\text{sec}^2$
Orbital period	7 h 39 min 14 sec
Eccentricity e	0.01515
Mean velocity absolute	2.14 km/sec
Mean velocity w.r.t. Mars	1.47 km/sec
Inclination i referred to Mars equator	1.075°

^a(Batson et al., 1992)

^b(Konopliv et al., 2006)

Similar to the Earth's moon Phobos is in a synchronous orbit about Mars. That indicates that the longest axis of Phobos points on average towards the center of Mars. However,

the gravity field of Mars in combination with Phobos' pronounced irregular shape (Figure 4) result in a forced libration motion of Phobos. The forced libration is an additional oscillating motion, superimposed on Phobos' rotation, which is caused by the interaction of Phobos' irregular body with the gravitation field of Mars. It should not be confused with the geometric libration, which is an effect due to different angular speeds of a body in its elliptical orbit and can also be observed at the Earth moon. The geometric libration amounts to two times the eccentricity of a body's orbit.

Phobos is in a prograde motion about Mars. Its orbital period is shorter than a Martian day. Hence, Phobos rises in the West and sets in the East when observing its motion from Mars.

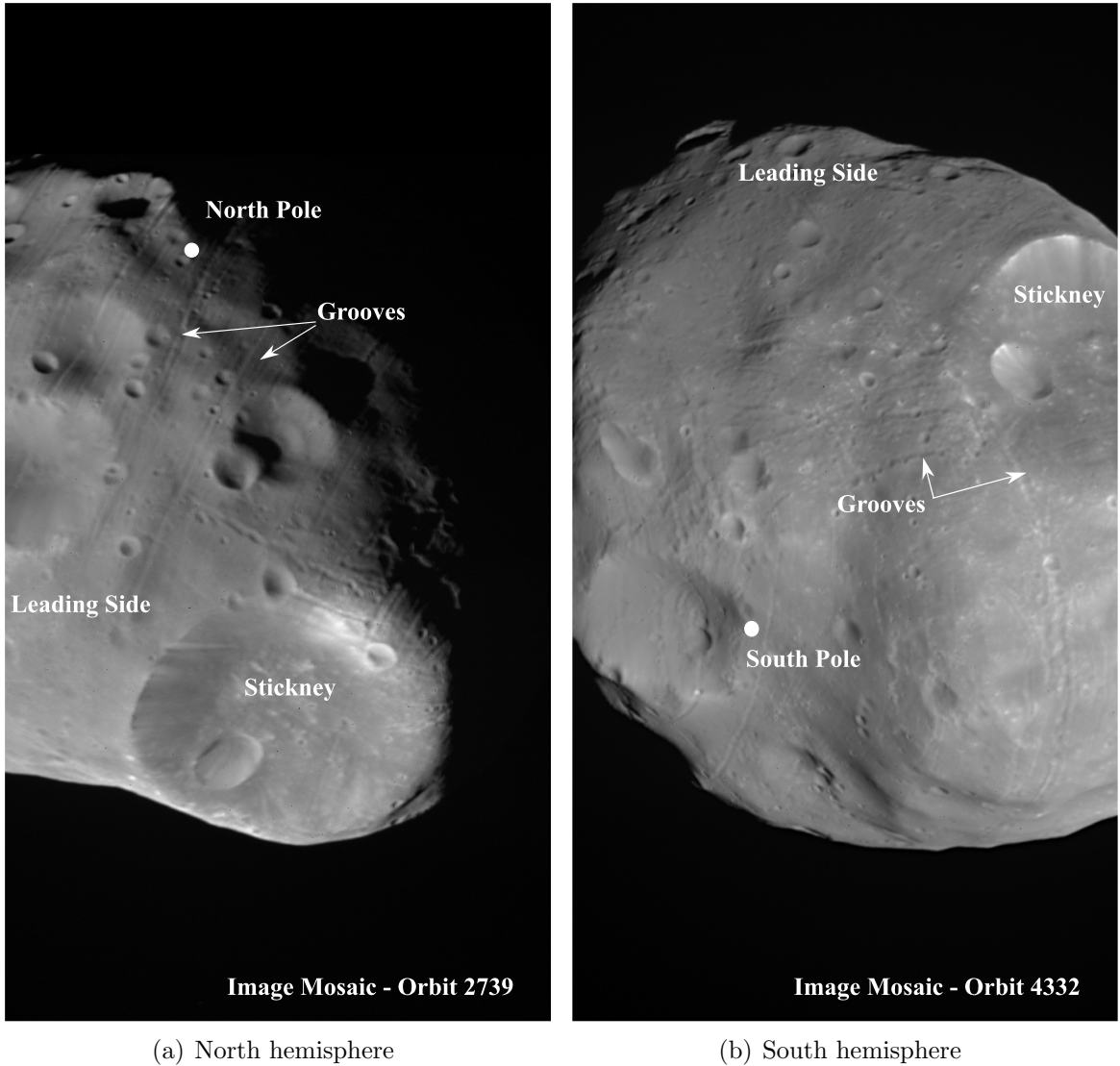


Figure 4: Views of Phobos as observed during different fly-bys.

2.3 The Figure

The leading face of Phobos is dominated by the Stickney crater (cf. Fig 4(a)). With a diameter of approximately 10 km and a depth of approximately 2 km Stickney is the largest crater on the $26.8 \text{ km} \times 22.4 \text{ km} \times 18.4 \text{ km}$ sized moon (see Table 1). Next to

large craters Phobos' surface is marked by deep grooves which are mainly located in the Northern hemisphere. These grooves are the most puzzling features on Phobos. Several possible explanations on the forming of the grooves have been published. Murray et al. (2006), for example, argues that crater chains and grooves may be formed by ejecta from Martian impacts. Wilson and Head (2005) discuss the possibility of groove forming through loose material, which was ejected during the forming of Stickney, rolling, sliding or bouncing across Phobos and thus crushing, pushing or moving the regolith aside. However, as these unique surface features, to date not observed on other objects, can be divided into several groups due to different morphologies and orientations, no model accounts for the formation of all different groups of grooves.

It is currently subject of debates whether Phobos is a rubble pile, it consists of very porous material but has a homogeneous mass distribution, or parts of Phobos are of lower density or are voids. Previous analysis led to the conclusion that Phobos has a homogeneous mass distribution (Duxbury, 1991). The estimates for the bulk density of 1.9 g/cm^3 (Avanesov et al., 1989) and 2.2 g/cm^3 (Duxbury and Callahan, 1989b), which are relatively low when compared to meteoritic analogs, indicate that Phobos possibly consists of 10 % to as high as 40 % low density material depending on the grain density assumed. The low density material could for instance be pore space or ice.

This study can put constraints on the knowledge of Phobos' motion in its orbit, its general shape, and on its interior structure. Accurate astrometric observations of Phobos could help to identify secular changes in its motion and may allow to draw conclusions on the orbital evolution of Phobos. The forced libration amplitude as well as improved estimates of the bulk density set more limits to the interior structures.

3 Missions to Mars

During the era of the cold war, the Soviet Union and the United States were competing for the dominance in space. The first aim was to orbit the Earth, then shortly after orbiting and landing on the moon, with subsequent ambitions increasing to visit our neighboring planets.

Starting in the early 1960's a number of missions were planned and conducted with the aim to initially fly-by Mars and later to place a spacecraft in a near Mars orbit. Since 1960, 38 missions were initiated towards Mars (Saiger, 2007; Spiegel, 2007). Many of the early missions failed to meet the expectations. However, the latter missions were increasingly sophisticated and successful as orbiters reached a Martian orbit and delivered valuable science data. Placing a lander on the surface of Mars was and still is a more difficult mission (for more details on the history of Mars missions see Beck et al. (2008)).

Planetary space missions usually carry at least one imaging subsystem. Missions with the primary goal to explore Mars occasionally also obtained images of Phobos and Deimos. One can differentiate between missions which imaged the moons while approaching Mars and then entering an orbit close to Mars and missions with elliptical orbits reaching past the orbits of the moons (cf. Table 2).

In this section, space missions which returned data from Phobos will be described. The subsequent section (3.2) will specifically address the camera systems of interest to this analysis.

3.1 Missions to Phobos and Deimos

In 1971, Mariner 9 was the first artificial satellite of Mars. It obtained not only a set of images with full coverage of the Martian surface but in addition also 80 images of Phobos (Duxbury and Callahan, 1989a). The 32 high resolution images were used to assemble the first map of Phobos (Veverka et al., 1974) and the first shape model (Turner, 1978).

Table 2: Missions which returned image data of Phobos and a short description of their orbits. (Veverka et al., 1974; Williams, 2008; Kolyuka et al., 1991; Jaumann et al., 2007)

Mission (launch year)	Orbit description	Average altitude
Mariner 9 (1971)	elliptical orbit with 64.4 degree inclination	1650 to 12650 km
Viking Orbiter 1 (1975)	elliptical orbit with 37 to 39 degrees inclination	300 to 56.000 km
Viking Orbiter 2 (1975)	elliptical orbit with 55 to 80 degrees inclination	300 to 33.000 km
Phobos 2 (1989)	Mars orbit coplanar with Phobos but 300 km further out	approx. 9675 km
Mars Global Surveyor (1996)	circular, near polar, Sun-synchronous	approx. 3800 km
Mars Express (2003)	highly elliptical, near polar	250 to 11.000 km
Mars Reconnaissance Orbiter (2005)	circular, near polar	255 to 320 km

Only 4 years later, in 1975, the twin spacecraft Viking 1 and Viking 2 were launched. The mission's main objectives were (a) imaging the Martian surface in high resolution, (b) characterization of the atmosphere and surface, and (c) the search for evidence of life. However, thanks to their elliptical orbits reaching beyond the orbit of Phobos, both spacecraft performed several fly-by maneuvers to image Phobos with resolutions of 200 m/pixel and better (Duxbury and Callahan, 1988). Over 500 images of both natural satellites of Mars were obtained at fly-by distances ranging from 20 km and 90 km, for Deimos and Phobos, respectively, to 20,000 km.

In 1989 the ill-fated Russian *Phobos 2* spacecraft returned 37 images of Phobos. The mission aimed primarily at exploring Phobos. However, it had additional instruments on board to also study targets such as the Sun, Mars, and the interplanetary medium. The *Phobos 2* spacecraft was to approach the moon to within 30 to 50 m above the surface to undertake in depth studies of the surface. Unfortunately the mission objectives could not be met due to the loss of the spacecraft several days before the closest approach to Phobos (Sagdeev and Zakharov, 1990).

The Mars Global Surveyor (MGS) spacecraft, launched in 1996, was the first successful U.S. mission to be placed into Mars orbit since the Viking Orbiters. This mission had to accomplish a number of science objectives. Albee et al. (2001) are pointing out six mainly geological or geophysical science goals of MGS. The mission was further adopted to e.g. provide for other science objectives such as relay capabilities to future lander missions and support in landing site selection planning. MGS carried four on-board science packages. Among the visual imaging package was the Mars Orbiter Camera (MOC) (see section 3.2) which returned over 250,000 images during mission life time between 12 September 1997 and 2 November 2006. MOC obtained numerous images of the shadow of Phobos on the Martian surface during the mapping phase. During MGS' four close encounters with Phobos in the first science phase, the Mars Orbiter Laser Altimeter conducted a ranging experiment (Banerdt and Neumann, 1999) while MOC imaged the surface of Phobos in very high resolution during the fly-bys.

On 2 June 2003 the Mars Express spacecraft (MEX), the first space mission led by the European Space Agency (ESA) with destination Mars, was launched. Its prime scientific goal, besides others, was to obtain global high resolution stereo coverage (10 m/pixel) and super-resolution imaging in selected areas (Chicarro, 2000). Hence, the High Resolution Stereo Camera (HRSC) is a major scientific payload. It is a successor of the HRSC flight model of the 1996 Russian-led Mars-96 mission which did not reach space due to a failure of the launch vehicle. The HRSC for MEX was additionally equipped with a Super Resolution Channel (SRC) to obtain meter resolution images nested within the HRSC scenes (Neukum and Jaumann, 2004). A pericenter height of 250 km is required to obtain image resolutions below 20 m/pixel (Jaumann et al., 2007). Mars Express is in a highly elliptical orbit around Mars reaching beyond the orbit of Phobos (cf. Table 2) and is observing Phobos on a regular basis.

By the end of December 2008 MEX performed 110 Phobos fly-bys returning at least one image of Phobos. During 107 of these fly-bys SRC images were obtained with resolutions ranging from as low as 0.9 m, obtained during the closest approach with a fly-by distance of only 93 km, to 105 m.

Mars Express is currently in its second extension of operation after successfully operating during the primary mission life time. Operations within the scope of the second extension will continue until May 2009. A third extension is approved until December 2009, while

a fourth extension is currently discussed. It would provide even more opportunities to observe Phobos from a close range.

The Mars Reconnaissance Orbiter, which was launched in August 2005 and arrived at Mars in March 2006, is equipped with a whole set of camera systems. Besides the navigation cameras it is equipped with the Context Camera (CTX) and the High Resolution Imaging Science Experiment (HiRISE). While images of the navigation cameras are used to observe Phobos' position in its orbit (Jacobson, 2008), HiRISE and CTX observed Phobos from the MRO orbit around Mars. Through the large focal length of 11.99 m of HiRISE, Phobos was still imaged with a resolution of 6.8 to 5.8 m/pixel when observed from a distances of approximately 6800 to 5800 km. However, the orbit of MRO is too close to Mars for the spacecraft to view the anti Mars side of Phobos. A global coverage with HiRISE can thus not be expected. To the current date two such observations were made by HiRISE. Further three images of Phobos obtained by the CTX can be found in NASAs archives.

3.2 Camera Systems of Different Space Missions

Many space missions carry a camera system which is designed according to the scientific aims and the general mission objectives – and dependent on the state of the art technology. Photogrammetric techniques require the knowledge of the geometry during image acquisition. This includes the inner geometry of the camera. To combine data sets from different missions one needs to consider the differences between the inner orientations of the cameras. Descriptions of camera systems which delivered image data used during this study, can be found in this section.

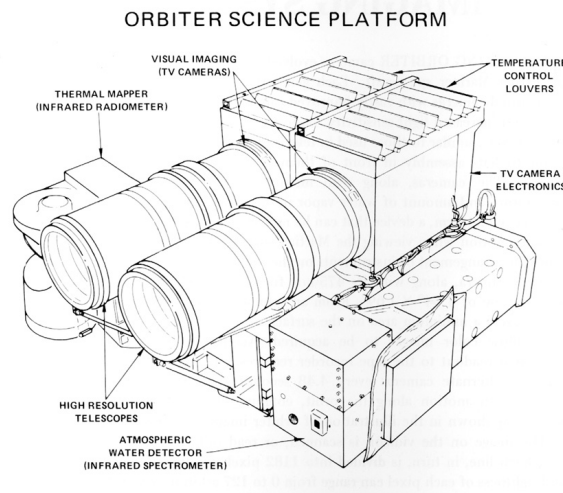


Figure 5: Diagramm of the Viking Orbiter Visual-Imaging System.

3.2.1 The Viking Orbiter Cameras

Both of the Viking Orbiters were equipped with twin cameras called the visual-imaging system (VIS). Each of the VIS consisted of two identical vidicon cameras with a nominal focal length of 475 mm and an offset between the optical axis of 1.38 degree (Figure 5). The focal length of the optical systems was later calibrated separately. The cameras were slow-scanning framing cameras mounted on the scan platform of each orbiter. The

vidicon board had no heat control so that the geometry changed between different images depending on the temperature. To be able to correct this distortion, a reseau grid was built into all four cameras. The 103 reseau marks were approximately $40\ \mu\text{m}$ on each side and their calibrated coordinates were known with an uncertainty of $2\ \mu\text{m}$. Image distortions observed prior to a geometric calibration through the reseau grid were in the order of 3 pixels in the center of the image, increasing towards the edges of the image to 6 to 11 pixels (Wu et al., 1982, and references therein). However, through calibration the distortion can be reduced to approx. $2\ \mu\text{m}$ for the entire image (Ruiz, 1976).

An image obtained by a VIS camera has 1056 lines and 1182 samples. One image element had the size of $11.76\ \mu\text{m}$ by $11.76\ \mu\text{m}$ (Zeitler, 1999) with a field of view (FOV) of $25\ \mu\text{rad}$. This corresponds to a total field of view of 1.538° by 1.692° for each image. Images were taken alternately by one VIS with a nominal overlap of 18.4% with adjacent images providing a wide-swath coverage of the surface.

3.2.2 The Mars Orbiter Camera

The Mars Orbiter Camera (MOC) consisted of three optical instruments. The narrow-angle and the two wide-angle cameras were integrated within MOC using a common electronic. They were designed to obtain high resolution images of the Martian surface and lower resolution mosaics of the planets surface and atmosphere. Built into an approximately 80 cm long and 40 cm wide cylinder like housing (see Fig. 6) the narrow-angle camera had a focal length of 3.5 m while the wide-angle cameras used an optic with 11 mm focal length (Malin et al., 1991). The cameras worked in a push-broom principle building the image line by line while moving over the target. Hence, the swath width was dependent on the focal length and on the altitude of the spacecraft. The length of the resulting image depended on the time span of image acquisition.

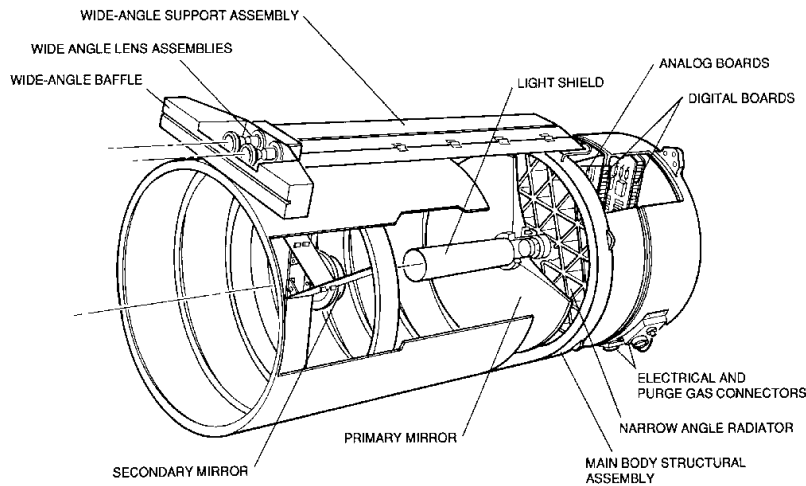


Figure 6: Diagram of the Viking Orbiter Visual-Imaging System.

Images of the narrow-angle camera (NAC) covered an area of $2.9\text{ km} \times 2.9\text{ km}$ with a pixel resolution of 1.4 m/pixel from the nominal spacecraft altitude of 380 km . However, the resolution could be reduced by pixel averaging to 11 m/pixel to obtain images of a size up to $2.9\text{ km} \times 500\text{ km}$. The wide-angle camera (WAC) was capable of obtaining limb to limb images of Mars due to its wide FOV of 140 degrees. Again, pixel averaging was applied for global swaths. Smaller areas, covering hundreds of kilometers at one side,

were imaged in pixel resolutions of 250 m/pixel and better.

The mentioned pixel averaging is for both the narrow-angle and the wide-angle cameras a pixel summing procedure which was performed within the instrument before transmission of the images to Earth (Caplinger, 1999). This procedure adds the grey values of the number n of pixels specified and computes the average to obtain only one pixel. The resolution of the resulting pixel is n times lower than the original pixel resolution. Pixel summing could be applied in along- and across-track direction, whereas for the NAC across- and along-track summing needed to be equal but could be variable for the WAC. To obtain global swaths with an overall equal pixel resolution the WAC used a special across-track summing scheme applying no pixel summing at either end of the CCD line and increasing the pixel averaging to the center of the CCD line.

3.2.3 The High Resolution Stereo Camera

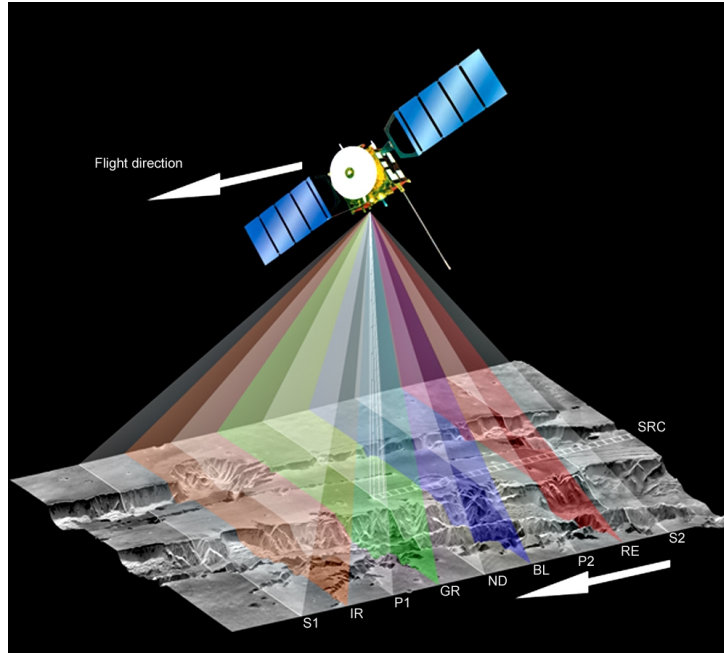


Figure 7: HRSC viewing geometry and operating principle.

The HRSC on board the European Mars Express mission is a multi-spectral, stereo, multi-line scanning push broom camera acquiring simultaneously image swaths of superposed images (Neukum and Jaumann, 2004). It is the successor of the HRSC developed for the ill-fated Mars-96 mission. The camera consists of 9 CCD lines with 5184 active pixels per row and a pixel size of $7\mu m \times 7\mu m$. The CCD lines are mounted in parallel with an angular offset in along-track direction behind one 175 mm focal length lens system (Spiegel, 2007). The stereo-1, infrared, photometry-1, and green channels are directed forward with respect to the nadir channel and the blue, photometry-2, red, and stereo-2 channels are facing backwards during an image scan (see Figure 7). Stereo angles of ± 18.9 degrees are implemented between the stereo-1/ stereo-2 channels and the nadir channel, respectively. The photometry channels are mounted with an angle of ± 12.8 degrees to the nadir channel (Table 3).

Photometry, stereo and the nadir channels are operating in a panchromatic spectrum and can thus be used for simultaneous photogrammetric processing with triple or quintuple

Table 3: Overview of the nine HRSC channels. Positive angles indicate that the channel is directed forward while negative angles are oriented backward (Jaumann et al., 2007).

Channel name	Abbreviation	spectral range	Angle to Nadir
Stereo 1	s1	675±90 nm	+18.9°
Infrared	ir	970±45 nm	+15.9°
Photometry 1	p1	675±90 nm	+12.8°
Green	gr	530±45 nm	+3.3°
Nadir	nd	675±90 nm	–
Blue	bl	440±45 nm	–3.3°
Photometry 2	p2	675±90 nm	–12.8°
Red	re	750±20 nm	–15.9°
Stereo 2	s2	675±90 nm	–18.9°

stereo images (Jaumann et al., 2007). The along-track angles of the boresight vectors were determined for each CCD line separately depending on the position of the CCD line on the CCD plane. The across-track orientation of all boresight vectors is defined to be the geometrical center of the CCD line. At a nominal altitude of 250 km pixel resolutions of 10 m per pixel are realized which corresponds to image swath widths of approximately 52 km. This relates to an across-track field of view of $\pm 6^\circ$. Hence, the width of HRSC images is constrained by the altitude of the observation but the lengths of the images can vary between 400 and 4000 km depending on the duration the camera was operating. About 10 min before and after the pericenter image resolutions are better than 20 m per pixel. The imaging duration for Mars is on average 6 minutes with an exposure time of 2.5 milliseconds per line. Such an image would cover 2610 km of the surface. To decrease data volume and comply with data transfer volumes pixels can be summed by increasing the exposure time (digitally binning) 2, 4 or 8 times for across track compression.

Table 4: Common image compression modes for Phobos fly-by imaging with the HRSC. 1×1 indicates no compression - 2×2 and 4×4, two or four times, respectively. For no image acquisition during fly-bys with a certain imaging mode \emptyset is displayed.

Imaging Mode	Nadir	Stereo	Photometry	Color
... channel compression				
Large Distance	1×1	\emptyset	\emptyset	\emptyset
Stereo High Resolution	1×1	1×1	2×2	\emptyset
Stereo Color	1×1	2×2	2×2	4×4
Color Stereo	1×1	2×2	\emptyset	2×2
Color	\emptyset	\emptyset	\emptyset	1×1

3.2.4 The Super Resolution Channel

The HRSC on MEX was additionally equipped with a Super Resolution Channel (SRC). This channel is in fact a separate camera with a different optical system. However, since it uses the same digital unit as the HRSC, it is, for processing and commanding purposes, integrated as a 10th channel into the HRSC. As a consequence, SRC images can only be obtained when at least one channel of the HRSC is operating.

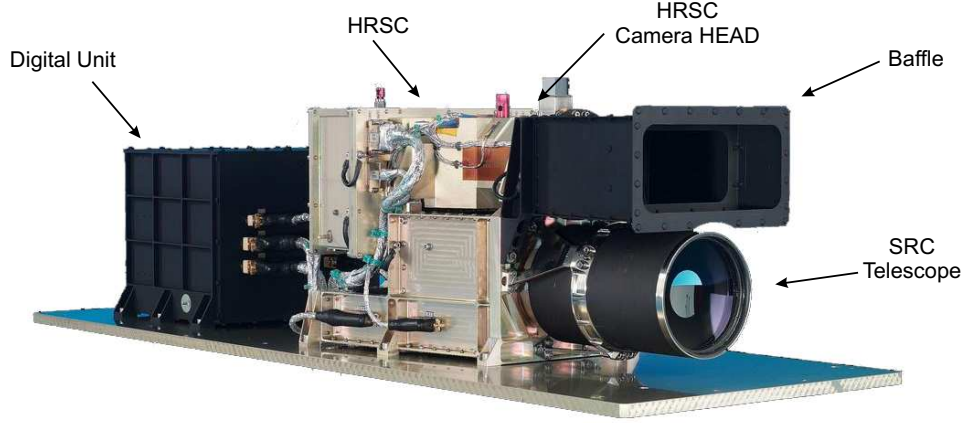


Figure 8: Image of the flight model of the HRSC with SRC.

Table 5: Geometric properties of the SRC camera (Oberst et al., 2008).

Property	Value
Focal length f	988.5 mm (in-flight calibration)
Number of pixels	1024×1024 pixels
Number of active pixels	1008×1018 pixels (lines \times samples)
Pixel size	$9 \times 9 \mu m$
FOV per pixel	$9 \mu rad$
FOV total	$9 mrad$

The SRC has a nominal focal length of 975.0 mm. An in-flight re-calibration of the focal length indicated the significantly larger focal length of 988.5 mm. This figure was confirmed through the determination of the magnification factor between HRSC images and SRC images from Mars orbit. Here the nominal focal length of the HRSC was assumed to be correct. A magnification of 4.33 was observed by comparing surface features observed in HRSC and SRC images within the same orbit (Oberst et al., 2008). The image focal point is defined by the geometric center of the 1024 by 1024 pixel sized CCD array – $x_0 = y_0 = 512.5$. Edge pixels of the CCD array are used to measure dark current leaving an area of 1008 lines with 1018 samples each, defining the active image area of the CCD (Table 5). The optical axes of the SRC and the HRSC nadir channel are bore-sighted. Thus, SRC images are embedded in large HRSC scenes. From the nominal pericenter height of 250 km images with a pixel resolution of 2.3 m per pixel can be recorded. One pixel of the SRC has a field of view of $9 \mu rad$ corresponding to a field of view of 0.5° for the entire image.

Unfortunately strong blurring coupled with ghost effects are observed in SRC images. Star observations are suitable to study the observed astigmatism. However, since point spread functions are varying in different images and no further physical parameters such as the temperature changes of the optic during image acquisition are available, a general point spread function could not be determined. It was estimated that the nominal resolution is reduced by a factor of 2 to 3 by these effects (Oberst et al., 2008).

The SRC CCD sensor was additionally exposed to particle bombardment originating from solar flares and thus severely affected. Hence, the number of “warm”, “hot”, or “dead” pixels with irregular or no response to incoming light has increased. Calibration images taken in Mars orbit show a total of 1000 so called “blemish” pixels while shortly after launch a number of 79 blemish pixels was counted.



(a) Background star with +7.6 visual magnitude



(b) Background star with +8.2 visual magnitude

Figure 9: SRC images of background star observations during the fly-by in MEX orbit 1163. The strong point spread function of the SRC camera depicts point like light sources as a triangle like feature. In both examples one star is visible. Single white or grey dots are hot pixels of the CCD array.

4 Reference Systems and Tools

Reference systems are a set of basic concepts and schemes to define their realizations, reference frames. They are introduced to allow for a clear identification of locations of objects and to describe geometric relations between different objects. Reference frames have in general three dimensions. The mutual motion of planetary bodies is a function of time which is very important information when describing geometric states of bodies. In this section an overview of reference systems and time measures used during this study is given. Tools which were used to handle the available data are also introduced in this section.

4.1 Time

Time is an important coordinate component in planetary sciences. For one, distances are too large to ignore the time electromagnetic waves such as visible light, ultra violet rays, or infrared rays, travel from a source via the target of observation to the sensor. Secondly, the mutual motion of bodies with sometimes very high velocities makes the definition of time epochs necessary. Historically different concepts to define time as a quantity have been developed due to adoption of a concept for certain applications or technical advances such as the atomic clock. The three types of time, Solar Time, Atomic Time, and Dynamical Time, can be distinguished based on the realization of the concepts themselves. Solar time concepts refer to subsequent transits of the sun through the same meridian. Atomic clocks do define units and origins for an Atomic Time concept and the ephemerides of planetary bodies state the realization for Dynamical Times (Montenbruck and Gill, 2001).

For this study two different time measures were used. The times at which images were acquired, are registered in image labels as Coordinated Universal Time (UTC) epochs. The UTC, actually the common civil time, is based on the International Atomic Time (TAI) but corrected by an integer number of leap seconds. The leap seconds are applied to closely follow the Universal Time which is the realization of the mean solar time. Hence, UTC is a time determined from two different concepts (Montenbruck and Gill, 2001).

When computing within the used SPICE toolkit (see Section 4.5) times are converted to Ephemeris Times (ET). The time concept implicitly used is the Dynamical Barycentric Time (TDB). TDB is a time based on the dynamical concept and is used to describe the motion of bodies with respect to the solar system barycenter. Within SPICE, and thus within this study, ET means TDB and is expressed in terms of seconds past the reference epoch of J2000. Since UTC equals the TAI plus leap seconds and the difference between TAI and TDB is set to the fixed value of 32.184 seconds, the difference between UTC and TAI is equal to the sum of leap seconds past the reference epoch and 32.184 seconds (Torge, 2001).

$$TDB = ET = UTC + \text{Leap Seconds past reference epoch} + 32.184\text{sec} \quad (1)$$

4.2 Reference Frames

Reference frames are the implementations of reference systems which are defined through a number of conventions. Reference frames are needed to point out locations or describe mutual motions of bodies.

In order to describe the motion of planetary bodies with respect to each other, an inertial system needs to be defined. In Inertial systems Newton's laws of motion are valid. Inertial systems are either at rest or in a uniform rectilinear motion without any rotation (Torge, 2001). Celestial inertial systems are implemented through the definition of a reference epoch at which the origin and the orientation is observed with respect to the stellar sky. The conventional inertial frame J2000.0 serves as the inertial reference frame for this study and is thus the top level of the frame tree (Fig. 10). It is defined by the Earth ecliptic as the fundamental plane at the epoch J2000.0 which was at January 1st 2000, 12:00:00.000 Barycentric Dynamical Time (TDB) which equals to January 1st 2000, 11:58:55.816 Universal Time Coordinated (UTC). The rotation axis Z points northwards and is perpendicular to the fundamental plane. The X -axis points to the vernal equinox at J2000.0. The Y -axis is completing the right handed coordinate frame and is perpendicular to the XZ -plane. The origin of the J2000 frame is defined to be at the geocenter (McCarthy and Petit, 2004). The realization is based on the Fundamental Catalogue FK5 which provides mean positions and proper motions of over 1500 stars for the epoch J2000.0 with high precision.

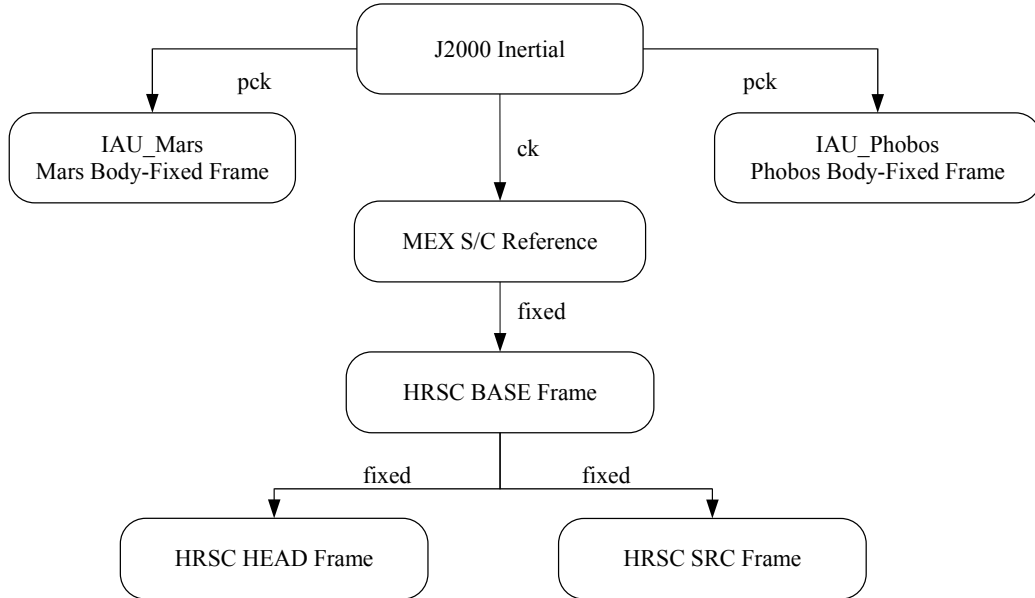


Figure 10: Coordinate frame hierarchy for the HRSC on Mars Express. All translations from a HRSC frame to a body-fixed frame are computed via the inertial frame J2000. Locations and orientations of frames on MEX are known and do not change over time. Time dependent information is needed to convert information from and to the J2000 frame.

To express locations on planetary bodies, body-fixed coordinate systems are required. These reference systems have the advantage that the coordinates of a surface feature do not change with time. The Z -axis of a body-fixed coordinate frame coincides with the mean rotational axis of the body. The north pole, and thus positive Z direction, is that pole which lies north of the invariable plane of the solar system. The invariable plane is defined to pass through the barycenter of the solar system and to be perpendicular to the angular momentum vector of the solar system. The origin of the frame is in the center of mass of the body. Furthermore a prime meridian is defined which is equal to the direction of the X -axis. The Y -axis is perpendicular to the XZ -plane and completes a right handed coordinate frame. Prime meridians on rigid bodies are defined by prominent surface features. For natural satellites in a synchronous orbit, such as Phobos, the positive

X -axis is defined by the mean direction of the sub-planet point of the body.

For a number of planetary bodies the motion of body-fixed frames with respect to the inertial frame is described as a function of time (Seidelmann et al., 2005). The orientation of the rotation axis of a body is defined by the stellar coordinates right ascension α_0 and the declination δ_0 of the pole axis in the J2000 frame. The direction of the prime meridian, which is defined to be the X -axis of the body-fixed frame and is in a first approximation assumed to rotate uniformly with the body, is given by the time variable angle W measured along the equator of the planetary body in positive direction with respect to the north pole from the ascending node. Seidelmann et al. (2002) provides a list of rotational parameters of planetary frames with respect to J2000.

Just like the planets, all spacecraft and subsystems thereon have pre-defined coordinate frames. The root to all frames is the J2000 inertial frame (Fig. 10). To convert coordinates from one frame to another transformations into the J2000 frame are computed. From the J2000 frame another transformation into the destination frame is performed. The SPICE software library is providing this information implicitly once the required kernel information is available (see Section 4.5).

4.2.1 The Phobos Reference Frame

Phobos' prime meridian, which implements the positive X -axis of Phobos, is defined to point on average from the center of mass of Phobos towards the center of Mars. The positive Z -axis is defined to be the perpendicular vector pointing upward with respect to the equatorial plane. To complete the right handed coordinate frame, the Y -axis is perpendicular to the XZ -plane. The negative Y -axis is thus pointing in the direction of Phobos' motion. Due to its prograde motion longitudes on Phobos are positive increasing to the West (Seidelmann et al., 2007).

The orientation of Phobos' body-fixed frame with respect to the inertial frame J2000 is defined by the rotation of the prime meridian W ,

$$W = 35^\circ.06 + 1128.8445850^\circ/\text{day } d + 8.864^\circ/\text{cen}^2 T^2 - 1^\circ.42 \sin M1 - 0^\circ.78 \sin M2, \quad (2)$$

and the orientation of the rotation axis with respect to the stellar coordinates α_0 and δ_0 ,

$$\begin{aligned} \alpha_0 &= 317^\circ.68 - 0.108^\circ/\text{cen} T + 1^\circ.79 \sin M1 \\ \delta_0 &= 52^\circ.90 - 0.061^\circ/\text{cen} T - 1^\circ.08 \cos M1. \end{aligned} \quad (3)$$

Here T is the interval in Julian centuries (of 36525 days) from the standard epoch and $M1$ and $M2$ are defined by

$$\begin{aligned} M1 &= 169^\circ.51 - 0.4537640^\circ/\text{day } d \\ M2 &= 192^\circ.93 + 1128.4096700^\circ/\text{day } d + 8^\circ.864/T^2, \end{aligned} \quad (4)$$

with d being the interval of days from the standard epoch (Seidelmann et al., 2002).

The expressions for the orientation of the rotation axis (Eq. (3)) include two small variations. The first – including the century dependency T – accounts for a minor linear secular variation of the orbital plane. The second term expresses periodic variations due to torques exerted on Phobos by planetary bodies – the precession (Montenbruck and Gill,

2001). Mars, the Sun and possibly Deimos have dominant influence on Phobos' precession motion. Looking at equation (4) it becomes apparent that the precession has a period of about 793 days. As the amplitudes are different in the direction of the right ascension α_0 and the declination δ_0 the precession describes an elliptic motion of the rotation axis (Eq. (3)).

Since Phobos is locked in synchronous rotation, the orientation of the prime meridian W (Eq. (2)) is completing one period with one revolution of Phobos about Mars. This is expressed through the term $1128.8445850d$ which indicates that Phobos takes 0.31891 days (= 7 h 39 min 14 sec) to complete one orbit (cf. Table 1). The third term on the right hand side of equation (2) indicates a small secular acceleration. The next term is again a correction for the precession of the rotation axis which slightly effects the orientation of the prime meridian.

Furthermore, the prime meridian is affected by the forced libration expressed through the term $-0^\circ.78 \sin M2$ in equation (2). While $-0^\circ.78$ equals the currently recommended amplitude of the forced libration, $M2$ models a one-to-one coupling of the forced libration to the orbit. The forced libration causes an additional oscillation of the prime meridian during one orbit. The period of the forced libration is just smaller than the orbital period. The difference of

$$-0.434915^\circ/\text{day} = 1128.4096700^\circ/\text{day} - 1128.8445850^\circ/\text{day} \quad (5)$$

equals the secular change of the ascending node of Phobos. The ascending node Ω is the angle between the vernal equinox and the point at which the satellite crosses the parent body equator from south to north (Montenbruck and Gill, 2001). Its change due to perturbation caused by the Martian gravity coefficient J_2 can be computed with

$$\dot{\Omega} = -\frac{3}{2}n_0J_2\frac{R_{Mars}^2}{a^2}\cos i \quad \text{with} \quad n_0 = \sqrt{\frac{GM_{Mars}}{a^3}}. \quad (6)$$

The Martian gravitational coefficient J_2 represents the main perturbation force on Phobos. R_{Mars} is the equatorial radius of Mars, $G = 6.67259 \times 10^{-20} \text{ kg}^{-1} \text{ km}^3 \text{ sec}^{-2}$ the gravitational constant, M_{Mars} the mass of Mars, a is the semi major axis of the satellite orbit, and i represents the orbit inclination. Using the values in Table 6 the secular motion of the line of nodes is computed to be $-0.43411^\circ/d$. Additional perturbations, not accounted for in Eq. (6), cause the small discrepancy to the value given in Eq. (5).

Table 6: Values used to compute the secular motion of the ascending node Ω .

Source	Variable	Value
Seidelmann et al. (2007)	R_{Mars}	3396.19 km
Konopliv et al. (2006)	J_2	1.956×10^{-3}
	M_{Mars}	$0.6418 \times 10^{24} \text{ kg}$
Jacobson (2008)	a	9377.2 km
	i	1.075°

The model of the orientation of Phobos' body-fixed frame is implicitly used during transformations to and from the Phobos body-fixed frame within this study.

4.3 Surfaces and Maps

Sphere or ellipsoid models are defined as a good approximation for regular shaped planetary bodies (Seidelmann et al., 2007). The (simple) model for Mars is defined by a rotational ellipsoid with the radii of $3396.19 \times 3396.19 \times 3376.20$ km. However, the reference body for heights used during this study is the so called Mars Orbiter Laser Altimeter (MOLA) sphere with a radius of 3396.0 km (Smith et al., 2003). Measurements of the MOLA experiment on MGS were used to compute a global digital terrain model (DTM) for Mars. Heights are stored in form of the Mission Experiment Gridded Data Record (MEGDR) and are registered with respect to the MOLA-sphere (Smith et al., 2001a).

The Mars Digital Image Model 2.1 (MDIM 2.1) is a revised version of an earlier Viking Orbiter image mosaic. It is an ortho-image draped onto the MOLA topography and based on control points referenced to the IAU 2000 reference frame for Mars (Archinal et al., 2003). MDIM 2.1 is used as a reference to control map projections for Mars.

Even though Phobos is a planetary body of irregular shape, a triaxial ellipsoid model has been defined. The axes of Phobos are currently known to be $13.4 \times 11.2 \times 9.2$ km (see Table 1). The approximation through an ellipsoid is of limited use when it comes to applications such as dynamical modeling or determination of physical parameters. For cartographic purposes other models such as those described through spherical harmonic functions and DTMs state a better approximation. Duxbury (1991) determined the coefficients of the spherical harmonic function up to degree and order 8. However, as the spatial frequency of craters on Phobos is too high to be modeled through spherical harmonics of low degree and order, expressions to model local disturbances have been introduced approximating the depth to diameter ratio of craters. Another local function was introduced for Stickney.

4.4 Planetary Image Data

Planetary image data are compressed when received from space. They need to be unpacked and in most cases radiometrically or geometrically corrected before it can be used for any analysis. The processing of image data is divided into different levels. According to the processing level, images have different names and are commonly called *Level X data*, where $X=1\dots4$ indicates the explicit level of processing.

Level 1 data are images which were uncompressed but not yet corrected. Only when a radiometric or geometric correction is finished, images passed the Level 2 processes. In the next step images are – if applicable – ortho-rectified and map projected and thus passed the Level 3 processing. In the case of HRSC images another differentiation takes place as different digital terrain models are used to ortho-rectify and map project the images. A Level 3 image is ortho-rectified based on the DTM information derived from MOLA observations. A DTM determined from the HRSC stereo information is used to ortho-rectify images for cartographic processes which are Level 4 data.

For the HRSC the following naming convention was adapted. Images are labelled

$$hxxxx_yyyy.zzL.vv$$

where h stands simply for the HRSC instrument. The first four digits $xxxx$ mark the orbit number. $yyyy$ indicate the number of the image in the orbit, zz is the indicator of the channel which acquired the image. L is the number of processing level and vv is the version number of the image.

Planetary images usually contain a text header. The headers include general information such as the size of the image or data format. More detailed information of the orbit, state of the camera, map projections – if applicable – and processing steps are registered in the header, too. Especially the image time and the best ground resolution are important information often queried during this study.

4.5 Software

SPICE

Table 7: SPICE is an acronym. Information in the SPICE system is stored in Kernels which contents is summarized in this table (Acton and Baalke, 2007).

S	-	Spacecraft ephemeris, given as a function of time
P	-	Planet, satellite, comet, or asteroid ephemerides, or more generally, location of any target body, given as a function of time
I	-	Instrument description kernel, containing descriptive data peculiar to a particular scientific instrument, such as field-of-view size, shape and orientation parameters
C	-	Pointing kernel, containing a transformation, traditionally called the C-matrix, which provides time-tagged pointing (orientation) angles for a spacecraft structure upon which science instruments are mounted. May also include angular rate data
E	-	Events kernel, summarizing mission activities - both planned and unanticipated. Events data are contained in the SPICE EK file set, which consists of three components: Science Plans, Sequences, and Notes

SPICE is an information system to assist scientist and engineers working with scientific data from planetary exploration mission and designing space mission. A major component of the SPICE system, which was developed by the Navigation and Ancillary Information Facility (NAIF), is a large software suite of subroutines called SPICELIB (Acton, 1999). Subroutines are used to

1. read SPICE-Kernels which contain information of e.g. properties of planetary bodies or spacecraft (see Tabel 7),
2. compute different quantities of interest to scientists and engineers.

The software library supports for example the computation of observation geometries in different frames accounting for light time corrections and at different times. The SPICE system was used for most of the computations of this study. Information such as e.g. the orientation of frames, positions of objects are stored in SPICE-kernels.

Furthermore, kernels containing frame information (FK-Kernel) or spacecraft clock ticks (SCKL-Kernel) and leap-second definitions (LPS-Kernel) are available. Other information such as shapes can be implemented as needed and are currently under development.

SPICE supports nearly all National Aeronautics and Space Administration (NASA) space missions. It was prepared to be used for the Russian-96 mission and now supports Mars Express and other European space missions such as Rosetta and Venus Express.

This software library was used for most computations during this study. Since essential

informations such as the orbit models of Phobos, the trajectory of MEX, or the motion of Mars with respect to the solar system are available in SPICE kernels, the SPICE software routines and functions are a comfortable tool to compute for instance the position of MEX with respect to the Phobos body-fixed frame or the position of Phobos as seen from the Martian surface.

Bundle Block Adjustment Software

During the course of this study image data obtained by two different camera systems, namely framing cameras and push-broom cameras, were used to compute object point coordinates through bundle block adjustment techniques. To accommodate the specific properties of the camera systems the collinearity equations, which represent the functional model behind a bundle block adjustment, are adopted accordingly.

Hence, different applications exist at the German Aerospace Center (DLR) to maintain support for a variety of camera systems. During this study the software *dlradjust* and *hwbundle*, latter provided by Spiegel (2007), were used to solve the control point network and to improve orientation data of HRSC images for computation of the digital terrain model, respectively. Both software applications can be controlled through numerous parameters such that the model of the 3D-coordinate reconstruction can be adapted to e.g. a spacecraft drift or a different weighing scheme.

Ellipse-Fit Function

Several times it was necessary to determine ellipse parameters on the basis of point measurements during this study. Control points of the Duxbury and Callahan (1989b) network for instance were determined through an ellipse-fit. Likewise the position of Phobos' shadow center on the Martian surface was determined via an ellipse-fit. A routine freely available online was used (Markwardt, 2008).

5 Astrometric Observations

Orbit modeling is based on the two-body Kepler problem. In addition known perturbations are introduced to model the orbit of an object as correctly as possible. However, the knowledge of the perturbing forces is limited. This is especially true in the case of Phobos as it is orbiting deep in the gravity field of Mars. Even for Deimos, the smaller of the two moons, which is orbiting with approx. 22,000 km distance to Mars, accelerations due to regional differences in the Martian gravity field can be observed (Gläser, 2008). Astrometric observations are used to compare the modeled orbit with the actual position of the moons. Fitting orbit models to astrometric observations can constrain perturbation parameters depending on the overall accuracy of the solution.

Up to the current date, the orbit of Phobos is studied by means of ground-based observations (Morley, 1989; Veiga, 2008) during Mars oppositions. Even though accuracies are more and more improving through ever more sophisticated technical tools, observation accuracies are still in the order of 14 km in the object space. Through the number of observations as well as the time span of 130 years of observations, the orbit model of Phobos is, however, one of the most accurate available models for planetary bodies.

5.1 Previous Astrometric Observations

The large number of space missions launched to explore Mars (cf. Section 3) provide new opportunities and alternatives to observe the position of Phobos in its orbit. Mariner 9 was the first spacecraft to observe the Martian moons through a TV camera (Duxbury and Callahan, 1989a). Stellar coordinates with respect to the spacecraft position were determined by approximating the center of figure (COF) of Phobos in the images. An offset between the COF and center of Mass (COM) was not known to that date. It was assumed to be smaller than the center finding error. The limb of Phobos was modeled as an ellipse resulting from the intersection of a plane, which is parallel to the image plane, with a triaxial ellipsoid model of Phobos. A one sigma error of 1 km between the surface and the ellipse-model was observed. In the late 1970's for the first time the Viking orbiters obtained global image coverage of Phobos (Duxbury and Callahan, 1989b). These observations were reduced in a similar way as the Mariner 9 observations. Accuracies of astrometric measurements of Phobos were for both missions in the order of 3 to 10 km.

In 1989 the Russian Phobos 2 mission reached the orbit about Mars and approached Phobos but was then lost shortly before its closest approach. It did send back 37 images of Phobos which Kolyuka et al. (1991) used to determine the position of Phobos. Two methods were applied to determine Phobos' position. The first approach was to overlay the Phobos' figured model computed by Duxbury (1991). In a second approach a control point network was measured. These control points were then used to determine the position of Phobos with respect to the spacecraft position. Derived stellar coordinates showed uncertainties of approximately 2 km (Kolyuka et al., 1991).

A decade later, MGS (Mars Global Surveyor) was the first spacecraft to revisit Phobos. The MOLA (Mars Orbiter Laser Altimeter) Ranging Experiment to Phobos (Banerdt and Neumann, 1999) was carried out. With an uncertainty of 1 km (1σ of the MGS position) a discrepancy of 3.8 km between Phobos' orbit model and observed position was determined. In addition the position of Phobos' shadows observed through MOLA were analyzed (Neumann et al., 2004). To be able to bring observation and predicted position

into agreement, the position of Phobos was corrected by moving Phobos approximately 4km ahead of its predicted position in along track direction. With the observation of Phobos eclipse events from the Mars Exploration Rovers, discrepancies of 12km to the orbit prediction model *MAR033* were reported (Bell et al., 2005). These discrepancies were later confirmed by a number of astrometric observations obtained from SRC images (Oberst et al., 2006). For the latter analysis the limb was again approximated through an ellipse. A main error source, the pointing accuracy of the camera, could be ruled out in some cases due to background star observations.

New orbit models are released sporadically but mostly with the publication of a larger number of new astrometric measurements or when space missions, which are reaching beyond the orbit of Phobos, are in place. In 1999 the orbit prediction model *MAR033* was compiled based on observations available to that date (Morley, 1989). However, confirmed uncertainties of this orbit model as well as the large number of new observations of Phobos' position against the stellar sky led to the release of new orbit models by two groups in 2006 and 2007 by the JPL (Jet Propulsion Laboratory) and the ROB (Royal Observatory of Belgium), respectively (Jacobson and Rush, 2006; Lainey et al., 2007).

In the following section the approach to analyze Phobos' shadow observations of the MOC and the HRSC cameras is described. Furthermore, a method to obtain astrometric observations from fly-by images is presented. Results of both approaches are compared to current orbit models for Phobos.

5.2 Shadow Observations

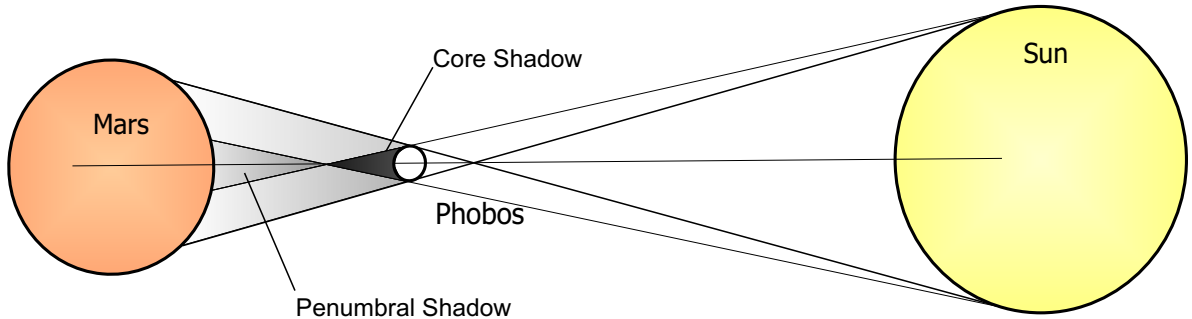


Figure 11: Phobos is shading Mars only through partial eclipses. Such eclipse events occur on average 3.22 times per day. (diagram not to scale)

The MOC and the HRSC obtained images of Phobos' shadow moving across the surface of Mars. The HRSC was especially commanded to point into the direction of the shadow, slightly off nadir, to obtain the images. MOC, on the other hand, mostly captured the shadow while scanning a global image of Mars. Only 12 shadow observations from 6 orbits are available in HRSC image scenes (Table 8) and 334 MOC images were found containing the Phobos shadow. HRSC images containing Phobos' shadow were obtained with pixel resolutions from 100 m/pixel to 400 m/pixel. Shadow images obtained by MOC have resolutions ranging from 1 to 7 km/pixel.

Phobos is too small to cover the solar disc completely when viewed from Mars (Bell et al., 2005). The visible shadow on the surface is the diffuse penumbral shadow of Phobos (cf. Figures 11 and 12). Phobos is moving with a mean absolute speed of 2.14 km/sec around Mars. The relative velocity of Phobos when observed from Mars is reduced due to the

Table 8: Phobos shadow observations by the HRSC

Orbit No.	Channels	approx. Latitude
2239	nd,gr,bl,	55° North
2345	nd, gr, bl	28° North
2451	nd, bl	14° North
2549	nd, bl	3° North
2598	nd	2° South
2729	nd	18° South

rotation of Mars and the fact that Phobos is in a prograde rotation. However, it is still 3.2 times faster than the angular velocity of Mars' rotation. Hence, Phobos rises in the West and is setting in the East. The shadow of Phobos is moving with a relative velocity of 1.47 km/sec across the surface of Mars.

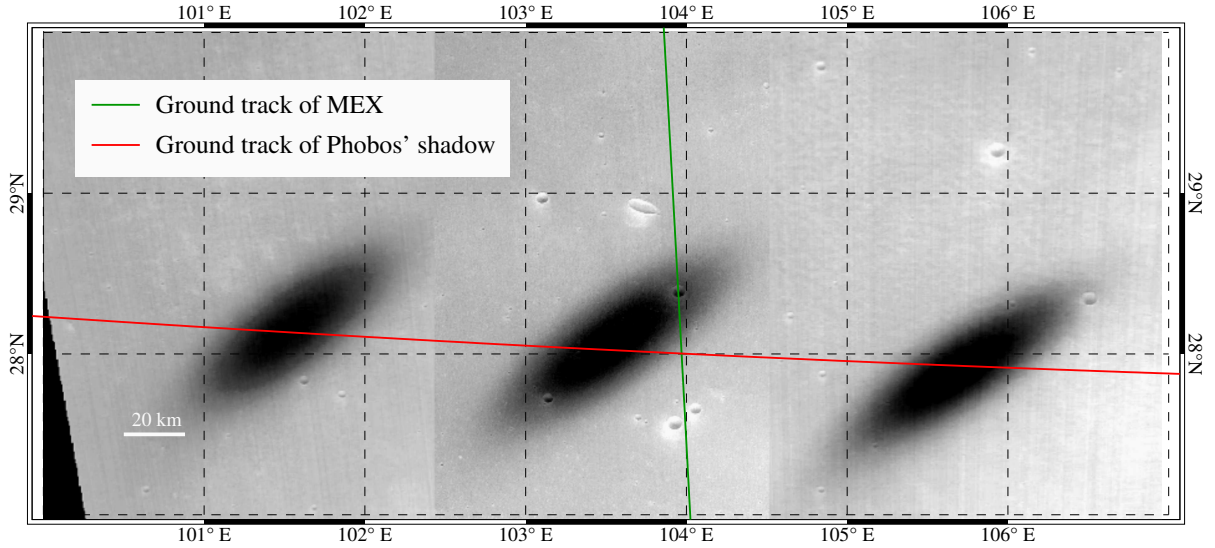


Figure 12: The footprint of the sub-spacecraft point and the projected COM Phobos track defined by the vector originating in the Sun and passing through the COM of Phobos. The shadows were observed during MEX orbit 2345. The shadow moves West to East and is captured by the blue, nadir and green channel, from left to right.

The Phobos orbit plane has an inclination of 1.075 degrees to the equatorial plane of Mars. MEX on the other hand has an almost polar orbit. Hence, both trajectory planes are nearly perpendicular to each other (Figure 12).

The relative speed of Phobos' shadow with respect to the push broom principle cameras which observed the shadow is too high to obtain an instantaneous image of the shadow as a frame camera would obtain. The line scanner moves e.g. from South to North while the shadow moves from West to East. Hence, the scanner captures first the most southerly parts of the shadow. By the time the scanner captures the next line, the shadow has moved further East in its track. In case of the nadir channel image in the HRSC orbit 2345, for instance, the shadow is covered by over 6200 lines which were recorded in a time span of approx. 42 seconds. During this time the shadow moved about 62 km further to the East. The obtained image shows the shadow in a first approximation as an elongated ellipse with the most northerly part of the shadow much further East than the most southerly

part of the shadow. The ellipse is stretched by different scales depending on the geometric

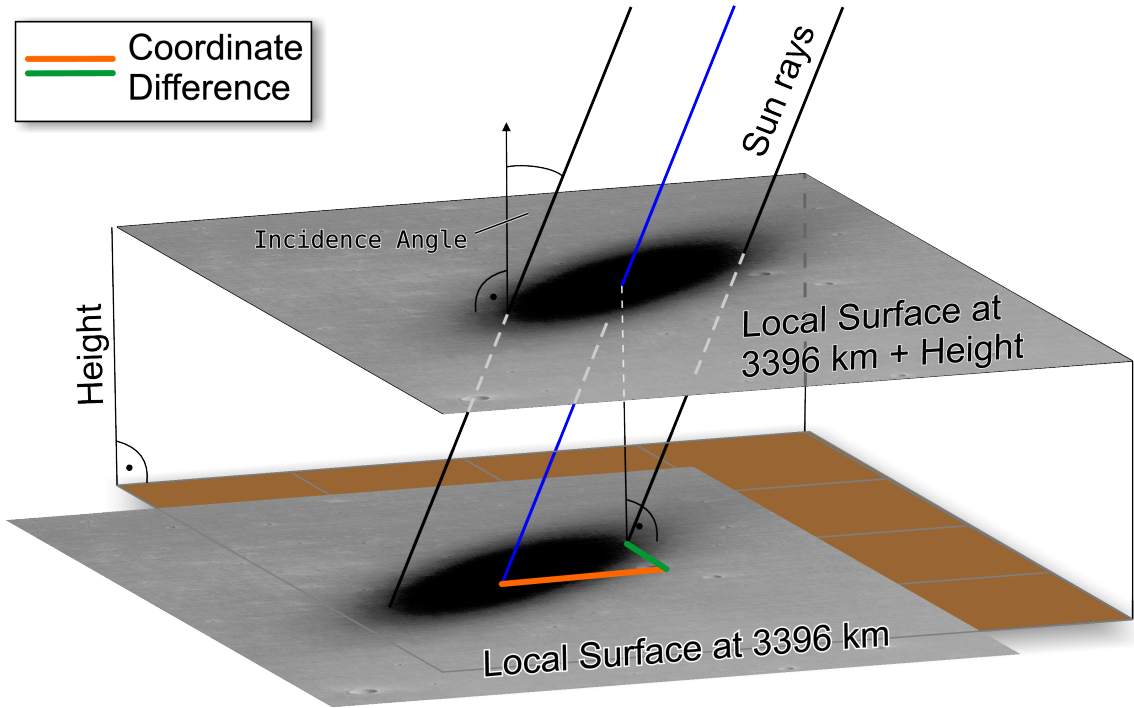


Figure 13: The location of the shadow is dependent on the height of the terrain the shadow is projected on. Coordinate differences vary with the incidence angle of the sun.

situation between Sun, Phobos and spacecraft. If the shadow is observed very close to the terminator it is naturally deformed due to the very large incidence angle of the Sun (Bills and Comstock, 2005). The coordinate of the shadow center is dependent on the height, with respect to the reference surface, of the area where the shadow was observed. The height, time, and the sun incidence angle are considered to be the largest error sources of this analysis. The larger the incidence angle of the sun, the more important is the accuracy of the height information (Fig. 13). The image of the shadow is furthermore dependent on the underlying topography. If surface elevations change drastically in the area of the shadow, this further elongates or shortens the shadow image (see Figure 14).

In a first approximation, it was assumed that the center of the shadow ellipse equals the projection of the center of figure of Phobos onto the surface of Mars. Additionally, it was assumed that the center of mass of Phobos coincides with the center of figure. The center of the shadow ellipse is defined to be the intersection of the semi-major and semi-minor axis.

The following information is required to compare observed locations of the shadow with the predicted locations:

- the coordinates of the shadow center,
- the time of acquisition of the line depicting the shadow center,
- the height of the underlying terrain.

Each information listed above needed to be determined through a different data set. The coordinates of the shadow center, with respect to the Mars body-fixed frame, can only be extracted from map projected, georeferenced images. The height can only be queried from a DTM once the correct coordinate pair of the location is known. The acquisition times of the image lines are only available up to Level 2 of the systematic image processing chain (cf. Section 4.4).

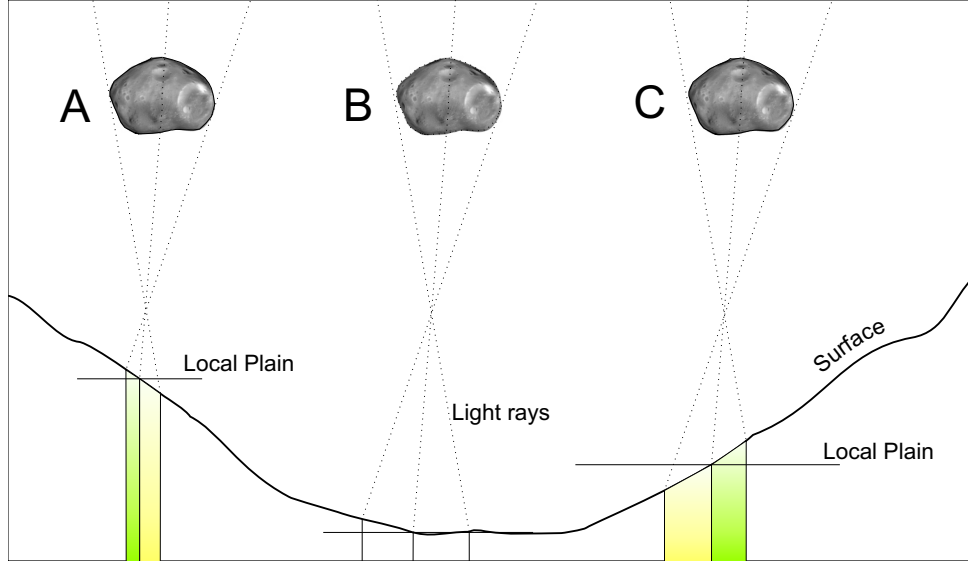


Figure 14: The shadow of Phobos projected onto different declined surfaces with equal projection geometries. In cases A and C the COM of Phobos is not projected into the center of the ellipse. The yellow quadrangles indicate that the COM projection is further away from this side of the ellipse. Green depicts a smaller distance.

5.2.1 Determination of the 3D - Coordinates

The planetocentric MOLA DTM contains height information with respect to the MOLA sphere. To determine the coordinates of the shadow center with respect to a uniform reference system, all images containing shadow observations were mapped onto a DTM model into an equidistant map projection. As the projection relies on the orientation data of the cameras, results of this process may, depending on the quality of this information, be shifted in lateral direction with respect to the known reference grid. To ensure that the geo-referenced images are correctly related to one reference frame the locations of surface features were compared to the MDIM 2.1. No offset between HRSC images and the MDIM 2.1 was observed. However, MOC images showed significant discrepancies in the location of surface features with respect to the MDIM 2.1. To correctly accommodate the images in comparison with the global image mosaic, a transformation was computed based on conjugate point observations. Once the correct reference was established, images were radiometrically stretched to improve the sharpness of the shadow outline. The shadow center was determined by collecting a number of points along the shadow edge. Ellipse fitting algorithms were used to determine the coordinates of the center of the ellipse from these points. The coordinate pair was used to read out the height at this point above the MOLA sphere from the MOLA planetocentric model (Mission Experiment Gridded Data Record, MEGDR) (Bendig, 2006).

5.2.2 Determination of Time

Up to processing level 2, HRSC image lines have a prefix which contains the exact time of exposure. For a detailed reconstruction of the shadow a list of epochs was determined containing the times of exposure for each line containing the shadow (see Section 5.2.4). However, to determine the line which contains the shadow center the same procedure used to determine the coordinate of the shadow center was applied a second time in Level 2 data. With the obtained line coordinate from the ellipse fit in the Level 2 image the

time could be extracted. For HRSC images it was tested if the pixel determined through the ellipse fit in Level 2 corresponds to the pixel of the center of the shadow observed in Level 3 through the ellipse fit method by tracing the pixels during the process of ortho-rectification.

Table 9: Differences of observed line coordinates to traced line coordinates of the shadow center in comparison with results from different software tools.

Image	Exposure Time per line [ms]	Line difference to observation in			
		ArcGIS		DTMTool	
		[pixel]	[km]	[pixel]	[km]
h2345_0001.bl3	27.3	11.9	0.48	3.86	0.15
h2345_0001.gr3	27.3	-13.8	-0.56	-7.84	-0.31
h2345_0001.nd3	6.8	17.5	0.18	-34.48	-0.34
h2451_0002.bl3	27.3	-2.0	-0.08	16.98	0.68
h2451_0002.nd3	6.8	15.0	0.15	-42.99	-0.43
h2549_0001.bl3	20.9	-13.6	-0.42	-40.62	-1.25
h2549_0001.nd3	5.2	57.5	0.44	-12.48	-0.10
h2598_0002.nd3	7.1	3.7	0.04	-10.28	-0.11
h2729_0000.nd3	11.3	-2.8	-0.05	-11.81	-0.20

The line containing the shadow center was determined with two different software tools, ArcGIS and the DLR software DTMTool. Table 9 shows a list of line differences observed between the line coordinate determined through ellipse fit and the one determined through pixel tracing. The difference in the observed line coordinates can be considered as an uncertainty of the observation of Phobos' position influenced by the time component of the observations. If combined with the relative velocity of the shadow across the surface, an uncertainty in the direction of motion can be determined (Table 9 columns 4 and 6). For the ArcGIS software a mean error of ± 270 m was determined while the uncertainty related to the time component of the observation with the DTMtool is in the order of ± 300 m to ± 400 m (Bendig, 2006).

The determination of the observation time of the shadow centers in MOC images proved to be slightly more challenging and is considered one of the largest uncertainty when analyzing this data set. For the MOC images no line prefix is available as is for the HRSC images. However, records of the *start times* and the *line integration time* can be found in the image labels. Furthermore, the *pixel summing mode* is recorded which is not always linear across the line for MOC images. Two modes - 13 and 27 - are known to have a variable pixel summing across the line to maintain similar pixel resolutions throughout one image line in global swath images. Tables which indicate how the summing was performed are available in Caplinger (1999). However, no clear statement is made by Caplinger (1999) of how pixels are summed along the track in these special summing modes. It is therefore assumed that each recorded line remains unchanged in the resulting image and is not compressed through pixel summing in along-track direction. The time of observation is determined by adding n times the line integration time to the starting time implicitly assuming that no compression took place.

5.2.3 Stellar Coordinates of Phobos

The stellar coordinates of Phobos' center of figure are determined by computing the stellar coordinates of the Sun at the time of observation. It is important to consider the time light travels from the Sun to Mars as we are interested in the geometric state of the Sun, with respect to Mars, at the time the light photon left the Sun to travel to Mars. Hence, the light time correction must be applied in a way that the state of the Sun is determined at the time of observation minus the time light travels from the Sun to Mars. It is assumed that the center of the Sun, Phobos' center of figure and the center of the observed shadow ellipse are exactly aligned. The time light travels from Phobos to the surface of Mars can be neglected as it only takes 0.02 seconds to reach the Martian surface. This would result in a positional uncertainty in the along track direction of approximately 30 m which is below the expected accuracy of the observation.

The position of the center of the shadow was measured in the Mars body-fixed frame and had to be transformed to the inertial frame. The position of the Sun as seen from Mars was also computed in the inertial frame and was added to the negative position vector of the shadow center. A vector pointing from the shadow's center to the Sun results,

$$\begin{bmatrix} X \\ Y \\ Z \end{bmatrix}_{J2000} = - \begin{bmatrix} R_{IAU_Mars \rightarrow J2000} \end{bmatrix} \begin{bmatrix} X_{Shadow} \\ Y_{Shadow} \\ Z_{Shadow} \end{bmatrix}_{IAU_Mars} + \begin{bmatrix} X_{Sun} \\ Y_{Sun} \\ Z_{Sun} \end{bmatrix}_{J2000} \quad (7)$$

This coincides with the direction of Phobos as it was assumed that the three points are aligned. Stellar coordinates are derived through the transition from rectangular to spherical coordinates. The computed radius equals the distance to the sun and is neglected.

To compare the computed position of Phobos with the predicted position of Phobos with respect to the shadow center, the vector \vec{X}_{J2000} is computed again, but this time adding the predicted position of Phobos with respect to Mars to the location of the shadow center. This yields the difference in stellar coordinates.

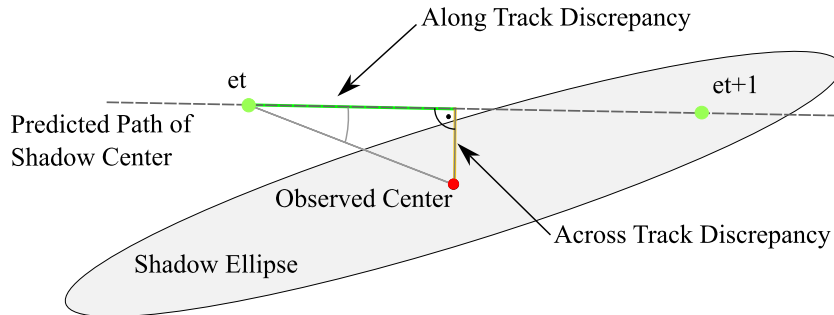


Figure 15: Determination of the across and along track component of the observed discrepancy between orbit prediction model and observation.

However, a more interesting question is how large are the possible differences in the along-track direction and in the across-track direction— out of the orbit plane or in radial direction to Mars – between observation and prediction? To determine these components of the observed differences, the intersection of the extended vector, originating in the Sun and pointing to Phobos at the time of observation of the shadow center et , with the modeled Mars body was computed. For consistency Mars was modeled as a sphere with the radius of 3396 km plus the observed height of the area the shadow was observed in. The coordinates of the intersection indicate the predicted position of the shadow center.

Another intersection at $et+1 \text{ sec}$ was computed. Assuming that the distance between these points is very small and the surface can be modeled as a plane, the along-track and across-track components of the observed difference can be computed via trigonometric function. The angle in the intersection point at et between the observed shadow center and the intersection point at $et + 1 \text{ sec}$ is computed. Assuming that the across-track component is perpendicular to the track the two components can be separated (Figure 15).

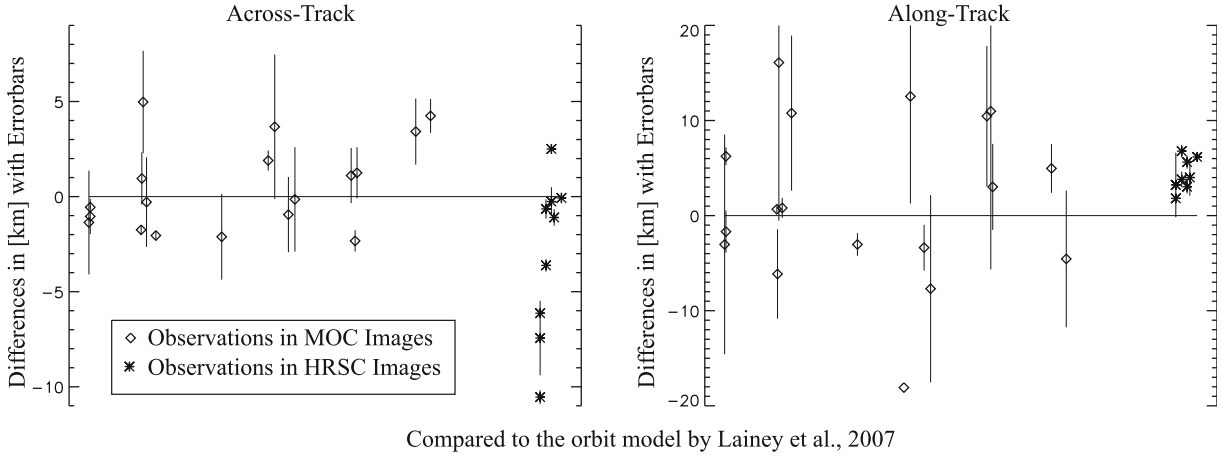


Figure 16: Differences between the observed shadow center and the predicted shadow center subdivided into the along- and across-track component. Positive values in the across-track direction indicate an observation above the orbit plane. Positive values in the along-track direction indicate that Phobos is ahead of its predicted position. Error bars computed are with respect to the empirical determined uncertainty for the observation.

Result of this analysis showed unexpected large scatter between the observations and, compared to previous astrometric observations, oversized discrepancies to the predicted position (Fig. 16). Especially observations in MOC images showed very large uncertainties. The latter may be caused by the low resolution of 7 km per pixel in most of the MOC images. Estimations that the center of the shadow ellipse can be observed in the images with an accuracy of 1 pixel, relates to an uncertainty of the resulting location of $\pm 7 \text{ km}$ in many cases. Furthermore, the uncertainty of the observation of the correct image line directly effects the time of observation and its uncertainty.

The across-track discrepancies between observations and predictions are substantial too. While it was expected that these should be much smaller than in the previous analysis (Oberst et al., 2006), the observed across track differences were equal or in some cases larger. The only across-track component which can be observed through the shadow is the component out of the orbit plane. Physically such a great variation of the across-track discrepancies can not be explained. It is therefore concluded that the model applied is insufficient and another model was designed.

5.2.4 Reconstruction of the Shadow

To refine the modeling of the shadow observation, the shadow outline was reconstructed image line by image line based on orbit prediction models and reconstructed orientation information of Phobos and MEX, respectively. Only HRSC images were considered for this modeling since the uncertainty of the recording time in MOC images remains. An ellipse was fitted to the predicted shadow outline to determine the center of the predicted shadow shape. Thus, it was possible to compare the predicted position with the observed shadow center directly in terms of planet-fixed latitude and longitude.

The reconstruction of the shadow image involved the determination of the visible ellipse of the triaxial Phobos ellipsoid model as seen from the Sun. Vice versa the visible disc of the Sun as seen from Phobos was computed. Note that the visible disc of a spherical or ellipsoidal body from a finite distance is smaller than the diameter of the body.

360 vectors originating at a point at the edge of the visible Sun-disc and pointing to the corresponding point at the visible ellipse of Phobos were defined. To determine the corresponding point on the Phobos visible ellipse the vector to the point of the Sun-disc was shifted along the Sun Phobos vector and scaled to agree with the Phobos ellipse dimensions. The intersecting points of these vectors with the surface of the Mars model were computed. As before, this surface was defined to be a sphere with the radius of 3396 km plus the observed elevation above the MOLA sphere. The points formed roughly an ellipse which was again parameterized by means of an ellipse fit. It was assumed that

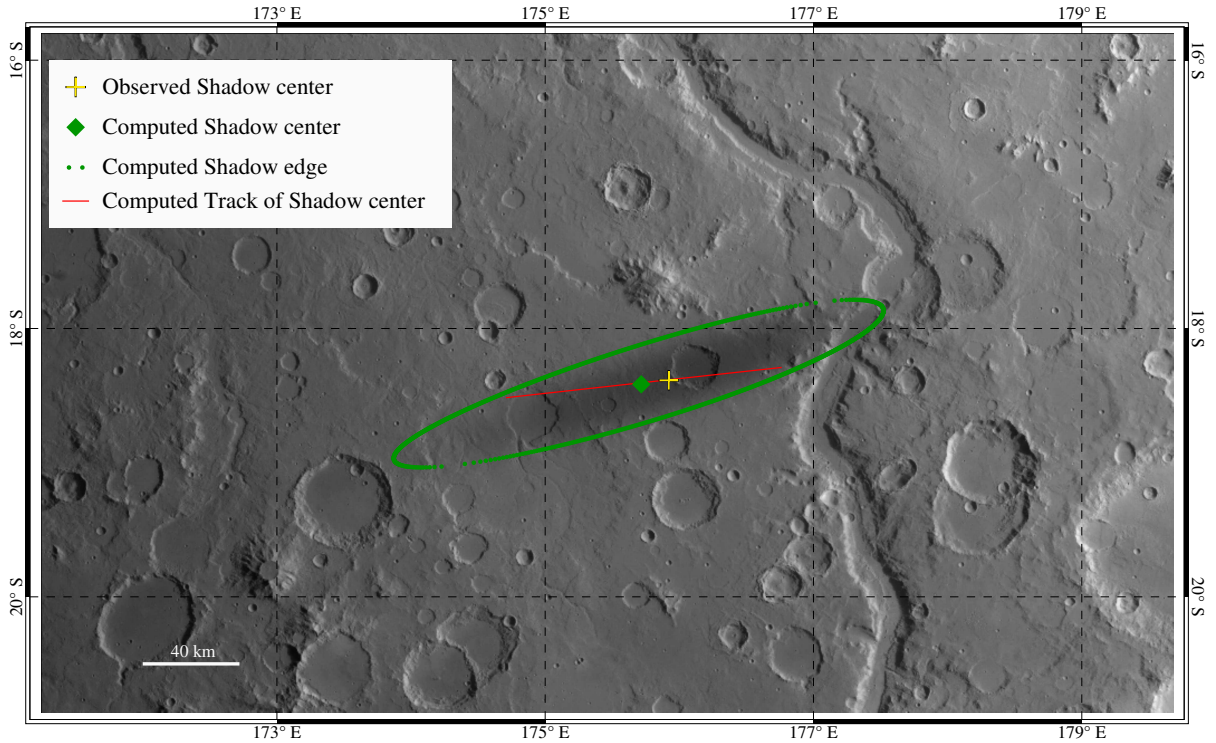


Figure 17: Reconstructed shadow ellipse (green) of orbit 2729 in comparison with the observed shadow center (blue). The yellow line marks the track of the reconstructed shadow ellipse center during the time of image acquisition.

the area in which the shadow is observed is relatively small and can be approximated by a plane. All further computations were executed in the assumed plane of the shadow.

Since the shadow is visible over several lines which were recorded over a certain time span, the predicted shadow ellipse was computed for all epochs between the line depicting the most southerly part of the shadow and the line showing the most northerly part of the observed shadow. Mostly the number of epochs was increased since there were obvious differences between the orbit model predictions and the locations of the observed shadow in the direction of motion of the spacecraft.

For each observed line a shadow ellipse prediction was computed and the CCD-line of the recording HRSC channel was projected into the shadow plane. The orientation of the CCD-lines of each channel is known with respect to the *HRSC HEAD Frame* from

the pre-flight camera calibration. Hence, it was possible to intersect the vectors from two pixels of the CCD-line through the focal point with the local surface on Mars. Through the two coordinate pairs a line was parameterized.

The predicted shadow ellipse and the CCD-line projection were then intersected in the plane. Hence, for each CCD-line up to two points were determined describing the edge of the predicted shadow ellipse at that epoch. When computing the intersection points of the projected CCD-line with the predicted shadow ellipse for all epochs during the recording time, a number of points are obtained which represent the outline of the predicted shadow. With fitting an ellipse to these points the center of the predicted shadow image is determined (Fig. 17).

Table 10: Differences of shadow observations in HRSC images to the JPL-model (Jacobson and Rush, 2006) and the ROB-model (Lainey et al., 2007).

Orbit model	along-track offsets	across-track offsets
JPL-model	2.2 km to 9.6 km	0.6 km to 10.5 km
ROB-model	2.8 km to 11.6 km	0.2 km to 10.3 km

The derived positions of the predicted shadow centers were compared with the observations and the positional offsets were studied. The offsets show again large random-like scattering, substantially larger than what was reported from the direct astrometric observations (Table 10 and results from Oberst et al. (2006)). This attests to the difficulty of mapping the shadow position on the ground, which is likely due to the undefined outline of the shadow. However, systematic offsets are seen along the track, which confirm that Phobos is ahead of its predicted position.

5.2.5 Results - Shadow Observations

It was possible to obtain astrometric information of Phobos from observations of its shadow on the Martian surface. 19 shadow observations obtained by the MOC and 9 observations of Phobos' shadow in HRSC images were analyzed. It was expected that such observations would independently verify previous and ongoing astrometric observations in fly-by images. Furthermore, it was anticipated that the analysis is independent from spacecraft pointing and position information.

Results of the observations in MOC images unfortunately suffered from large uncertainties and show unsystematic scatter between positions determined from different shadow images and ephemerides models. A reason for such diversifying observations may primarily be the resolution of the images combined with the shadow center finding error. Hence, results of the analysis of MOC shadow images are considered to be unreliable and too heavily biased when compared with the accuracy of current orbit prediction models.

However, the results of the shadow observations in HRSC images are in first order agreement with previous astrometric observations of Phobos, confirming that Phobos is ahead of its predicted position. Differences in the direction of motion are, compared to the orbit prediction models of Jacobson and Rush (2006) and Lainey et al. (2007), below the previously observed 12 km (Oberst et al., 2006), which was expected. The observed discrepancies show that the orbit models had improved. However, it was anticipated that the ephemerides models, in comparison to the previous ephemerides, would model the orbit of Phobos with a better accuracy and with more consistency than observed.

The reason why expectations on the orbit models are not met could be the applied model to derive the position of Phobos from the shadow observation. The model is based on a simple reconstruction of the shadow projection onto the Martian surface which limits the correct determination of Phobos' position in the sky. This becomes apparent when studying the across-track differences in comparison to the orbit prediction models. Relatively wide spreading offsets with no systematic behavior were observed (Fig. 16). Such a random discrepancy to the orbit models, which is indicating that Phobos is out of its orbit plane, is physically not feasible. Hence, the model to reconstruct the projection of Phobos' shadow would need further improvement.

During the analysis it became apparent that the simple model, used to obtain the desired information of Phobos' position against the stellar sky, is insufficient. A more accurate model was designed which included the use of predicted camera position and orientation information. However, since observed positions and predictions did not draw nearer – even with the improved model – and error bars were still of the same size, this approach to obtain astrometric informations was not further followed. A list of observation results can be found in the Appendix A in Table 24.

5.3 Fly-by Observations

A more straight forward possibility to determine the position of a planetary body in its orbit, is to analyze spacecraft image data picturing the body. Here it is important to have detailed information of the position and the pointing of the spacecraft as these parameters directly influence the quality of the positional information.

The center of mass is the reference point which one wants to observe when obtaining astrometric information. Determination of the COM of a body is commonly done by fitting an ellipse to the observed limb in the image data and computing the center of the ellipse. This method is only valid with the assumption that the center of mass and the center of figure coincide.

5.3.1 Fly-by Images

The apoapsis height of about 11,000 km of the highly elliptical, near polar MEX orbit reaches well beyond the orbit of Phobos (Jaumann et al., 2007). By the end of December 2008, MEX had observed Phobos during 107 fly-by maneuvers with average distances to Phobos of approximately 2,000 km (see Figure 18). Orbit periods of MEX and Phobos are quite similar, 6 h 43 min and 7 h 39 min, respectively, leading typically to multiple fly-bys in consecutive orbits followed by epochs of few or no close Phobos encounters (Oberst et al., 2006, 2008).

A data set of 326 SRC and some hundreds of HRSC images depicting Phobos or parts of its surface were obtained (Table 11). Due to the push-broom principle of the HRSC, which produces images over a period of time rather than obtaining an image in a single moment, images were not considered at all for this analysis. All SRC images were primarily considered for the astrometric observations. However, the suitability was constrained by a number of reasons. These are:

- (i) the lack of background stars observations,
- (ii) background stars observations only before *or* after the Phobos encounter,
- (iii) fly-by was too close and not enough surface features could be identified,

(iv) fly-by was too far away.

Images from fly-bys which fall under points (i) and (ii) were not used since the pointing of the camera or the stability of the pointing could not be controlled by any means (cf. Section 5.3.2). It was aspired to observe at least three control points for redundancy. Hence, images which fall under (iii) were often excluded from the analysis since the area depicted in one image was too small to measure the required number of control points. Images obtained from further distance (iv) could usually be used but were in some cases of too low resolution.

Table 11: Number of HRSC images depicting Phobos or parts of its surface and their ground resolutions. Status: December 2008

HRSC Channel	No. of Phobos Images	Resolutions [m]/pixel
nd	87	3.7 to 451
s1 & s2	51 each	3.9 to 474
p1 & p2	45 each	7.6 to 450
re	44	25 to 670
gr & bl & ir	45 each	25 to 670
sr	326	0.9 to 105

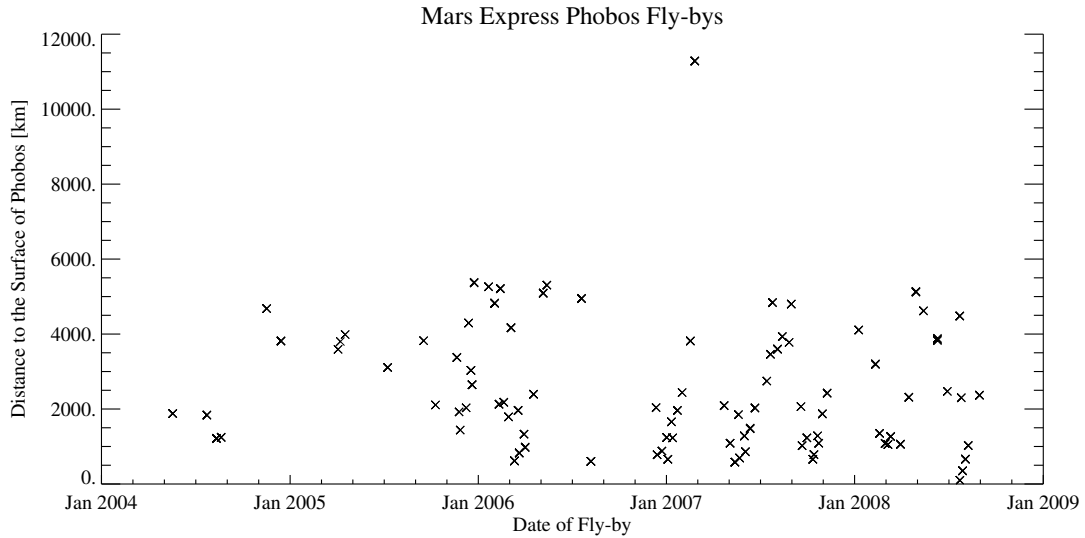


Figure 18: Fly-by distances during SRC observations. On average SRC images have pixel resolution of 50 m per pixel and below.

5.3.2 Pointing Verification

During a Phobos fly-by, the SRC is pointed at some fixed inertial point in the celestial sphere. A sequence of usually 8 images is recorded as Phobos enters the field of view (cf. Oberst et al., 2008). There is typically some freedom in the choice of the inertial pointing vector (within the plane containing Phobos and the spacecraft fly-by trajectory) to cover specific Phobos surface areas or to capture background stars. Background star observations have been obtained for all fly-by image sequences since mid 2005. As the background stars are normally observed in the first and in the last image of the sequence,

the observations can be used to verify the camera pointing and to control the stability of the camera pointing during one fly-by to detect possible pointing drifts.

Mostly the faint stars (visual magnitude $+4 < m < +10$) are captured in SRC's narrow field of view, which require dedicated long-exposure (516 ms) images. However, as many stars are much fainter mostly only one star is observed during one fly-by. Sometimes up to 4 stars are observed. The identification of the stars is thus unambiguous. Recognizing stars in an SRC image is also straight forward. The point spread function of the SRC depicts stars as a triangular feature rather than a point. Hence, a confusion of a star with hot pixels is unlikely (see Fig. 9).

The verification and controlling of the pointing is then achieved by measuring image coordinates of the background stars and comparing them with the predicted image coordinates, x_{St}, y_{St} , of the stars computed with the predicted pointing information of the spacecraft.

To compute the predicted image coordinates of the observed stars, the equations

$$\begin{aligned} \begin{bmatrix} X_{St} \\ Y_{St} \\ Z_{St} \end{bmatrix} &= \begin{bmatrix} f \cos(\alpha) \cos(\delta) \\ f \sin(\alpha) \cos(\delta) \\ f \sin(\delta) \end{bmatrix} \\ \begin{bmatrix} x_{St} \\ y_{St} \\ f \end{bmatrix} &= \frac{1}{pix} \begin{bmatrix} R_{J2S} \end{bmatrix} \begin{bmatrix} X_{St} \\ Y_{St} \\ Z_{St} \end{bmatrix} - \begin{bmatrix} x_0 \\ y_0 \\ 0 \end{bmatrix} \end{aligned} \quad (8)$$

were applied. Right Ascension α and Declination δ of the identified stars were registered in the Hipparcos (Perryman et al., 1997) and the PPM (Röser and Bastian, 1992) catalogs. The stellar coordinates from the star catalog were transformed into rectangular coordinates, X_{St}, Y_{St}, Z_{St} with the distance set to the focal length f of the camera. The focal length provides the correct scale for the coordinates. The resultant 3D-coordinates are still in the J2000 inertial frame and needed to be rotated with the matrix R_{J2S} to agree with the SRC frame orientation. This rotation matrix is derived from the predicted or reconstructed pointing of the camera which inherits any possible incorrect orientation information from the navigation data. To obtain pixel values, the metric coordinates are additionally divided by the metric pixel size, pix , and the coordinates are translated to the origin of the image coordinate frame.

Two star catalogs were used for the identification of the stars. While the Hipparcos catalog consists of 118218 star entries with an overall higher accuracy than the PPM catalog (Perryman et al., 1997), the latter catalog has a higher number of star position entries (Röser et al., 1994) with a wider range of visual magnitudes (cf. Tab. 12). Visual comparison of star position entries in both catalogs for a given star implied that positional differences between the two star catalogs are below the measurement accuracy of one SRC pixel.

Discrepancies between the predicted location of a star in the image and its observed position relate to two rotations in the camera orientation. A difference in the sample coordinate can be compensated by a rotation around the X -axis. A rotation around the Y -axis results in a line shift.

For fly-bys where just one star could be observed it was assumed that image rotation about the Z -axis could be neglected (an assumption that was later verified by the Phobos orientation in the images).

Table 12: Comparison of the Hipparcos (Perryman et al., 1997) and the PPM (Röser et al., 1994) star catalogues.

Catalogue	Hipparcos	PPM
no. of stars	118 218	468 586
stars/deg ²	~ 3	~ 7.8
mean err. position	0.77 / 0.64 ^a	0.11 / 0.27 ^b
Visual Mag.	9.0	13.5

^a $\sigma_\alpha \sigma_\delta$ in milliarcsec, at J1991.25^b σ in arcsec, dependent on the hemisphere, at J1990

The reduction of the background star observations show that the nominal pointing data are on average correct to 25 pixels, while a maximum offset of 45 pixels was observed and 3 gross outliers were found in orbits 682, 2706, and 2739, where observed and predicted image coordinates differed by up to 200 pixels. The relative pointing during one fly-by, on the other hand, was found to be very stable with an average positional difference of the depicted star of 3 pixels between the star observations in the first and the last image of a fly-by. Again, one outlier was found (orbit 3245), where no camera drift was registered in the nominal pointing information but star positions in the images differed by 44 pixel.

5.3.3 Center of Mass Measurements

The origin of the body-fixed frame of a planetary body is by definition equal to the center of mass of this body (Seidelmann et al., 2005). A position vector to this body would point to the predicted position of the COM since this information is recorded in the ephemerides model. Usually the assumption that the center of figure is the same point as the COM is also made in a first approximation. Hence, when observing the position of a planetary body primarily the position of the COF is determined.

Phobos' position in its orbit was previously observed in SRC images by using an ellipse overlay projected onto the image containing Phobos (Oberst et al., 2006). The ellipse overlay is a result of the computed intersection of the triaxial ellipsoid model of Phobos with the image plane. Its predicted position in the image is computed from the position and pointing data of the camera and the ephemerides model in question, similar to the determination of the predicted star positions in the image (Eq. 8). A fit of the ellipse onto the observed body is then performed leading to a new position of the ellipse. Assuming that Phobos would be a perfect ellipsoid and the projected ellipse fits perfectly onto the observed limb, the center of the ellipse would then be located over the COF of Phobos in the image. However, as Phobos is no triaxial ellipsoid the projected ellipse does not necessary fit well onto the observed limb, leaving the observer with some degree of freedom to position the ellipse.

Much effort was made to improve the method to determine the line/sample coordinates of the Phobos COM in the images. Craters are well defined surface features and on Phobos the 3D-coordinates of 315 craters were determined by Duxbury and Callahan (1989b) and Duxbury (1991). These control points, which are believed to be known with respect to the COM of Phobos, were used to observe the COM coordinate in the image indirectly but redundantly.

The control points of the Duxbury (1991) control network were defined to be located at the center of the mean local surface of the crater rims rather than at the crater floor. Duxbury and Callahan (1989b) used an ellipse overlay and interactively varied the ellipse shape to accommodate this definition and to be able to also consider craters under oblique view.

To observe these control points, a number of line/sample coordinate pairs were collected along the depicted crater rim in the image. These points were used to fit an ellipse to the crater rim. It was assumed that the center of the ellipse represents the center of the crater on the local plane, which complies with the control point definition. The image coordinates of the ellipse centers were registered.

The correct identification of the control points was supported by overlaying the predicted positions of the control points onto the image and bringing them into best agreement with the observed surface features. Thus, misidentification of points could be ruled out. On average 9 control points (minimum: 3) were identified and measured in each image considered for this analysis.

According to the differences between observed and predicted background star observations, the observed line/sample coordinates, x_m, y_m , of the control points were corrected. Similar to the method to determine the predicted star position in the image, the image coordinates of the control points were computed. A vector from Mars Express to the control point \vec{X}_{MEX-CP} was computed by adding the control point coordinate, known with respect to the body-fixed frame, to the predicted vector between MEX and Phobos $\vec{X}_{MEX-Pho}$ (Eq. (9))

$$\vec{X}_{MEX-CP} = \vec{X}_{MEX-Pho} + \vec{X}_{CP}. \quad (9)$$

The position of Phobos with respect to the spacecraft, $\vec{X}_{MEX-Pho}$, was computed using the orbit model for Phobos, the reconstructed trajectory information for MEX, the previously determined pointing correction, and a light time correction. A light time correction was applied such that the geometric state of Phobos at the time registered in the image label minus the time light traveled from Phobos to Mars Express was computed. \vec{X}_{MEX-CP} is then transformed into spherical coordinates and the range is substituted by the focal length of the camera. Substituting the X_{St}, Y_{St} and Z_{St} in Eq. (8) through the components of \vec{X}_{MEX-CP} the predicted image coordinates of the control points were computed.

These predicted image coordinates, x_p, y_p , were then transformed to fit the measured image coordinates, x_m, y_m , using the functional model:

$$\begin{bmatrix} x_m \\ y_m \end{bmatrix} = s \begin{bmatrix} R(\alpha) \end{bmatrix} \begin{bmatrix} x_p \\ y_p \end{bmatrix} + \begin{bmatrix} x_{trans} \\ y_{trans} \end{bmatrix}, \quad (10)$$

where the free parameters, rotation $R(\alpha)$, scale s , and translation, x_{trans}, y_{trans} , including their errors, were determined using an iterative least-squares analysis involving all identified surface features of one image at a time. The analysis converged rapidly after only 3 to 4 iterations. Furthermore, it indicated that the scale and rotation parameters could be neglected in all cases, implying that the apparent size and orientation of Phobos were correct to first order.

In the same way, the Phobos COM - at the origin of the Duxbury and Callahan coordinate system - was converted to predicted image space coordinates. The transformation parameters from above were used to calculate the corrected image position and, finally, the stellar coordinates of the COM of Phobos with respect to the spacecraft position.

5.3.4 Results

135 positional measurements of Phobos were completed covering a period of more than 3 years of observations of Phobos in its orbit. For the first time it was possible to obtain astrometric information on Phobos over such an extensive time span. Uncertainties of the determined stellar coordinates were significantly reduced by controlling the camera pointing through background star observations. Furthermore, redundant position information was obtained through positional measurements of surface features, of which 3D-coordinates are known with respect to the center of mass. This additionally constrained the observations.

The uncertainties of the measurements σ were estimated as the sum of accuracies of the determined transformation parameters σ_t , the camera pointing σ_p , a term that is related to the spacecraft position σ_{sc} , and range r

$$\sigma = \sqrt{\sigma_t^2 + \sigma_p^2 + \left(\arctan \frac{\sigma_{sc}}{r}\right)^2}. \quad (11)$$

The accuracy of trajectory information of Mars Express in its orbit, σ_{sc} , was reported to be better than 200 m (Jaumann et al., 2007). However, for this analysis the more conservative previously reported value of $\sigma_{sc} = 500$ m was used (Oberst et al., 2006). The overall uncertainty of the MEX position data is very likely to be of the order of the two estimates, or possibly even lower. Large errors of the camera position would reflect in the astrometric observations of Phobos. Indications for such an error are only occasionally observed (cf. Fig. 20).

Fly-by distances, r , which ranged from 660 km to 11,000 km, were computed from the orbit prediction models and assumed to be correct to first order. The values σ_t , and σ_p , were determined for each individual image within the least-squares adjustment solving for the transformation parameter. Resulting estimates of the total errors range between ± 0.002 and ± 0.035 degrees, which translates into Phobos positional errors in the object space of ± 0.1 km to ± 0.5 km, perpendicular to the line of sight.

Observed positions of Phobos show a relatively constant offset to orbit prediction models (see Figure 19). A weak trend of increasing differences between observations and prediction model can be observed. The red marked observations display the results of the astrometric observations from Phobos shadow images. These clearly differ from the observations in fly-by images and the scatter is even more apparent in the comparison.

No significant discrepancies of the fly-by observations to the JPL orbit prediction model were observed since the determined differences are all within the ± 5 km uncertainty range of the orbit model. Comparing the observations to the ROB ephemerides model the offsets exceed the estimated accuracies of the orbit model of ± 1 km on average by approximately 37% of the error estimation (cf. Table 13).

Figure 19 displays the differences between the Lainey et al. (2007) orbit prediction model and the observations with respect to the predicted stellar coordinates. The metric offset

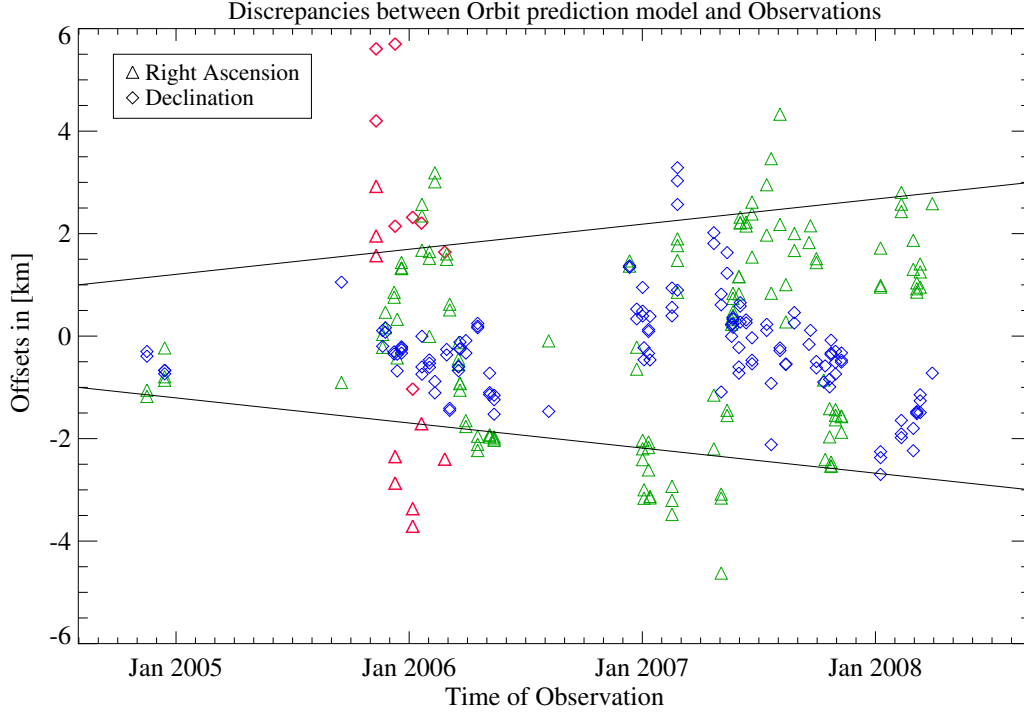


Figure 19: Fly-by discrepancies compared to the ROB orbit prediction model (green and blue marks). Plotted differences are in kilometers with respect to the stellar coordinates of right ascension and declination. Red marks display the results of the shadow observations for comparison.

Table 13: Estimated accuracies of the JPL- and ROB orbit prediction models.

Published by	Along-Track	Across-Track
JPL	± 5 km	± 2 km
ROB	± 1 km	± 1 km

was computed to be perpendicular to the line of sight. Differences are in some cases much larger than the primarily assumed accuracy of ± 1 km of the ROB orbit model.

5.4 Validation of Orbit Models

The differences with respect to the stellar coordinate frame in Right Ascension and Declination (as in Figure 19) do not allow to draw any conclusion on the direction of the offset with respect to the body-fixed coordinate frame of Phobos and thus to relate the offset to the direction of motion- , radial- , and out of orbit plane-discrepancies.

The observed two dimensional translation vector in the images plane is the projection of the corresponding 3D-vector in space. This vector can be freely oriented in space. Thus an unambiguous determination of the components of this vector is impossible without an assumption.

A first approach to determine the 3D-components of the projected translation vector, was based on the empirical determination of these components. It was assumed that the offset

vector in space,

$$\begin{pmatrix} X \\ Y \\ Z \end{pmatrix} = \begin{pmatrix} a + \sin(TA + b) * c \\ d \\ e + \sin(TA + f) * g \end{pmatrix}, \quad (12)$$

with respect to the Phobos body-fixed frame, consists of X and Z elements which include a constant term and a term dependent on Phobos' position, expressed by the true anomaly TA , in its orbit. The Y -component and thus the velocity was assumed to have a constant offset (Eq. (12)). Orbital variation of the velocity due to the eccentricity are assumed to be modeled correctly in the existing ephemerides model. The X -element of the vector in equation (12) represents a variation of the size of the orbital ellipse as well as the eccentricity of the orbit. A varying inclination of the orbit is modeled with the Z -component of the vector.

All seven free parameters of equation (12), a, b, c, d, e, f , and g were varied over a range of values. Phobos was then shifted along this vector and it was tested which combination of the free parameters minimizes the discrepancies to the observations. This empirical determined vector, $\vec{X}(a, b, c, d, e, f, g)$, which had the minimum discrepancy to all the observations, was assumed to represent the mean difference between orbit prediction model and all observations in object space.

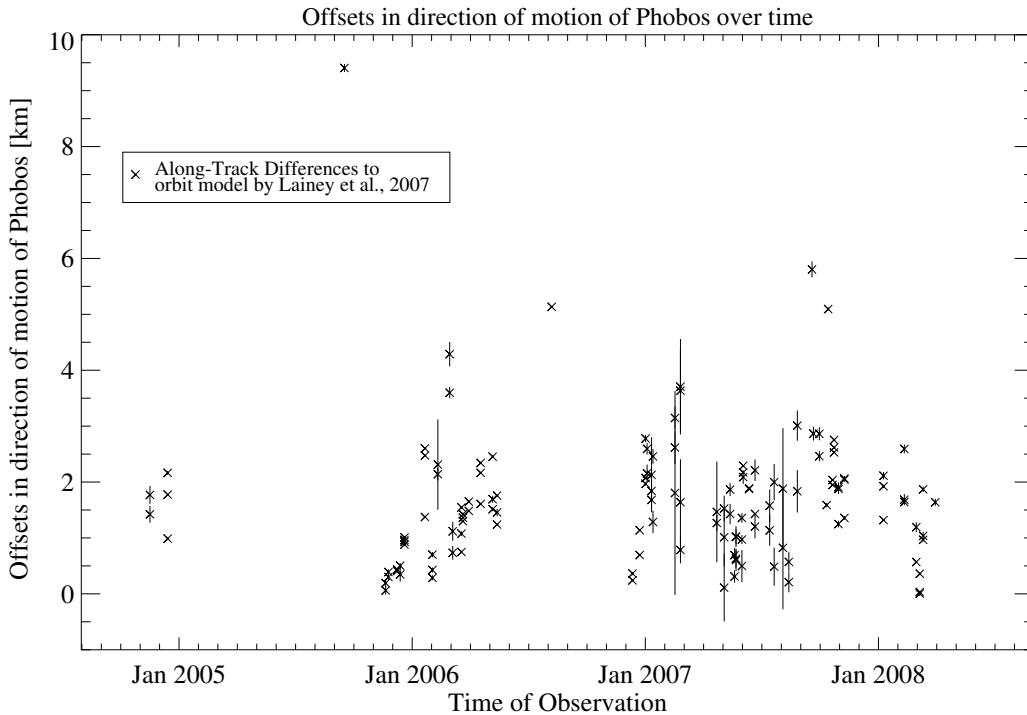


Figure 20: Offsets of observations to the orbit model Lainey et al. (2007) in the direction of motion of Phobos. Positive values indicate that Phobos is ahead of its predicted position.

The derived vector, here as an example for the orbit model of Lainey et al. (2007)

$$\begin{pmatrix} X \\ Y \\ Z \end{pmatrix} = \begin{pmatrix} 0.1 + \sin(TA + 1.0) * 0.1 \\ -1.6 \\ 0.0 + \sin(TA + 1.0) * 0.4 \end{pmatrix}, \quad (13)$$

indicated that the component radial direction to Mars, X , is smaller than the overall error estimate of the observations. As a consequence, it is assumed that the observed

X-components of the vectors represents only minor random scattering and no systematic or significant offset. It can be neglected in further analysis.

Thus, it was possible to determine the other two components of the discrepancy vector for each fly-by through the translation vector which was observed in the image. To model the two components, Y and Z , of the offset vector for each fly-by, normalized vectors along the coordinate axes were projected into the image plane and compared to the observed translation of the COF of Phobos in the image. The Y - and Z -component of the vector could thus be determined (see Fig. 20 for along-track differences Y).

The average of the along-track discrepancies in Figure 20 equals the empirical derived value of 1.6km for the Y -component when compared to the ROB-model. Astrometric observations show a consistently positive difference to the ephemerides models, indicating that Phobos is ahead of its predicted position.

Table 14: Comparison of orbit models with fly-by observations. Positive along-track offsets indicate that Phobos is ahead of its predicted position.

Orbit Model	along-track offsets	across-track offsets
ROB-model	+1.6km	± 0.3 km
JPL-model	+2.6km	± 0.5 km

Comparing the two orbit prediction models, released in 2006 and 2007, only small differences between them were observed which are within the error bands of both orbit models (cf. Tables 13 and 14). These small discrepancies are very likely caused by the use of a different set of planetary constants, other gravity field coefficients for Mars, the inclusion of different perturbations on the satellites and slightly differing sets of observations (Table 15).

5.5 Secondary Results

While the discussed results already supply good information about the orbit prediction models of Phobos itself, astrometric observations also provide valuable information to improve the knowledge of weakly constraint physical parameters of Phobos and also Mars.

The group at the ROB for instance fitted the Phobos orbit model to the MEX observations and solved for the gravitational coefficients C_{20} and C_{22} of Phobos. This led to a solution of a negative C_{22} coefficient, which is physically not possible. To resolve this disagreement a possible misalignment between COF and COM was allowed within the fitting process. The solution indicates that the two points differ by approximately 7m.

The ROB group also tried to find a solution for the time dependent Martian $J_2(t)$ gravitation coefficient through a fit to the new positional observations. The coefficient is described as function of time due to its variation caused by seasonal evaporation and sublimation of the polar ice caps over the Mars year (Smith et al., 2001b; Konopliv et al., 2006). Even though a solution was found it was not well constraint. It was speculated that the accuracy of the observations might still be too low.

Another example is the solution for the longitudinal librational of Phobos. The JPL group also tried to fit the C_{20} and C_{22} coefficients of Phobos during the fit of the orbit model to astrometric observations. They obtained also a negative result for the C_{22} coefficient.

Table 15: Differences between the ROB-model (Lainey et al., 2007) and the JPL-model (Jacobson and Rush, 2006)

Orbit model Criteria	ROB-model	JPL-model
Mars Gravitational field	MGM1041C up to degree 10	MGS95J (Konopliv et al., 2006) up to degree 8 for zonal harmonics and degree and order 5 for tesseral har- monics
Planetary Con- stants	DE406	DE414
Tides	Tides for both satellites are modelled as potential	Tides raised by Deimos are ignored
Available Obser- vations	<ul style="list-style-type: none"> – HRSC/SRC – No MRO – No MGS MOLA – all previous observations 	<ul style="list-style-type: none"> – HRSC/SRC – MRO data – MGS MOLA – earthbased observations from Ta- ble Mountain Observatory – all previous observations

The latest orbit prediction model MAR080 includes a forced libration of 1.06 ± 0.02 deg to obtain a positive gravitational coefficient.

6 Control Point Network on Phobos

Ground control points of a planetary body are points of which the 2D- or 3D-coordinates are known with respect to the body-fixed rotating frame. Their coordinates are not changing over time. The location and orientation of the body-fixed frame is changing with respect to the inertial frame J2000 (see also Section 4.2). The motion of bodies in the planetary system with respect to the inertial frame, and thus also of the body-fixed frames, is calculated and documented in ephemerides tables.

Control points need to be defined as re-identifiable points which can be surface features but also locations of artificial objects such as planetary lander coordinates. In any case a planetary control point network should consist of points visible from space.

The computation of ground control point coordinates relies on the collinearity equations which require at least an estimation on the camera position and pointing. These data, with respect to the body-fixed frame of the planetary body, are determined through the ephemeris model of the planetary body and the observed or modeled trajectory of the spacecraft. Hence, the absolute accuracy of the control points is dependent on the method used to determine the control point, on the accuracy of the ephemerides model of the body, and on the orientation information of the camera. However, the relative uncertainty can be much smaller depending on the image data and the quality of the relative orientation of camera view points available.

6.1 Previous Control Networks

Up to the current date, the Viking Orbiters, which operated in orbit from 1976 to 1978 (VO2) and 1980 (V01), were the only spacecraft to observe the entire surface of Phobos in stereo with resolutions below 200 m per pixel. First attempts to establish a control point network were based on the Mariner 9 images which covered approximately 70 % of Phobos' surface (Duxbury, 1974). Coordinates of 38 control points were determined from this image data set (Figure 21).

Almost a decade after the end of the Viking orbiter missions, Duxbury and Callahan (1989b) computed the locations of 98 control points from Viking orbiter images, using a similar technique as previously described (Duxbury, 1974). An overlay of ellipses was used to model crater rims in the images. Control points were thus defined to be the center of the crater on the mean local surface of the crater rim. The latest control network was the network computed in 1991 (Duxbury, 1991), consisting of 315 identified surface points, exclusively craters. Accuracies range from ± 74 m to ± 900 m. The variance in accuracies is very likely caused by the inaccurate navigation data of the Viking Orbiter (Zeitler, 1999). Points are again defined as the center of a crater "lid" rather than at the crater floor.

The control point network is an important tool for further analysis. Shape models can be computed to analyze physical parameters. For example, with the existing spherical harmonic function model of degree and order 8 (Duxbury, 1991) estimates of the volume, bulk density and moment of inertia values were derived. Also the general rotational state, in particular the forced libration, of Phobos can be observed with a control network.

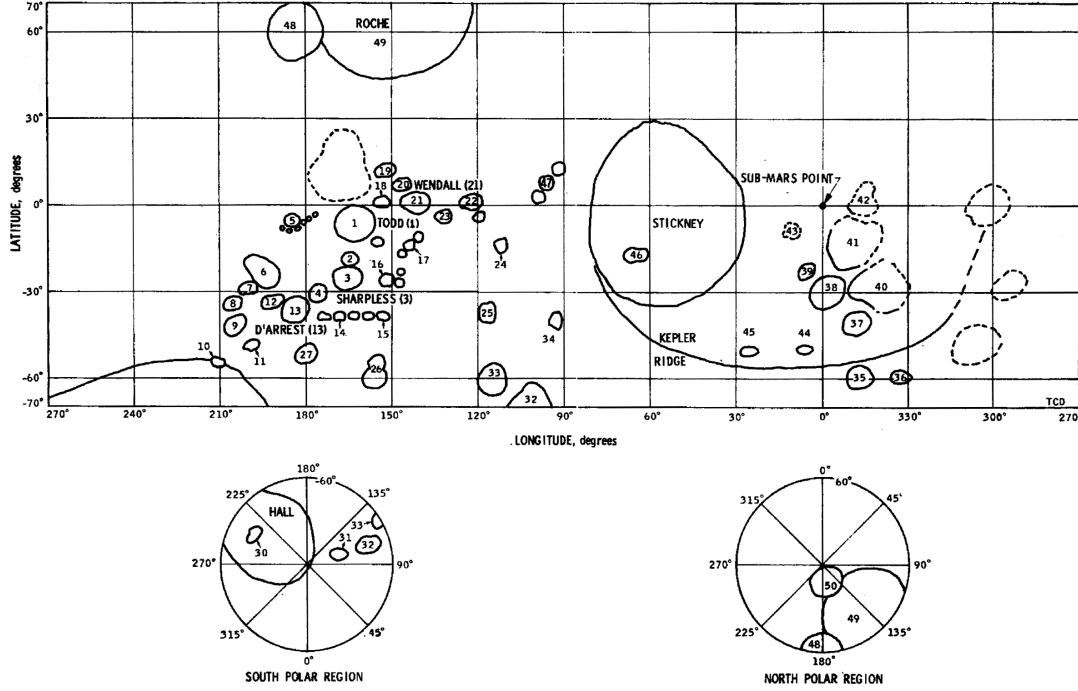


Figure 21: The first control network of Phobos computed by Duxbury (1974). It consists of 38 control points and covered only parts of Phobos' surface.

6.2 Determination of Control Point Coordinates

6.2.1 Available Image Data

To establish an independent global control network, stereo images for the entire body are required. As the relative accuracy of the control point coordinates is expected to be in the order of the pixel resolution of the image data used for the determination, stereo images should have a resolution higher than the best accuracy of the previous control network. Hence, an image data set is required, which covers Phobos globally in stereo, with an overall better resolution than 74 m per pixel.

The HRSC acquires stereo information during one fly-by and would thus be predestined for the acquisition of 3D-coordinates of object points. However, the average distance during Phobos fly-bys is about 2000 km. Images obtained from such a distance have a primary resolution of 80 m per pixel. An additional constraint is put on the resolution of HRSC stereo information as during most imaging operations only the nadir channel is obtaining images in full resolution (Table 4). The other channels which can be used for stereo analysis (s1, s2, p1, and p2; cf. Table 3) are operating in a pixel summing mode which leads to a decrease of the resolution by a factor of usually 2 or 4, and in some cases 8. The expected accuracy of a control point would then be in the range of lowest pixel resolution. Considering that the stereo or photometry channels are operating in a 2 by 2 pixel summing mode and the resolution of the resulting images should be better than ± 74 m, only HRSC images from fly-bys with a distance of less than 950 km can be used.

The SRC on the other hand, is magnifying objects in comparison to the HRSC by a factor of 4.33 (Oberst et al., 2008) and has therefore a much higher pixel resolution. However, it is a single frame camera aimed towards a fixed point in the sky during one fly-by “waiting” for Phobos to pass through the field of view. For this reason no stereo information is available from SRC images of one Phobos fly-by, even though consecutive

Table 16: Advantages and disadvantages of the different data sets regarding control point determination.

Data set	Pro	Contra
HRSC	<ul style="list-style-type: none"> - Stereo images during one fly-by - Automated determination of conjugate points possible 	<ul style="list-style-type: none"> - Suitable pixel resolution only from fly-bys with less than 950 km distance - No global coverage
SRC	<ul style="list-style-type: none"> - High resolution images for large areas - Can easily be combined with VO data set - Stereoscopic analysis possible 	<ul style="list-style-type: none"> - No global coverage - No stereo information from one fly-by - No automated determination of conjugate points
VO	<ul style="list-style-type: none"> - Can be combined with SRC images - Covers areas of Phobos which were not observed by SRC or HRSC - Stereoscopic analysis possible - Global coverage 	<ul style="list-style-type: none"> - Limited coverage by very high resolution images - No stereo information from one fly-by - Geometric correction necessary - inaccurate navigation data

images of one fly-by do overlap at times. Owing to the large number of fly-bys a stereoscopic analysis is possible. Approximately 75 % of Phobos' surface is observed in multiple SRC images obtained under different viewing angles and from different fly-by distances. Since images covering similar areas were obtained during different fly-bys, light conditions are in most cases very different. Shadows are casted in different directions and are of unequal length. Furthermore, pixel resolutions of the images vary, such that conjugate points can not be determined through automated processes. Global coverage of Phobos through SRC images could not be achieved yet (Figure 25). Fortunately, the area, which was not observed by the SRC nor by the HRSC, between 180° and 270° West and 90 degrees North, -90 degrees South was observed with very high resolution by the Viking Orbiters. VO images with very high resolution depict areas of 20 by 20 m per pixel.

The visual imaging systems (VIS) on the VOs were framing cameras. Before images of the VOs can be used for photogrammetric purposes they need to be geometrically corrected (Zeitler, 1999), resseau marks removed, and *salt'n pepper* effects – blemish or hot pixels which are clearly visible as white or black pixels – need to be corrected (see Figure 22). Each VIS on-board the two orbiters had two optical systems. Since the angular separation between the two cameras is too small, the VOs could also not gather stereo information during one fly-by (cf. Section 3.2.1). Again owing to the sheer number of close fly-bys a 3D-analysis of the VO data set is possible.

The various aspects of the properties of the different image sets led to the conclusion that the only reasonable way to determine a global control point network is by using SRC and Viking Orbiter images together. The two data sets are both obtained by framing cameras. Resolutions of the images do vary but are on average similar to each other and better than the highest accuracy of the previous control network. Global coverage with the highest resolution images of Phobos is achieved when combining SRC and VO images.

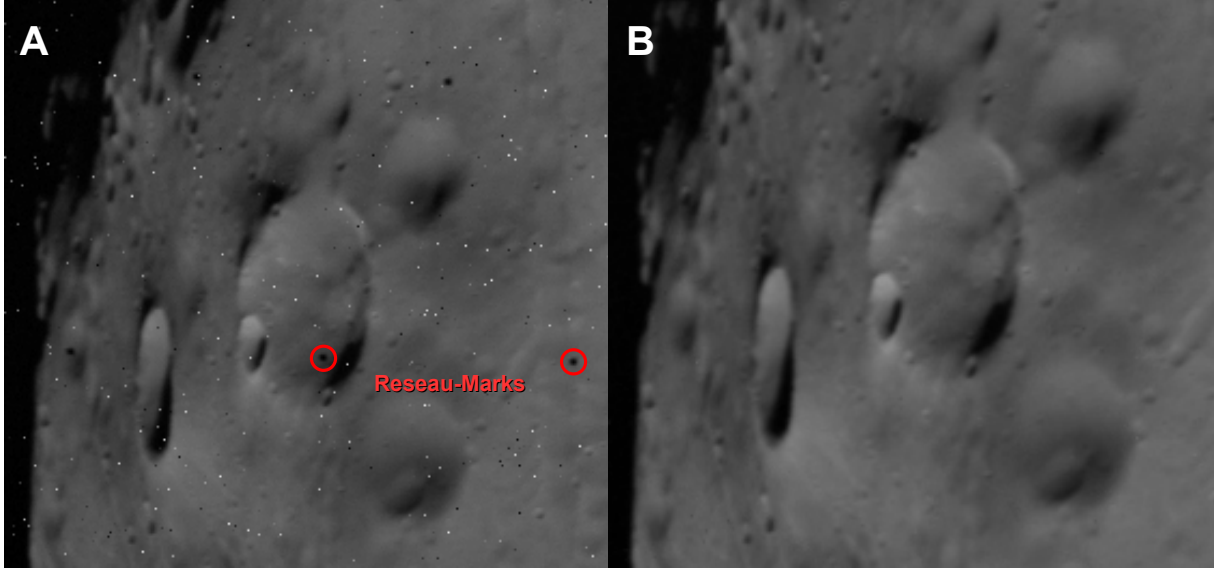


Figure 22: Part of a Viking Orbiter image before (A) and after (B) geometric correction, reseau removal, and Salt'n Pepper removal. The white and black pixels in image (A) are called salt and pepper.

6.2.2 Point Measurements

Conjugate points were observed manually in the different images. This was necessary due to the limited success rate when applying automated algorithms to determine conjugate points on the data set. Furthermore, it should be possible to clearly identify the points for later use. Such a constraint cannot be realized by current automated matching algorithms.

The location of a control point was determined by observing the center of craters at the crater floor. This definition of the control points does not comply with the previous control point definition for Phobos (Duxbury, 1974; Duxbury and Callahan, 1989b, and Section 6.1). However, while the previous network analysis might not have permitted to observe small features in the images, due to image data of lower resolution, it is now possible to observe such features, even features within large craters. It is expected that control points located on the crater floors represent Phobos' shape in more detail.

The control points were observed in the image with the software tool *TP* which directly saves the image coordinates in line/sample pixel values to a file. The software permits to load 12 images simultaneously and to view three images at once. 53 SRC images were selected for control point observations. The selection was driven by different requirements. These are,

- (i) Images should overlap with at least one other image,
- (ii) Angular separation between the spacecraft locations with respect to the COM should be larger than 5 degrees,
- (iii) Resolution should be as good as possible,
- (iv) Image should extend the covered area.

Images were grouped into five sets to accommodate the 53 SRC images within the software. Line/sample coordinates were primarily observed within one group of images but also between the different image groups to ensure a tight cross connection between the images. VO images were handled as a separate image group. Later image coordinates of conjugate points in the overlapping areas were observed to be able to combine the two data sets. 16 VO images were used to fill the area not covered by the SRC. Line/sample coordinates of

665 points were observed in both data sets.

6.2.3 Computation of Coordinates

The adjustment was computed without a re-determination of the position of the COF. In 2008 a new orbit prediction model was released which was fitted to all spacecraft astrometric observations, including the first spacecraft observations obtained by Mariner 9 and results of this study (Willner et al., 2008a), as well as doppler tracking data of the Viking and *Phobos 2* missions (Jacobson, 2008). The model, *MAR080* shows discrepancies to the observed position of Phobos on the order of ± 1 km, well below the estimated error of this ephemerides model. It is assumed that the new ephemerides model of Phobos is correct to the required accuracy and a re-determination of the COF is not necessary during the control network analysis.

Hence, only the position and orientation information of the spacecraft with respect to the body-fixed Phobos reference frame are improved to minimize the residuals of the object points. This information is based on the predicted position of Phobos from the ephemerides model and on the predicted or reconstructed trajectory of the spacecraft and has a strong influence on the accuracy of the resulting object points.

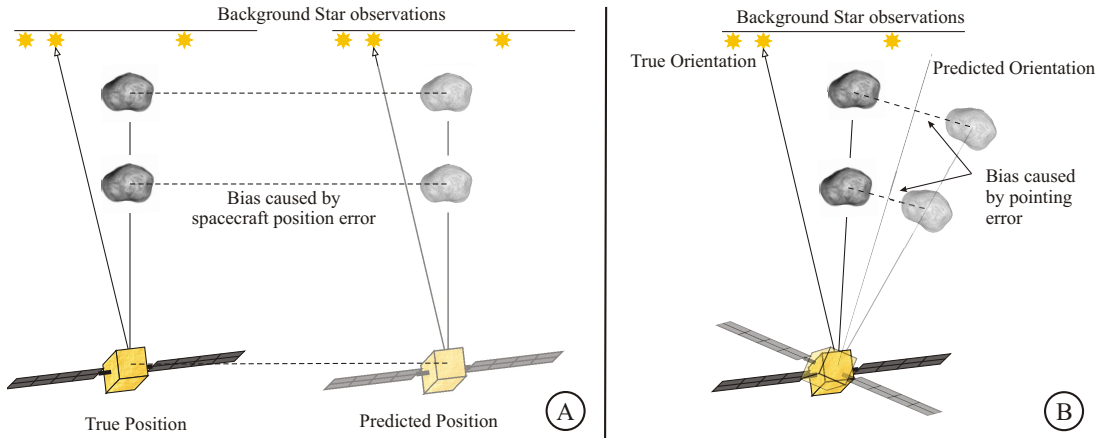


Figure 23: Uncertainties in object space depending on the error source.

The spacecraft position has a one-to-one influence on the position of the observed point, e.g. if the spacecraft position is shifted by 500 m the ray of the observations is also shifted by 500 m. It is influencing the observation with the same magnitude from all distances. An inaccurate pointing on the other hand biases the observation increasingly with increasing distance to the observed object (cf. Figure 23). For all bundle block adjustments of the SRC and the VO images it was primarily assumed that the position was almost perfectly known. Uncertainties of the pointing data were given more freedom such that small position errors could be compensated by rotations of the camera.

To detect gross errors in the predicted orientation of the cameras, least-squares bundle block adjustments were computed for both data sets separately. Orientation data for the SRC was of good quality and could directly be used to determine object point coordinates in the bundle block adjustment. However, normalized residuals indicated, in some cases, larger errors than the preliminary assumed uncertainties for camera orientations. Significantly improved results were computed after an adopted weighing scheme, allowing for much larger corrections of the observations in question, was applied to the camera position and pointing data.

The least-squares adjustment of the VO data set was not successful applying the orientation information provided by NASA. Hence, the camera orientation data of the Viking Orbiter images were improved prior to the adjustment. The pointing data were improved by fitting the predicted limb position to the observed position of Phobos in the images. This corresponds to rotations about two axes of the camera. Very high resolved images do not necessarily depict parts of the limb. Therefore, an overlay was produced, containing the control point positions of the Duxbury (1991) control point network, which was then fitted to the surface features.

Introducing the improved pointing information into the adjustment 3D-coordinates of the control points can be computed. It is concluded, that the uncertain orientation of the VO data set caused the failure of the adjustment prior to the improvement of the pointing. This observation is in agreement with previous observations by Zeitler (1999), who reported of erroneous orientation information for the VO spacecraft. To improve results of the adjustment the weighing scheme was again adjusted according to the computed normalized residuals.

The adjustment of the VO data set was very sensitive to small changes of the weighing scheme. As a consequence and due to the uncertain orientation data of the VOs, the bundle block adjustment including the SRC and VO observations was primarily computed solving for the object point coordinates and the Viking orbiter orientation data. In a second step the adjusted orientation data of both data sets was used to compute the object point coordinates through forward ray intersection (Fig. 24).

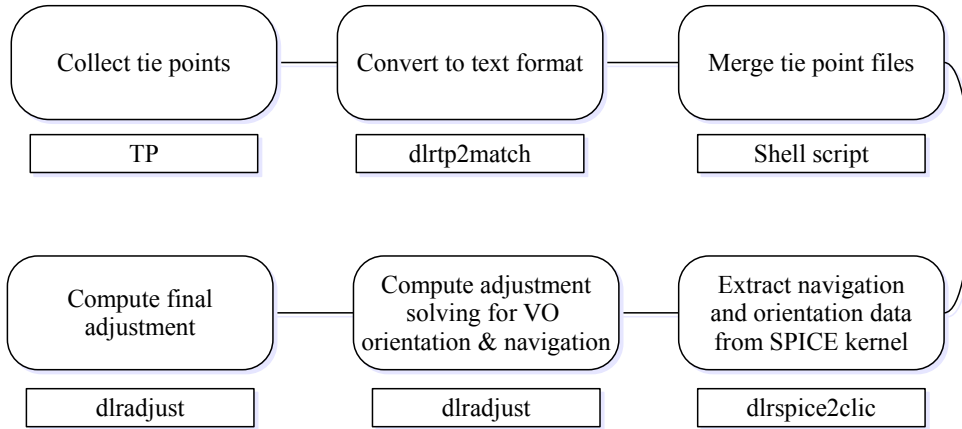


Figure 24: Flow chart of control point analysis.

6.2.4 Results

SRC images, which were used for this analysis, had pixel resolutions ranging from 5 m/pixel to 48 m/pixel and an average resolution of 17 m/pixel. VO images that were used had resolutions between 6 m/pixel and 77 m/pixel with a mean resolution of 17 m/pixel. A total of 665 points were observed 3898 times with a minimum of 3 observations and a maximum of 14 observations, but on average 6 observations per point in both image data sets.

Mean object point accuracies σ_x , σ_y , σ_z of 39.6 m, 34.6 m, and 36.1 m, respectively, were computed for control points measured in SRC images when adjusted without the VO data

set. An uncertainty of 1 pixel for the image coordinate observations was assumed.

Object point coordinates with considerably higher uncertainties were computed when computing 3D-coordinates of points observed in VO images only. Mean accuracies of $\sigma_x=122.5$ m, $\sigma_y=94.1$ m, and $\sigma_z=114.2$ m were determined attesting for a weak geometry of the observations and the uncertain orientation of the VOs.

Table 17: Object point accuracies for the different bundle block adjustment models.

	SRC			Viking orbiter		
No. of points obs.	2989			871		
	x	y	z	x	y	z
σ_{max} [m]	91.7	56.1	63.6	156.6	156.2	192.0
σ_{min} [m]	17.8	13.2	14.6	115.0	86.5	109.0
σ_{mean} [m]	27.1	17.2	19.5	122.5	94.1	114.2
Combined Adjustment of SRC and Viking						
No. of points obs.	3898					
	x	y	z			
σ_{max} [m]	92.26	103.28	79.93			
σ_{min} [m]	8.47	7.24	7.87			
σ_{mean} [m]	21.24	16.19	16.70			

The joint adjustment of the SRC and VO data sets was computed in two stages. In a first step, the least-squares bundle block adjustment was used to solve for the orientation of the VO images, based on the observation of the conjugate points and the orientation of the SRC images. The data sets were tied to one another through conjugate points in overlapping areas. Solutions for the 3D-coordinates of the control points as well as the unknown camera positions and pointing information of the VO were derived. The orientations of the SRC images were also improved but only within the limits of the assumed errors. The computed camera orientations for SRC and the VO cameras were then used to determine the object point coordinates of the GCPs in a second bundle block adjustment. A Baarda gross error detection was applied (Baarda, 1968) to rule out misidentified point observations. Uncertainties of the 3D-coordinates could be reduced slightly for points observed in SRC images. An improvement by a factor of approx. 6 for points in Viking images was observed when computing the combined data set (cf. Table 17).

Figure 25 shows that most uncertain points are located within the area which is covered by Viking Orbiter images. Since the average pixel resolution of the VO images is comparable to the pixel resolution of the SRC images one could argue that this should not be the case. However, the geometric correction and the uncertain navigation information are explaining the lower accuracy of control points in this area.

Another area indicating slightly higher uncertainties of the control points is located between 5° to 35° West and 0° to 25° North. This area is covered by a number of images. All images display this area under different but very oblique views. Points with larger uncertainties can often be found in areas of the terminator. It is assumed that these are the reasons for the lower accuracy of control points in this area.

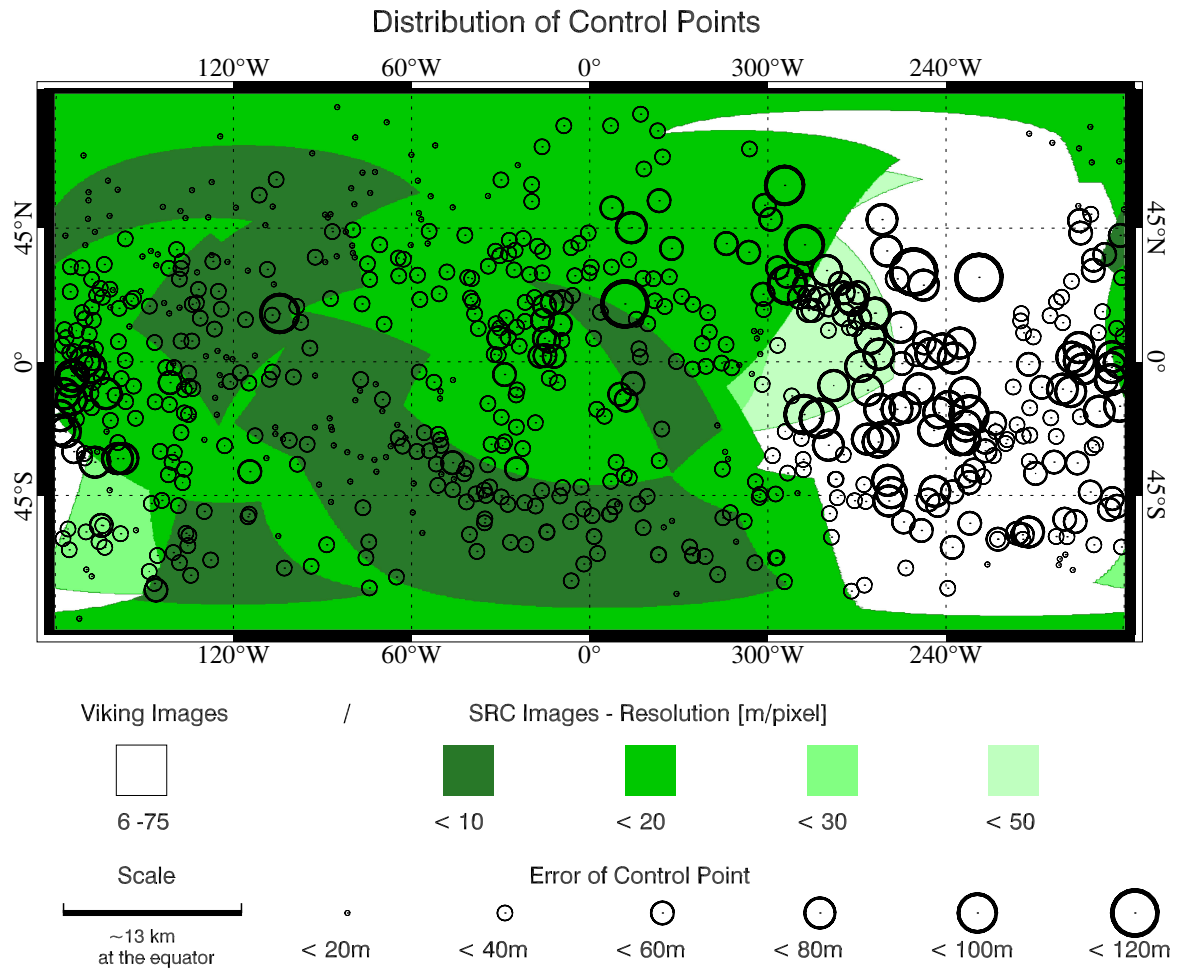


Figure 25: Overview of control point locations and their accuracies. Accuracies degrade visibly in the region covered by Viking Orbiter images.

7 Global Shape Model

Depending on the purpose of a shape model different levels of accuracies and kinds of shape models are necessary. The study of Phobos' grooves in a geological or geomorphological perspective requires a very accurate height information (which can have a high data volume and can thus be of numerical form). To study its physical parameters such as the volume or the moments of inertia tensor a more general model possibly expressed in an analytical function would be required.

Prior to this study different methods were used to model planetary bodies (Table 18). A very simple approximation is the triaxial ellipsoid. This is only used for tasks which require little accuracy. Other models, such as the spherical harmonic function model of degree and order 8 with added detail through local functions describing large craters (Duxbury, 1991), already represent Phobos' figure with much more detail but are still of too low resolution for, e.g., mapping purposes.

Table 18: Methods that were used to model Phobos' shape.

Method	Necessary Observations	Reference
Plaster model	Control point observations	Turner (1978)
Ellipsoidal models	Limb coordinates	Thomas (1989)
Numerical models	Limb measurements	Simonelli et al. (1993)
Spherical Harmonic Expansion model	Ground Control Points, Crater modeling	Duxbury et al. (1991)
Global Digital Terrain Model	Dense point cloud of conjugate points	this study
Spherical Harmonic Expansion model	Dense distribution of Ground Control Points	this study

During this study, two different shape models for Phobos were generated to account for the different needs of cartographic processing and geophysical analysis.

(1) A global digital terrain model (DTM) was determined from HRSC and Viking images. This model was used to ortho-rectify SRC and VO images of Phobos. DTMs contain discrete height information for each element of the model. Height information for small gaps in the model are determined by interpolation between neighboring or surrounding elements. DTMs are relatively large data sets to describe the surface accurately.

(2) The coefficients of a Spherical Harmonic Expansion model (SHE) up to degree and order 17 were computed based on the previously determined control point network (Section 6). The shape of Phobos is described through 324 coefficients of an analytical expression. Radii to all surface points of the shape model can be determined through a function of latitude and longitude pairs. The data set is very small but the low degree and order of the Spherical Harmonic Function does only model larger surface features and represents the general shape of the body. No small local variations of the surface such as the groove system can be reproduced. The SHE were used to compute physical parameters such as the volume, bulk density, the moments of inertia, and rotational state, e.g. the forced libration amplitude. The spherical harmonic expansion model is very useful to determine Phobos' low degree and order gravitational potential for assumed density distributions. It could serve as a basis for future missions to Phobos.

In this section the methods to determine the two shape models are described and results

are compared.

7.1 Global Digital Terrain Model

Planetary stereo images are commonly photogrammetrically processed to derive 3D information of the observed object. Other methods, such as shape from shading, are also used to obtain 3D information from image data, especially when only single images with good light conditions are available (cf. Heipke et al. (2007)).

Phobos was observed several times by different camera systems. Not all available data sets are suitable to determine a global accurate, high resolved DTM. To evaluate the data for suitability, certain requirements were defined:

- The expected accuracy of points determined from images is in the order of the resolution of one image element. Resulting DTM resolutions are often set to double the pixel (accuracy) resolution. Hence, only images with resolutions better than 80 m/pixel were considered.
- To obtain the desired complete coverage a comprehensive number of conjugate points needs to be determined. Hence, it should be possible to apply automated matching techniques to determine large numbers of conjugate points. Image matching algorithms used for planetary image data from Mars are based on the comparison of grey values in pre-rectified images – area based matching – and are thus dependent on the lighting situation (Heipke, 1996). As a consequence, only stereo images obtained under similar phase angles were selected.
- Stereo image sets need to overlap with adjacent stereo images so a block of images can be defined to globally cover Phobos.
- If available, multi-fold stereo information is preferred to twofold stereo information. Fly-by images of the HRSC should be obtained by all panchromatic channels.

The High Resolution Stereo Camera is the first camera system on a planetary mission designed to obtain images suitable for stereo analysis.

HRSC images from twelve fly-bys were found to be suitable for a DTM analysis. During all 12 fly-bys the HRSC obtained images with the nadir, stereo and photometry channels. Thus, quintuple stereo information was available in these HRSC image scenes. HRSC images unfortunately only cover 84% of the surface of Phobos. This, however, does not imply that 84% of the surface is covered in fivefold stereo (cf. Figure 26). The different viewing angles of the sensors result in a slightly different area covered by each sensor during one fly-by. Most of the area covered by the nadir channel is also seen by the other channels providing fivefold stereo information. But the stereo 1 channel for instance is depicting areas of Phobos which cannot be viewed from the stereo 2 channel (see Fig. 27 and 28). Threefold or twofold stereo information is available for these areas. Accuracies in these areas are considerably lower since the angles of convergences are not as favorable as in stereo combination between the two stereo sensors and the nadir sensor.

An area between 180° and 340° West, 60° North and 80° South is partly observed by the HRSC stereo scanner but no conjugate points could be determined. Fortunately, this area was covered by the VO cameras in very high resolution. VO images that were used for the Control Network analysis were now also used to find conjugate points through matching techniques.

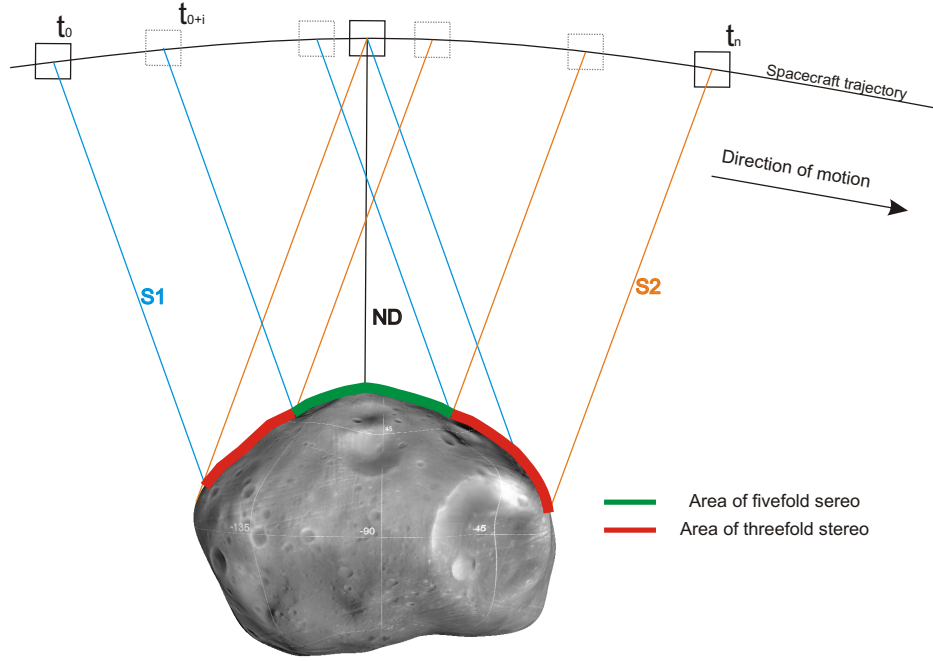


Figure 26: Schematic diagram of stereo covered areas during one fly-by.

7.1.1 Improving the Orientation

Once images were evaluated to be suitable for the DTM determination the orientation information is controlled and improved for each image strip and between the fly-by images. This is necessary since for each channel different orientation information might be registered while all five channels of one image strip must have the same trajectory (Spiegel, 2007). Gwinner et al. (2005) show that improving the orientation prior to the matching process increases the mean accuracy of ray intersections significantly. Furthermore, orientation data for all fly-bys need to be oriented with respect to the same reference frame to avoid artificial height differences in the DTM. A convenient reference frame is the coordinate frame of the control point network. Orientation data of SRC and VO images used to compute the control point coordinates are already registered to this frame. When the navigation data of the HRSC images is now improved with respect to the control point coordinate frame than HRSC, SRC and VO images can be used for the map preparation without any further registration.

Line/sample coordinates of conjugate points were manually selected in all twelve HRSC fly-by image sets. An automation of this process proofed to be unsuccessful due to very small overlapping areas between the image strips, the different resolutions of the images. Common areas between the images are also often near the limb of Phobos and observed under different viewing and light conditions.

The software *HWBUNDLE* (Spiegel, 2007) was used to recompute the exterior orientation for all image sets in one step. This software defines a number of camera view points, called orientation-points, for which the exterior orientation is computed and optimized. The trajectory between the orientation points is interpolated. The interior orientation is assumed to be known to a sufficient accuracy from pre-flight calibrations. The quality of the resulting orientation is judged by several parameters computed during the adjustment.

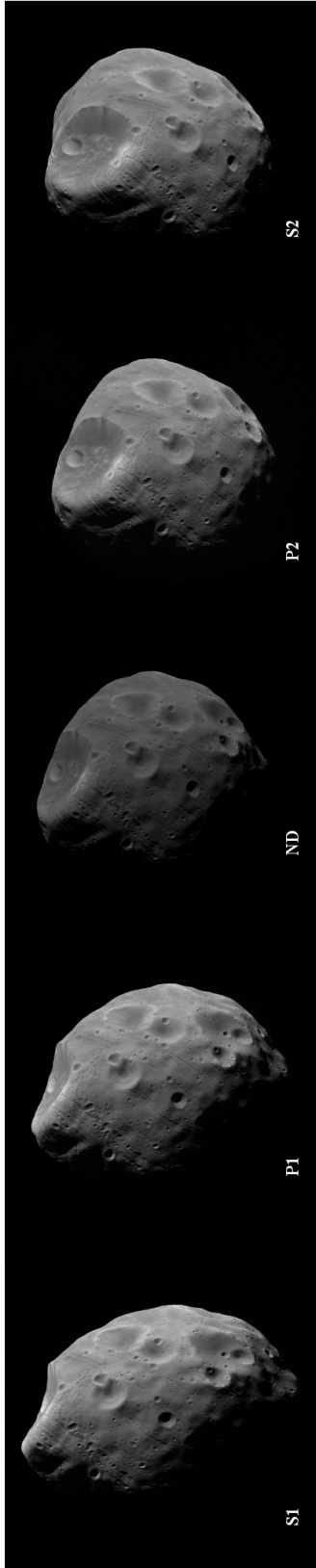


Figure 27: HRSC images of the MEX fly-by during 0756. Fly-by distance was approximately 155 km.

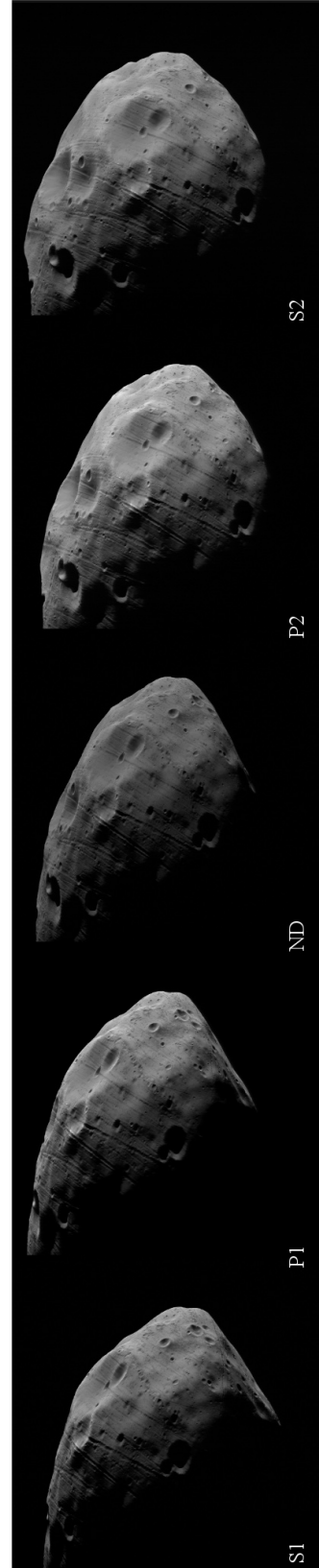


Figure 28: HRSC images of the MEX fly-by during 5851. Fly-by distance was approximately 93 km.

These include:

- Residuals of the object point coordinates,
- Improvements to the image coordinates,
- Number of object points,
- Number of orientation points.

When dealing with Mars images of the HRSC, *HWBUNDLE* uses the MOLA DTM as a reference surface to establish the correct absolute orientation. For Phobos no such reference surface is available making it necessary to introduce coordinates of control points from the control network analysis (Section 6) as pass information. Coordinates of only one control point were held fixed. To control the quality of the orientation with respect to the reference, image coordinates of other ground control points from the network were observed in the HRSC images. By solving for the coordinates of these control points during the adjustment, and comparing the results with the 3D-coordinates determined during the control network analysis, the quality of the absolute orientation was judged.

Best results of the block adjustment were obtained when it was assumed that for all fly-by strips the observed spacecraft position is known with an uncertainty of 500 m. The introduced uncertainty relates to a shift of the predicted trajectory by 500 m in all directions to determine the best fit to the observations. Residuals between control point coordinates computed from observations in HRSC images and coordinates of the same point from the control network did not exceed 20 m. Demanding one orientation point every other second, the adjustment determined 77 orientation points in the twelve fly-by strips.

7.1.2 Matching

Once the navigation data of the HRSC image strips were oriented to the same reference, conjugate points were determined through matching techniques within the single fly-by strips.

To match in HRSC images of Mars, images are pre-rectified to a unified pixel scale onto the MOLA DTM. The use of the a priori topography information of the MOLA DTM reduces the search areas within the matching process (Scholten et al., 2005) and reduces the residuals of correlated points (Gwinner et al., 2005). Typical map projections used are the Sinusoidal map projection for regions from 88° South to 88° North and a Stereographic projection for pole regions. Phobos fly-by images were pre-rectified into the Stereographic or Orthographic projection. Distortions of the image through the map projection were locally minimized by choosing a map projection which models the observation geometry as close as possible (see Table 19 for properties of the map projections). The two different map projection types were used to determine whether one or the other results in more and qualitative better conjugate points.

Since no reliable a priori topographic information is available for Phobos, the images were pre-rectified onto a sphere with the radius of 11.1 km, the mean radius of Phobos (Seidelmann et al., 2007).

Gwinner et al. (2005) introduce several criteria to judge the quality of the resulting object point cloud which are mainly based on geometric and statistical properties of intermediate products. The four criteria are:

- (i) percentage of the accepted points of possible correlated points,

Table 19: Map projections used for pre-rectification during matching procedures

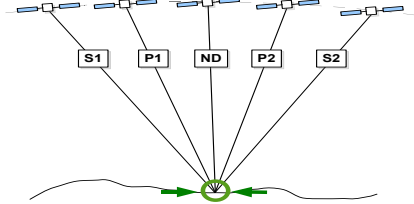
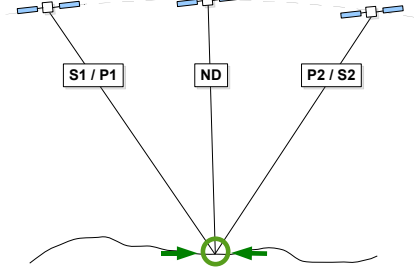
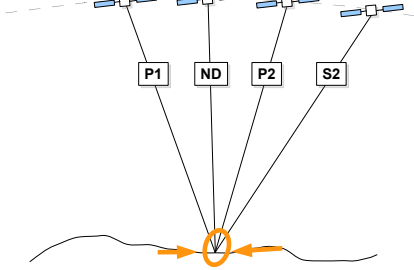
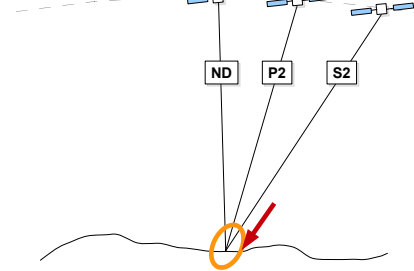
Map Projection	Properties	Area of application
Sinusoidal	<ul style="list-style-type: none"> - pseudo-cylindrical projection - equal area - poles are points - latitudes are parallel lines with equal spacing 	world maps with one central or several central meridians
Stereographic	<ul style="list-style-type: none"> - azimuthal projection - isogonal - perspective projection for spheres - at polar view all meridians are straight lines - at equatorial view the equator is a straight line 	polar and special maps
Orthographic	<ul style="list-style-type: none"> - azimuthal - neither isogonal nor equal area 	pictographic views in conjunction with spheres

- (ii) mean object point accuracy computed through forward ray intersections,
- (iii) object point density, and
- (iv) the lateral variability and accuracy of object points.

Comparing the results of the matching process, based on the two map projections which were used to pre-rectify the images, matching in the Orthographic map projected images delivered more conjugate points of higher quality than in the Stereographic map projection (Fig. 29). A better point density could also be achieved. Hence, images were pre-rectified into an Orthographic map projection during further analysis.

A multi-image matching technique based on the pre-rectified images is then applied to determine conjugate points. The algorithm uses one image as a template comparing all other images to it. The nadir channel image of each fly-by was used as the template for the matching process in the particular image strip. The nadir channel covers the largest common area between all images of that fly-by. Some areas depicted by the forward looking channels can not be observed by the backward looking channels and vice versa (Fig. 26). Only images of one fly-by were matched and no determination of conjugate points between different image strips was attempted by means of matching techniques. The size of the search window in the pattern images can be defined through settings in the matching software. However, due to its pronounced irregular shape relatively large parallaxes were observed between pre-rectified images. Only near the chosen central latitude and central longitude of the projected image parallaxes were small. With increasing distance from the central longitude and latitude parallaxes grow larger exceeding the size of the search window. To exploit the entire information of the image the matching process was started for several central longitude/latitude pairs to minimize the parallaxes in different areas of the image.

Table 20: Possible geometries of point observations. The expected quality of the point accuracy is depicted from top (best quality) to bottom (poor quality).

Quality	Combination	Property	Situation
very good	S1 P1 ND P2 S2	Constraint to all sides with redundancy	
good	S1 ND S2	Constraint to both sides of the nadir channel	
	P1 ND P2		
medium	P1 ND P2 S2	Unevenly constraint - weight through more information on one side	
	S1 P1 ND P2		
poor	P1 S1 ND	Only information from one direction. The largest error is in the direction of the rays due to glancing intersections	
	ND P2 S2		

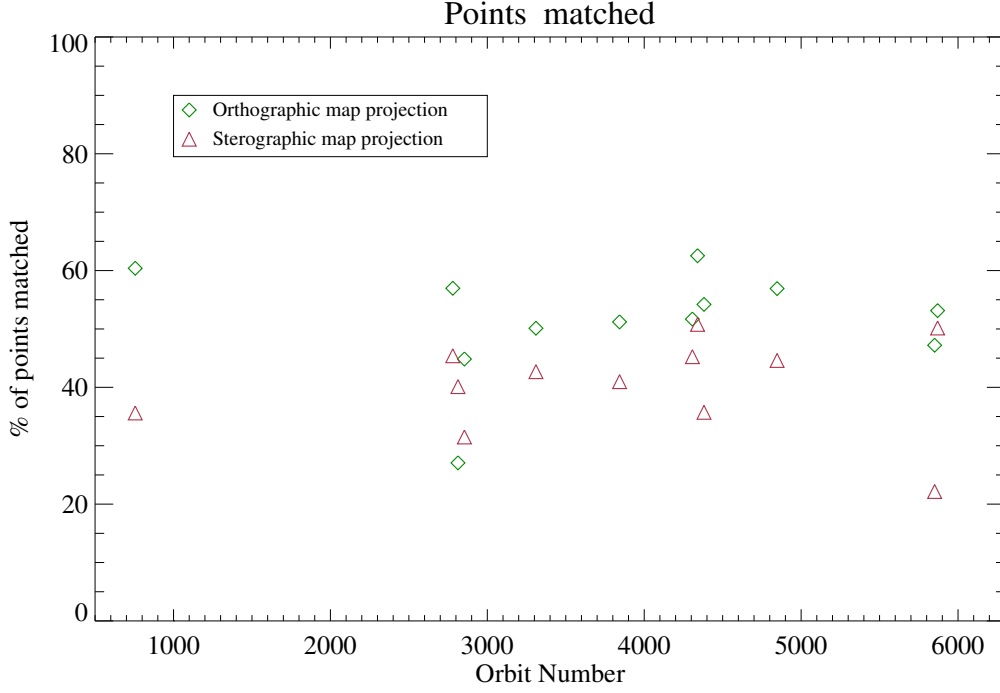


Figure 29: Acceptance in percent out of all possible points which were matched in Stereographic and Orthographic pre-rectified images.

7.1.3 DTM Generation

The matching process resulted in a number of point clouds for each fly-by during which Phobos was observed.

To be able to mosaic a DTM with the highest possible accuracy, the point clouds were subdivided into different groups of points depending on two different criteria. The first was the observation geometry reflected in the number and combination of channels in which the points were observed (see Table 20 for the classification scheme depending on the geometry). All points were separated into groups depending on the underlying observation geometry. In a second step, points of one observation geometry were subdivided into groups depending on the computed accuracy of the ray intersections.

In the next step, one DTM for all points of the same accuracy level and of the different observation geometries is computed. Single terrain models of all possible observation geometries are mosaicked to obtain only one DTM. During the mosaicking process one layer is copied onto the previous one, overwriting values in equal areas. Gaps in the DTM, which is copied onto the previous DTM layer, may thus be filled with areas of the underlying DTMs. By layering the terrain models from poorest - bottom - to best observation geometry - top - it was assured that the DTM with the estimated best quality is fully visible and only gaps are filled with DTM values of poorer quality (Fig. 30).

In the same fashion, the terrain models of each accuracy level were combined to one single DTM. Finally the DTM was visually controlled for eventual peaks. The remaining gross, obvious errors in the DTM were edited manually. The final DTM has a pixel resolution of 100 m. The lateral accuracy is assumed to be the same as the quality of the orientation with respect to the control point network. Hence, the DTM has a horizontal uncertainty of only ± 20 m which corresponds to only a fifth of a pixel of the final DTM.

Uncertainties of the height information of the DTM vary depending on the region. Since

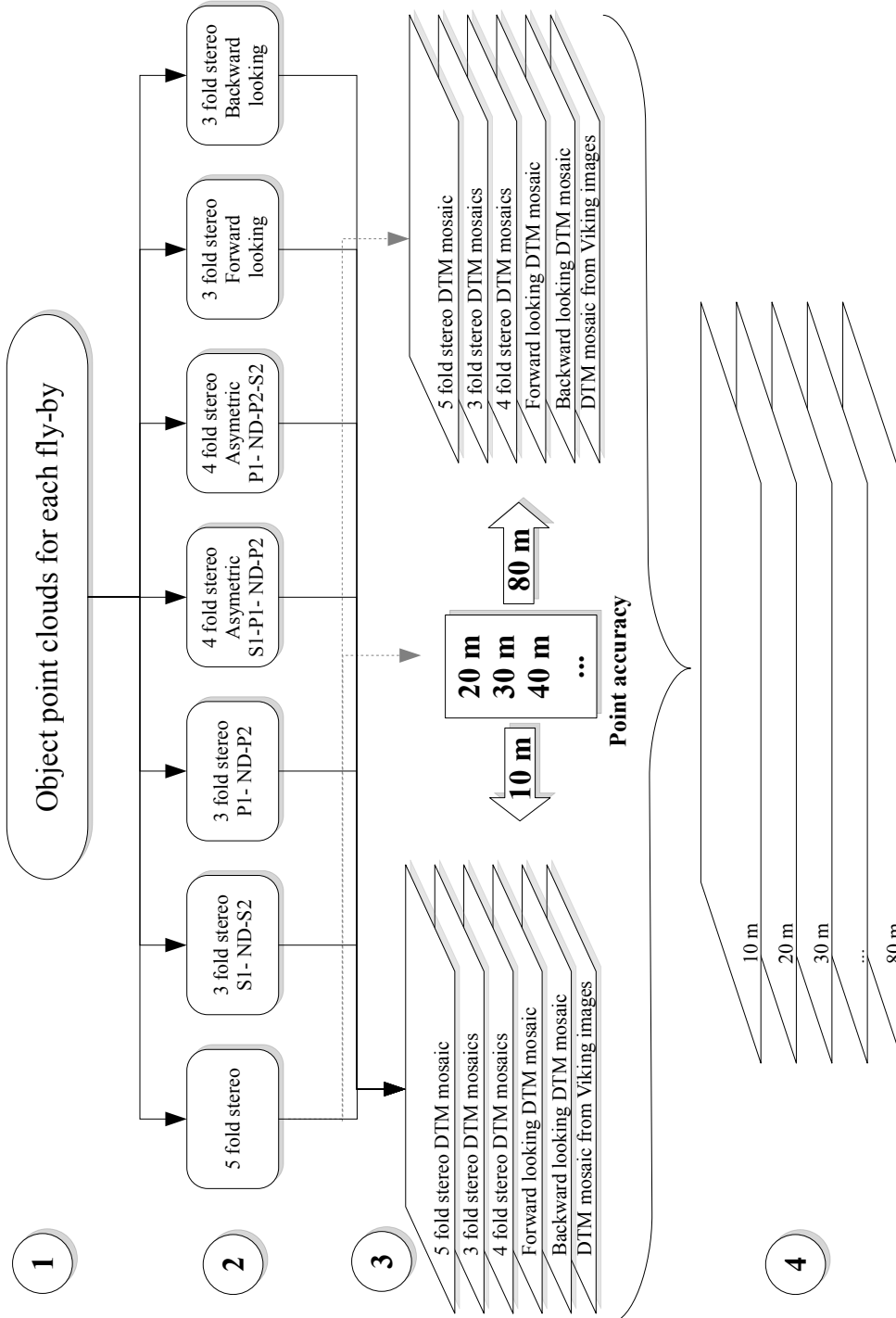


Figure 30: Scheme of the mosaicking process of the global DTM for Phobos

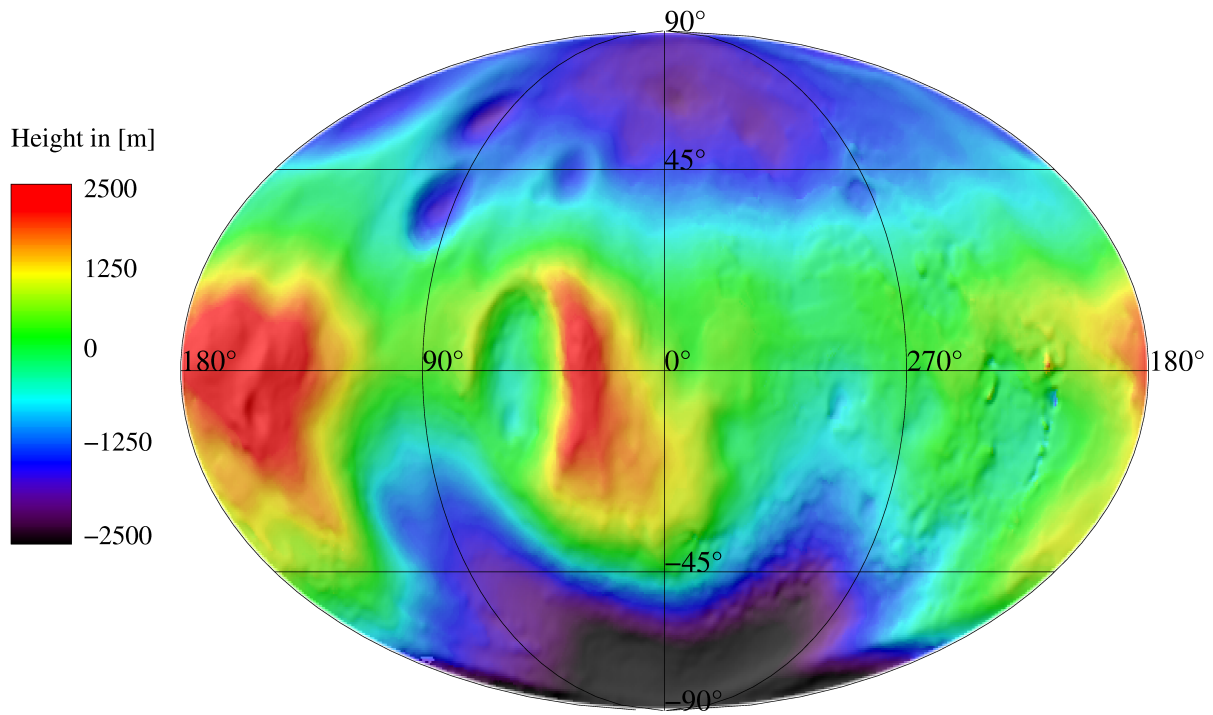


Figure 31: Global DTM with a lateral resolution of 100 m. Heights are given with respect to a sphere with the mean radius of Phobos of 11.1 km.

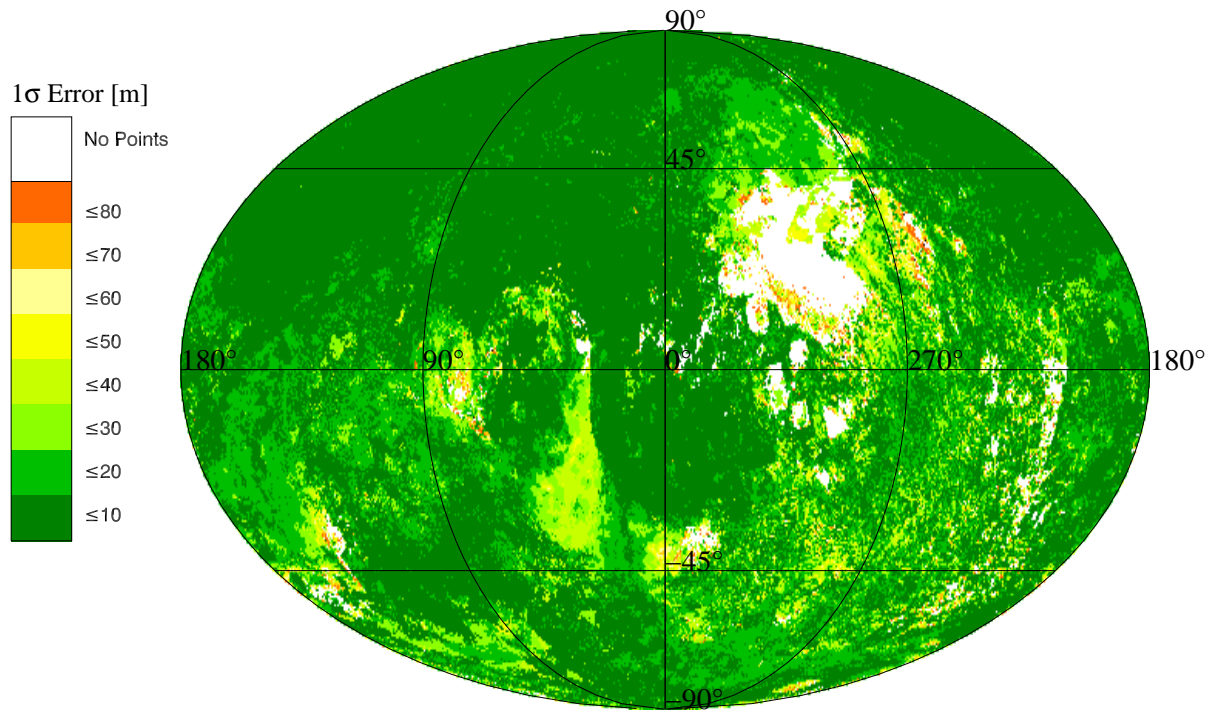


Figure 32: Accuracy map of the global DTM.

various pixel resolution and even different image data sets were used to assemble the terrain model, each pixel might have a different quality (Fig. 32). A relatively small area on the trailing side of Phobos is not sufficiently covered by any data set and the matching algorithm did not return any results. This area was filled by interpolating over the surrounding area.

The DTM was primarily used to compile a global map of Phobos. SRC and Viking images of Phobos were ortho-rectified and map projected. The process of the ortho-map compilation proved to be rather complex (Semm, 2008).

A detailed DTM is also required to analyze secondary echos received by MARSIS (Mars Advanced Radar for Subsurface and Ionospheric Sounding) (Cicchetti et al., 2008). The MARSIS experiment is an orbital sounding radar optimized for deep penetration. During the close approach on 28. July 2008, MARSIS successfully detected primary echos from the surface of Phobos. However, to distinguish subsurface features from surface features in the secondary echoes detailed information about the surface geometry is necessary.

7.1.4 Controlled Ortho-Image Mosaic and Global Map

The DTM was the fundament for a global Phobos atlas. Images of the SRC and VOs were ortho-rectified and mosaicked (Semm, 2008). To ortho rectify images, detailed information of the underlying surface is necessary which was provided by the generated DTM. A sphere with 11.1 km radius was chosen as reference surface for heights.

An atlas on a scale of 1:50,000 was generated. It was divided into three map sheets according to the quadrangle scheme by Greeley and Batson (1990). To provide the maps with little distortion, ortho rectified images of the central latitudes between 57° and -57° latitude are divided into two Mercator maps, one displaying the leading side of Phobos, 0° to 180° West, and the other the trailing side, 180° to 360° West, each occupying one map sheet. Pole areas are mapped in a Stereographic map projection and are both on the third sheet (see Appendix D for print outs).

All maps include contour lines and nomenclatures to label the most prominent surface features. The location and resolution of images used for the map projection are depicted in smaller index and resolution maps (Wählich et al., 2009).

7.2 Spherical Harmonic Function Model

The shape of Phobos was also modeled by spherical harmonic functions. Only “star-like” objects can be described by spherical harmonic functions. These are objects fully containing all possible line segments, which originate in the center of figure and are pointing at a surface point, within the body. This means that no overhangs or bubble like features can be taken into account since line segments would then intersect the surface several times (Garboczi, 2002). For Phobos no such features are observed and thus the model can be applied.

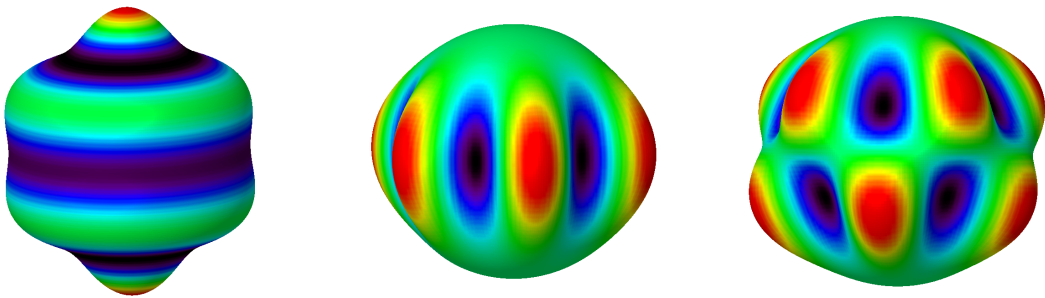
The surface harmonics, which are of interest in this case, are expressed by linear combination of real terms of the spherical harmonic. MacRobert (1967) shows that for positive integer numbers n and m ,

$$u(\phi, \lambda) = \sum_{n=0}^{\infty} \sum_{m=0}^n [A_{nm} \cos m\lambda + B_{nm} \sin m\lambda] P_{nm}(\sin \phi) \quad (14)$$

is the surface spherical harmonic function of degree n and order m . Here $P_{nm}(\sin \phi)$ are the associated Legendre polynomials and λ is the longitude with $0 \leq \lambda \leq 2\pi$. The latitude ϕ ranges between $-\frac{\pi}{2} \leq \phi \leq \frac{\pi}{2}$ and $u(\phi, \lambda)$ describes the radius to a surface point with the coordinates λ, ϕ .

Equation (14) includes descriptions for zonal (Fig. 33(a)), sectorial (Fig. 33(b)) and tesseral (Fig. 33(c)) harmonics, depending on the degree n and order m combination considered.

For all cases with $m = 0$ Eq. (14) only depends on the function of $P_{nm}(\sin \phi)$ since $\cos m\lambda$ equals 1 for all λ and the $\sin m\lambda$ terms vanish. Hence, the function is independent of the longitude λ and the a description of the body by positive and negative zones, relative to the mean radius A_{00} of the body, occurs parallel to the equator. When n is an even number, an even number of zones (zonal harmonics) between the poles describe the body. For odd numbers of n the body is divided asymmetrically into zones.



(a) Zonal harmonic $n=6$ $m=0$ (b) Sectorial harmonic $n=m=6$ (c) Tesseral Harmonic $n=6$ $m=5$

Figure 33: Plot of the spherical harmonic functions which are divided into three groups: Zonal, Sectorial and Tesseral harmonics. Positive areas, with respect to the reference radius defined by the coefficient A_{00} , are colored in red and negative areas in blue to black.

When $n = m$ the associated Legendre polynomials $P_{nn}(\sin(\phi))$ have only zero points at the poles and the sum of cosine and sine terms is never becoming zero. Hence, the body is described by sectors parallel to longitudes (sectorial harmonics).

Finally, when $m \neq 0$ and $n \neq m$ the surface spherical harmonic is describing the body by different zones due to the $(n - m)$ roots in $P_{nm}(\sin \phi)$, but also by $2m$ sections through the multiplication of $\cos \lambda$ and $\sin \lambda$. This results in a tesseral-like pattern accounting for the tesseral harmonics.

By determining the coefficients A_{nm}, B_{nm} of Eq. (14) an arbitrarily shaped body can be described.

7.2.1 Evaluation of the Data Set

The expansion model used in the literature is based on 280 control points and is developed up to degree and order 8 (Duxbury, 1991). Since the shape model insufficiently described the crater blotched body of Phobos, additional local functions for large craters were introduced. Instead the ratio was determined from known depth-to-diameter relationships of craters and the general appearance of each crater in planetary images. During this study

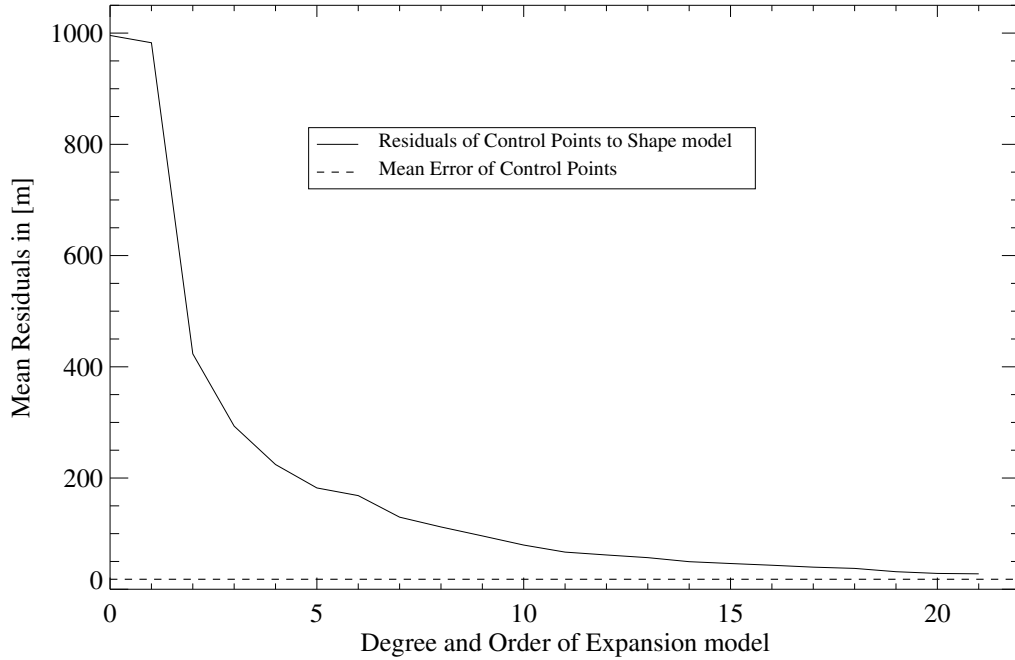


Figure 34: Mean Residuals of Control Points to the spherical harmonic function model. The dashed line marks the mean error of the control points.

a spherical harmonic function model to degree and order 17 was determined, based on HRSC, SRC and VO images. No extra functions were introduced to model specific surface features.

The 3D-coordinates of the 665 control points of the control point network analysis were used as initial input data set. The quality of the expansion model was estimated by computing the remaining differences between observed radii of the control points and modeled radii in the respective directions.

Residuals naturally decrease with increasing degree and order determination (Figure 34). However, visual control of the resulting shape model indicates that the modeled shape departs from the observations in images when developing the expansion model to a degree and order higher than 15 (cf. Figures 35(a) and 35(b)). It is apparent that the degradation

is regionally confined to an area close to the North Pole but other areas are still well described with expansion models of even higher degree and order.

The degradation is a result of the little constraint in this area (see also Figure 25). Only a few control points were observed on this side of the North Pole. Before 2008, it was neither observed under good light conditions nor with high resolution by any camera system.

During 2008, the orbit of Mars Express was especially adjusted to allow for Phobos observations from close range during a number of fly-by maneuvers. In orbit 5851 MEX passed Phobos with a distance of only 93 km to its surface. The HRSC obtained a full set of high resolution stereo images of the North Pole area with a pixel resolution of 4 m and 8 m with the nd,s1,s2 and the p1,p2 channels, respectively (cf. Table 4). Due to the relative velocity between Phobos and MEX of 3 km/s the recorded SRC images suffer from severe smear effects. Furthermore, the area covered by the SRC images is very small delivering no additional information for this analysis.

In contrast to the SRC data, the HRSC images could well be used to obtain more control points in the weakly constrained area. To be able to use the HRSC observation of this fly-by, the orientation information of the HRSC was improved and tied to the control point network by introducing one control point as tie point into the block adjustment. The quality of the orientation with respect to the control point network was tested in the same way as described in Section 7.1.1. Residuals between the 3D-coordinates from the different adjustments were below the average uncertainty of the control points of the network. Hence, 90 object point coordinates computed within the bundle block adjustment of the HRSC image strip from orbit 5851 could be introduced to the analysis of the spherical harmonic function without contradictions.

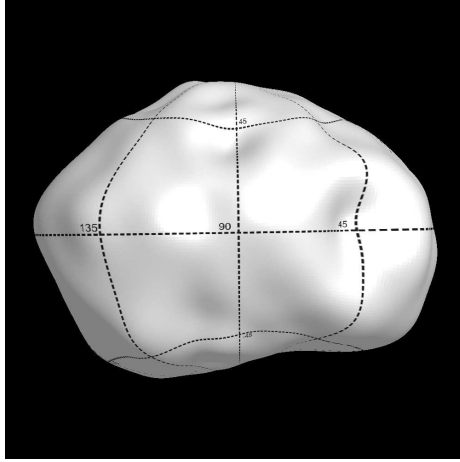
Using the new data the expansion model could be developed up to degree and order 17. Tests were made to develop the expansion model to higher degree and order. However, reasonable determination of the coefficient was only possible to degree and order 17 (cf. Fig 35(c) to 35(e)).

7.2.2 Computation

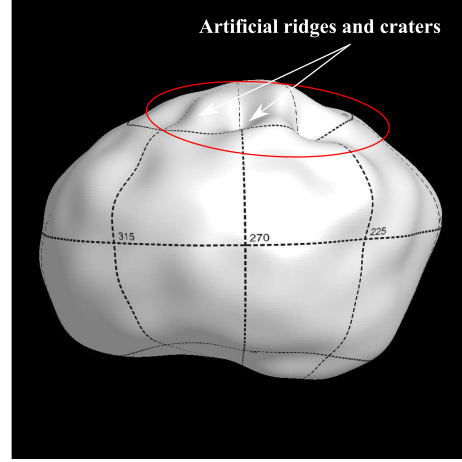
The equation system including the coefficients of the surface spherical harmonic function model was solved by means of a least-squares adjustment. Therefore the 3D-coordinates of the control points were converted into spherical coordinates. The resulting latitudes and longitudes of these points were introduced as fixed known values into the equation system. The radii to the points are observed parameters in the adjustment process. Solving for the unknown coefficients, A_{nm} , B_{nm} , of the equation system (Eq. (14)). Since the control points are afflicted with errors the radii were introduced as weighted observations according to their errors, which were determined during the control network analysis.

755 observations were introduced into the adjustment problem. For the expansion model with degree and order 17 only 324 coefficients need to be determined. This states a redundant problem and can be solved through least-squares adjustment techniques. Approximately 2.5 radii observations are available to determine one coefficient. The unknown surface expansion coefficients are in a linear relation to the observed radii. Starting values of the coefficients could be set to zero.

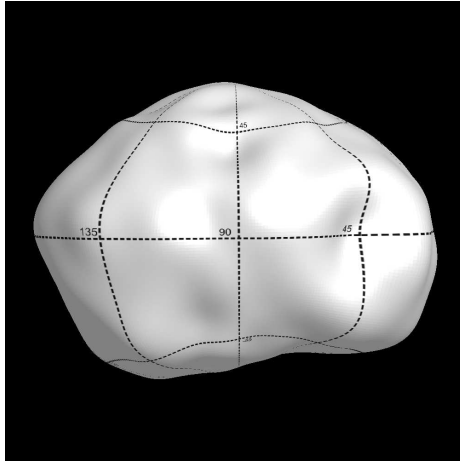
The 324 coefficients of the degree and order 17 spherical harmonic function were computed with remaining mean residuals to the object point coordinates of ± 40 m. The coefficients and the corresponding one sigma errors can be found in the Appendix C.



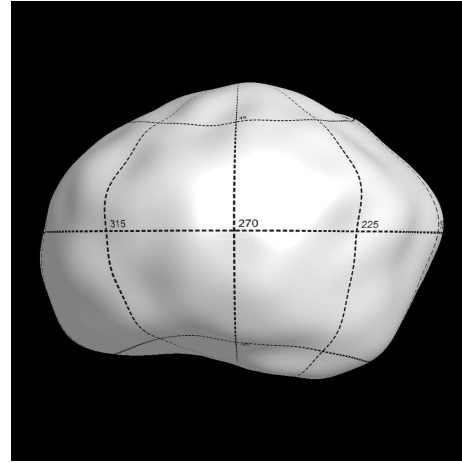
(a) Leading side, 665 points, Degree and order 15 model.



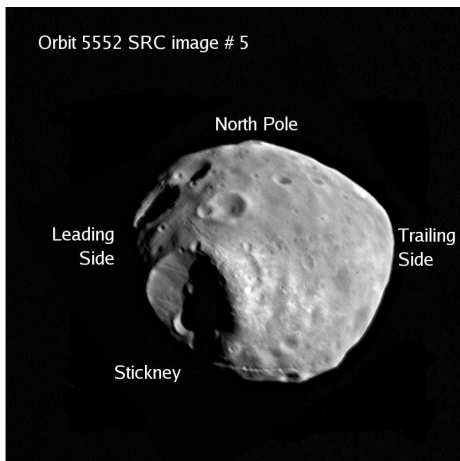
(b) Trailing side, 665 points, Degree and order 15 model.



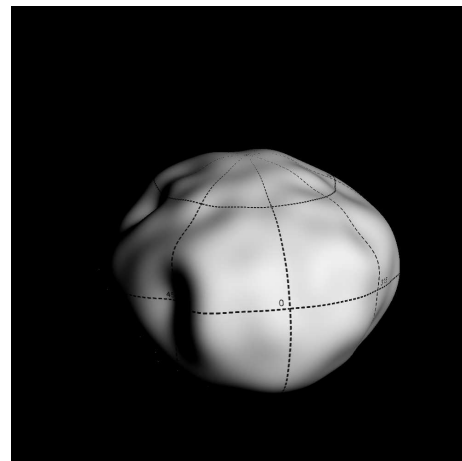
(c) Leading side, incl. HRSC points, Degree and order 17 model.



(d) Trailing side, incl. HRSC points, Degree and order 17 model.



(e) SRC observation of MEX Orbit 5552.



(f) Modeled view of Orbit 5552.

Figure 35: (a) and (b) show shape models based on 665 ground control points developed to degree and order 15. 665 plus 90 additional points from HRSC observation of orbit 5851 were used to compute the coefficients of the improved expansion model of degree and order 17 ((c) and (d)). An example of one SRC observation is given in Figure (e) which is compared with the modeled view in (f).

7.2.3 Interpretation of the Coefficients

In a first approximation it was assumed that the coordinates of the control points were observed in a coordinate frame with the origin at the center of figure of Phobos. However, the degree and order one coefficients of the spherical harmonic function are non-zero coefficients, indicating a difference in the location of the center of figure and the origin of the coordinate frame.

The translation between the origin of the coordinate frame and the center of figure is expressed through the degree and order one coefficients. This becomes apparent when Equation (14) is explicitly written out. The associated Legendre Polynomials for $m, n = 0, 1$ are,

$$\begin{aligned} P_{00} &= 1 \\ P_{10} &= \sin \phi \\ P_{11} &= \sqrt{(1 - \sin^2 \phi)} = \cos \phi . \end{aligned}$$

Hence, $u(\phi, \lambda)$ becomes

$$u(\phi, \lambda) = A_{00} + A_{10} \sin \phi + A_{11} \cos \lambda \cos \phi + B_{11} \sin \lambda \cos \phi . \quad (15)$$

The three terms associated to the degree and order one coefficients A_{nm}, B_{nm} for $n = 1$ and $m = 0, 1$ can be written as

$$\begin{pmatrix} A_{11} \\ B_{11} \\ A_{10} \end{pmatrix} \cdot \begin{pmatrix} \cos \lambda \cos \phi \\ \sin \lambda \cos \phi \\ \sin \phi \end{pmatrix} = \mathbf{F} \cdot \vec{e}_r = F_r , \quad (16)$$

which is a representation of the elements of a Cartesian coordinate vector \mathbf{F} as corresponding spherical coordinate F_r . \vec{e}_r is the unit vector in the direction of the radius r as a result of

$$\begin{pmatrix} X \\ Y \\ Z \end{pmatrix} = \begin{pmatrix} r \cos \lambda \cos \phi \\ r \sin \lambda \cos \phi \\ r \sin \phi \end{pmatrix} . \quad (17)$$

The last product in Eq. (16) can also be written as

$$\mathbf{F} \cdot \vec{e}_r = \begin{pmatrix} F_x \\ F_y \\ F_z \end{pmatrix} \cdot \begin{pmatrix} \cos \lambda \cos \phi \\ \sin \lambda \cos \phi \\ \sin \phi \end{pmatrix} \quad (18)$$

with

$$F_x = \mathbf{F} \cdot \vec{e}_x \quad F_y = \mathbf{F} \cdot \vec{e}_y \quad F_z = \mathbf{F} \cdot \vec{e}_z ,$$

where F_x, F_y and F_z are the elements of the Cartesian vector. Hence, A_{11}, B_{11} and A_{10} can also be interpreted as a translation vector along the Cartesian coordinate axes. It is applied to all points of the figure and is thus a translation of the entire figure also interpreted as the offset between the origin of the applied coordinate frame to the center of figure.

The finding of the final translation vector is an iterative process. Coordinates of the control points are shifted three to four times before the origin of the coordinate set is

within 0.5 m to the center of figure. The difference between the origin of the coordinate frame and the center of the figure model was determined to be

$$X = -375.9\,m, \, Y = -341.8\,m, \, Z = 206.3\,m \, , \tag{19}$$

when using control points computed with the latest orbit prediction model, *MAR080*.

8 Physical Parameters of Phobos

Physical parameters of a planetary body describe the body in a complementary way to the visible image. The volume for instance allows conclusion on the bulk density of a body once the mass is estimated. The density in turn, together with a mass distribution model, can be used to determine the moments of inertia and thus the principle axes of the body. For Phobos the moment of inertia tensor provides even more information. It is the basis to model the forced libration amplitude of Phobos. In this section the determination of the volume, bulk density, moments of inertia, and a model for the forced libration amplitude is described. Conclusions are drawn at the end of this section.

8.1 Volume

To compute the volume of this irregular body the spherical harmonic expansion model described in Section 7.2 to degree and order 17 was used. The volume of a sphere as a function of spherical coordinates,

$$V = \int_0^{2\pi} \int_0^\pi \int_0^r r^2 \sin(\phi) dr d\phi d\lambda , \quad (20)$$

can analytically be solved for r ,

$$V = \frac{1}{3} \int_0^{2\pi} \int_0^\pi r^3(\phi, \lambda) \sin(\phi) d\phi d\lambda . \quad (21)$$

To describe the irregular body of Phobos, r is substituted by Equation (14) in Section 7.2, introducing a variable radius depending on the longitude λ and the latitude ϕ .

When developed to degree and order 17 the analytic expression of Equation (14) is rather complex due to its many terms. It proved to be very demanding in terms of computational time and computational power to solve the integral by analytical means to obtain the volume. Hence, a numerical solution was derived. A transition from spherical coordinates to Cartesian coordinates was made and discrete volume cubes were used to determine the total volume. The numerical solution of the integral is an approximation. Its accuracy was tested prior to the computation of the volume and the moment of inertia tensor for Phobos. The volume of a triaxial ellipsoid was computed through the integration of the volume cubes and then compared to the value determined with the analytical expression

$$V = \frac{4}{3} \pi abc , \quad (22)$$

where a, b and c are the radii of the triaxial ellipsoid. The integration was started at the origin of the coordinate frame and interrupted once the center of the volume cube is outside of the body. The value of the radius in the direction of the volume cube center was computed applying Equation (14) and the previously determined coefficients.

Moments of inertia were computed in the same way as the volume, assuming a homogeneous mass distribution model. Evaluating the accuracy of the summation, the method was tested for both, the volume and the moment of inertia values (Figure 36).

Volume cubes were varied starting with a cube size of 500 m per side, subsequently decreasing the cube size. Since the computation time is moderate and the approximation is

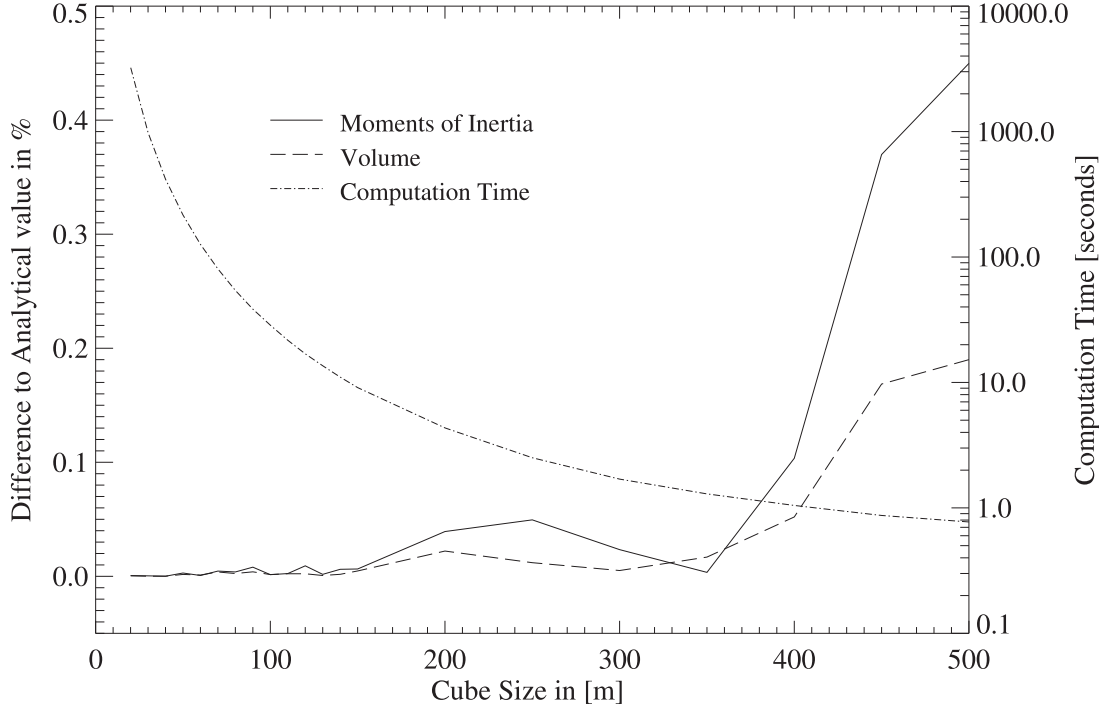


Figure 36: Difference of analytic computed values and values determined by numeric integration.

almost perfect, it was decided to use cubes of a size of $20 \times 20 \times 20$ m to compute the volume and the moment of inertia tensor.

A volume of $5689.8 \pm 60 \text{ km}^3$ was determined for Phobos based on the spherical harmonic function model. While this agrees well to previous mass estimates of 5680 km^3 (Duxbury, 1991) and 5620 km^3 (Thomas, 1979), the uncertainty estimate of $\pm 60 \text{ km}^3$ has significantly improved compared to previous reports ($\pm 250 \text{ km}^3$).

8.2 Bulk Density

Early studies of Phobos' composition, based on observations of the Viking Orbiters, suggested a bulk density of $2.2 \pm 0.4 \text{ g/cm}^3$ (Duxbury and Callahan, 1982). Burns (1992) reports that results of the *Phobos 2* mission narrowed the bulk density estimate to $1.9 \pm 0.1 \text{ g/cm}^3$ just within the error band of the $2.2 \pm 0.3 \text{ g/cm}^3$ which were also derived from Viking observations (Duxbury and Callahan, 1989b).

A bulk density estimate depends on the volume as well as on the mass estimates. While both values were previously quite uncertain, previous volume estimates were now confirmed and the derived volume is expected to deviate not more than 1% from the derived value. Recent mass estimates derived from fitting close fly-by trajectories to spacecraft trajectory predictions (Andert et al., 2008), from modeling of Phobos' orbit (Jacobson, 2008), and from fits of long term spacecraft trajectories to gravity field models (Konopliv et al., 2006) vary also by less than 1% (cf. Table 21).

The estimated mean densities vary by not more than 2% (cf. Table 21) and show that Phobos has a very low mean density of $1.875 \pm 0.008 \text{ g/cm}^3$.

The derived density is much lower than e.g. rock density of 3.5 g/cm^3 . Hence, Phobos must have either a high porosity or is consisting of low density material which could be water-ice or CI chondrites. Britt and Consolmagno (1997) measured the densities

Table 21: Computed bulk density depending on current mass estimates. The observed volume of 5689.8 km^3 was used. With G being the gravitational constant.

Reference	GM (km^3/sec^2)	Bulk Density (g/cm^3)
Konopliv et al. (2006)	$0.7158 \pm 0.009 \times 10^{-3}$	1.885 ± 0.024
Jacobson (2008)	$0.7112 \pm 0.001 \times 10^{-3}$	1.873 ± 0.003
Andert et al. (2008)	$0.7090 \pm 0.002 \times 10^{-3}$	1.867 ± 0.005

on sample meteorites and found only the Orgueil meteorite, a CI chondrite, to have a low density of 1.6 g/cm³. CI chondrites – a class of carbonaceous chondrite – are known to have altered extensively by water and thus lacking chondrules. They contain a high abundance of organic carbon (Ehrenfreund et al., 2001). Orgueil has a grain density of 2.4 g/cm³. The porosity was determined to be as high as 35 %. An explanation for the low bulk density could be water inclusions within Phobos or micro porosity emerging from impacts – which Phobos has clearly experienced.

8.3 Moments of Inertia

8.3.1 Theory

The kinetic energy E of a discrete mass element with the mass M within a rigid body is defined to be

$$E = \frac{1}{2} M v^2, \quad (23)$$

where v describes the velocity of the mass element with respect to an inertial reference frame. Considering a translation \vec{V} of the body, with respect to the fixed point, and a rotation about one of its axes, the velocity v of the mass point is divided into the translation of the body and the rotation of the mass point within the body,

$$\vec{v} = \vec{V} + \vec{\omega} \times \vec{x}. \quad (24)$$

Here $\vec{\omega}$ is the angular velocity of the mass element at the location \vec{x} , given with respect to the body-fixed frame. If now all mass elements of the rigid body are considered, the total mass can be described by

$$M_B = \int d^3x \rho(\vec{x}), \quad (25)$$

where $\rho(\vec{x})$ is the mass distribution. Substituting M and v in equation (23) by equations (25) and (24), respectively, the kinetic energy of the body is,

$$\begin{aligned} E &= \frac{1}{2} \int d^3x \rho(\vec{x}) (\vec{V} + \vec{\omega} \times \vec{x})^2 \\ &= \frac{1}{2} \vec{V}^2 \int d^3x \rho(\vec{x}) + (\vec{V} \times \vec{\omega}) \cdot \int d^3x \rho(\vec{x}) \vec{x} \\ &\quad + \frac{1}{2} \int d^3x \rho(\vec{x}) \omega^l [\vec{x}^2 \delta_{lm} - x_l x_m] \omega^m, \end{aligned} \quad (26)$$

where δ_{lm} is the Kronecker-Delta which is defined by

$$\delta_{lm} = \begin{cases} 0, & \text{if } l \neq m \\ 1, & \text{if } l = m \end{cases} ,$$

and $l, m = 1, 2, 3$ address the single elements of the vectors. The integral of the first term in equation (26) equals the total mass M_B of the body (Eq. (25)). The integral of the second term vanishes since it equals the condition to define the barycenter,

$$\int d^3x \vec{x} \rho(\vec{x}) = 0 .$$

The kinetic energy of the rigid body,

$$E = \frac{1}{2} M_B \vec{V}^2 + \frac{1}{2} \vec{\omega} \mathbf{J} \vec{\omega} \quad (27)$$

with

$$\mathbf{J} = \int d^3x \rho(\vec{x}) (\vec{x}^2 \delta_{lm} - x_l x_m) , \quad (28)$$

is thus separated into translational energy and rotational energy. \mathbf{J} is known as the moment of inertia tensor and expresses, together with the angular velocity, the rotational energy of a body (Scheck, 2007), which is of interest in the context of this study.

Values of the elements of the inertia tensor depend on the origin of the body-fixed frame, its orientation with respect to the principle axes of inertia, and the mass distribution $\rho(\vec{x})$. The moment of inertia tensor is a symmetric, orthogonal tensor which can be transformed into a diagonal matrix $\hat{\mathbf{J}}$. The diagonalization orientates the tensor with respect to a different body-fixed frame – which, in this case, is the frame defined by the principle axes of inertia. The rotation matrix R consists of directions $\hat{\omega}^{(i)}$, $i = 1, 2, 3$, which satisfy the conditions

$$\mathbf{J} \hat{\omega}^{(i)} = I_i \hat{\omega}^{(i)}, \quad (29)$$

where I_i are the diagonal elements of $\hat{\mathbf{J}}$. This is a typical eigenvalue problem which can also be expressed as

$$(\mathbf{J} - I_i \bar{E}) R = 0, \quad (30)$$

where \bar{E} is the identity matrix. A solution is only given when the determinant

$$\det(\mathbf{J} - I_i) = 0, \quad (31)$$

becomes zero. Equation (31) is also called the characteristic equation of the matrix. Goldstein (1980) shows that the characteristic equation for the inertia tensor has three real, positive solutions – the eigenvalues I_i – and a solution can be found for any point in a rigid body. The eigenvalues are known as the principle moments of inertia which do have one corresponding axis each. These axes are mutual orthogonal to each other and are called the principle axes.

8.3.2 Computation of the Tensor

To determine the inertia tensor, Phobos was, similar to the volume determination, divided into n discrete mass elements. The total mass can then be written as the sum over all

mass elements m_i ,

$$M = \sum_{i=1}^n m_i . \quad (32)$$

When applying volume elements of $20 \times 20 \times 20$ m n equals approximately 711,125,000. When substituting the term for the total mass in equation (28) by equation (32) and explicitly writing out the elements of \mathbf{J} , the equation

$$J_{lm} = \begin{pmatrix} \sum_i m_i (x_{i2}^2 + x_{i3}^2) & -\sum_i m_i x_{i1} x_{i2} & -\sum_i m_i x_{i1} x_{i3} \\ -\sum_i m_i x_{i2} x_{i1} & \sum_i m_i (x_{i1}^2 + x_{i2}^2) & -\sum_i m_i x_{i2} x_{i3} \\ -\sum_i m_i x_{i3} x_{i1} & -\sum_i m_i x_{i3} x_{i2} & \sum_i m_i (x_{i1}^2 + x_{i2}^2) \end{pmatrix} \quad (33)$$

is derived. Equation (33) was used to determine the moment of inertia tensor during this study. Since the origin of the coordinate frame was already brought into agreement with the COF (cf. section 7.2.3), it was expected that the resulting inertia tensor is already a diagonal matrix. However, remaining off-diagonal elements indicated that the coordinate axes of the control point network frame are still rotated against the principle axes of inertia.

The rotation matrix is defined by the eigenvectors $\hat{\omega}^{(i)}$. Small rotations of the coordinate frame of the control points and the principle axis frame were necessary to diagonalize the inertia tensor. The angular difference between the two frames was observed to be,

$$\alpha = -0.5970^\circ, \quad \beta = -0.7283^\circ, \quad \gamma = 0.6904^\circ$$

where α, β and γ are the rotation angles about the X -, Y -, and Z -axis of the control network frame, respectively. These need to be applied as follows,

$$\vec{x} = R_Z(\gamma) R_Y(\beta) R_X(\alpha) \vec{x}'.$$

Where $R_{X/Y/Z}$ are the rotation matrices about the corresponding axis, \vec{x}' is the observed coordinate vector of the control point with respect to the COF and \vec{x} represents the vector to the control point with respect to the principle axes. The moments of inertia were determined to be

$$A = 0.3615, \quad B = 0.4265, \quad C = 0.5024 \quad (34)$$

when normalized by $1/Mr_0^2$, with M being the observed mass of Phobos. r_0 equals the spherical harmonic coefficient of degree and order 0, A_{00} , and is the mean radius of Phobos. Duxbury (1989) computed the moments of inertia from a spherical expansion model of degree and order 6 determining the values of $A=0.3362$, $B=0.3871$ and $C=0.4773$. While the differences between previous values and values computed during this study appear to be small, the ratio of the principle moments has changed. This affects the model of the forced libration.

8.4 Forced Libration Amplitude

As described in section 4.2.1, the forced libration is a superimposed oscillation on the rotation of Phobos. Due to its elongated shape, Phobos is interacting with the Martian gravity field and thus forced to oscillate periodically. The dependence on the elongated shape can be deflected from

$$\theta_A = \frac{2e}{1 - \frac{1}{3\hat{\gamma}}} \quad \text{with} \quad \hat{\gamma} = \frac{B - A}{C}, \quad (35)$$

where θ_A is the amplitude of the forced libration in radians, $A \leq B \leq C$ are the principle moments of inertia, along the principle axes, and e is the orbital eccentricity (Chao and Rubincam, 1989). It is obvious that $\hat{\gamma}$ would vanish if the A and B moments of inertia were equal, which would occur when the equator describes a circle of a symmetrically formed body under the assumption of a homogeneous mass distribution.

Varying velocities of Phobos in its slightly elliptic orbit and the synchronous rotation about Mars result in the geometric libration. The amplitude of the geometric libration amounts to two times the eccentricity $e = 0.0151$ (Burns, 1992). As well as the other orientation parameters, the geometric libration is implicitly applied when transformations into or from the Phobos body-fixed frame are computed.

Within the scope of this study, the forced libration amplitude was observed through the control points of the control network and compared to models assuming different mass distributions. By calculating the moment of inertia tensor the forced libration amplitude is obtained from Eq. (35).

8.4.1 Observation

To compute the coordinates of the control points during the control network analysis, the position and orientation parameters of the camera view points were transformed into the Phobos body-fixed coordinate frame. For the transformation of the spacecraft trajectory information, which is commonly known with respect to the inertial frame J2000, the rotation model of Phobos is implicitly used. It includes time dependent parameters to describe Phobos' changing orientation with respect to the inertial frame (cf. Section 4.2.1).

Hence, a change of these rotational elements of the Phobos rotation model also changes the position of the camera at a certain epoch with respect to the Phobos body-fixed frame. Due to the relatively long period of precession, a successful re-determination of the corresponding parameters is not feasible. The high-frequency forced libration, however, was expected to be observable with a better accuracy than before.

An observation of the forced libration amplitude is only possible if the positional difference of surface features at the equator, with respect to the mean prime meridian, are significantly larger than the accuracy of the control points. Currently a value of -0.78° for the forced libration amplitude is recommended by the IAU (Seidelmann et al., 2007). Duxbury and Callahan (1989b) determined this value during the control network analysis and estimate the error to be $\pm 0.4^\circ$. This amplitude would correspond to a shift of the prime meridian at the equator of 180 m in one direction. Hence the amplitude of the forced libration is expected to be approximately ten times larger than the uncertainty of the control points.

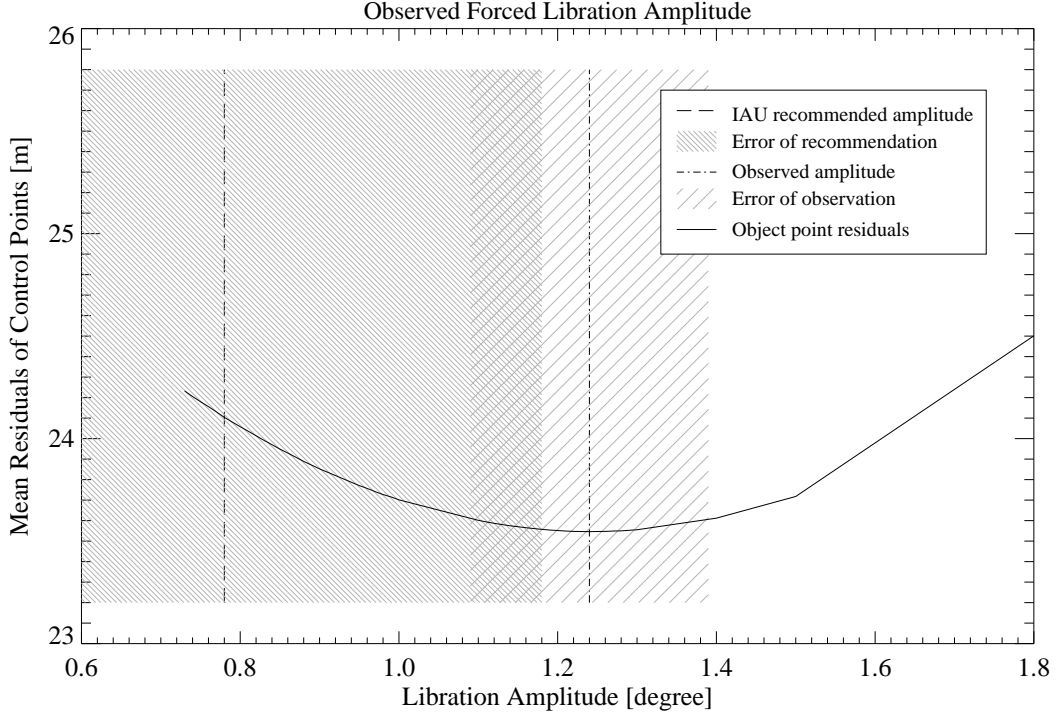


Figure 37: Residuals of control points over a variety of forced libration amplitudes. While currently the value of -0.78 ± 0.4 deg is recommended for the amplitude of the libration the control network points are in better agreement when assuming an amplitude of -1.24 deg with an estimated error of ± 0.15 deg.

It is anticipated that a variation of the forced libration is also changing the accuracy of the computed control points since stresses between the camera position, observing Phobos at a different position in its orbit, might be minimized or might possibly increase.

The control network was computed with a variety of forced libration amplitudes. Subsequent studies of the computed residuals of the control points showed that the lowest residuals of the points are obtained when assuming a forced libration amplitude of -1.24 degrees (Figure 37). The accuracy is estimated to be in the order of $\pm 0.15^\circ$, as a result of the coordinate uncertainties in the XY -plane. Since the forced libration is an oscillation about the Z -axis it only effects X and Y coordinates of points. The observed minimum is relatively weak but it is still considered to be significant since the recommended value is not within the error bounds of the observation and vice versa.

8.4.2 Modeling

The observed value of the forced libration amplitude can be compared with an analytical model. To model the forced libration amplitude, primarily a homogeneous mass distribution within Phobos was assumed applying equation (35). A $\hat{\gamma}$ of 0.1294 rad was computed when using the values of equation (34) for A , B and C resulting in a forced libration amplitude θ_A of -1.1° . This value is well within the error estimates of the observed amplitude for the forced libration. Hence, one could argue that Phobos has a homogeneous mass distribution. Previously, Duxbury (1991) made such an estimate relying on the observation of an amplitude of $0.8 \pm 0.3^\circ$ and a modeled amplitude of 0.9° . Both values were based on observations and models derived from VO images.

Nevertheless, it was tried to bring the observation and the analytic model of the forced libration into exact agreement. Therefore, the mass distribution model was altered, which

affects the moments of inertia. The mass estimate for Phobos and the density of regolith constrained the models. The first model (see Fig. 38(a)) included an outer layer with a lower density and constant thickness. The layer represents regolith which is known to have a bulk density of approximately 1.6 g/cm^3 (Busch et al., 2007). Agreement with the observed forced libration amplitude of -1.24° is not perfect. However, when a 5000 m thick layer of regolith is modeled, the forced libration amplitude increases to -1.18° . Based on estimates of Thomas et al. (1992) the thickness of the regolith layer on Phobos is assumed to be 35 m or up to 100 m when ejecta is re-accumulated to 100 %, such that the modeled 5,000 m thick layer is considered as unlikely.

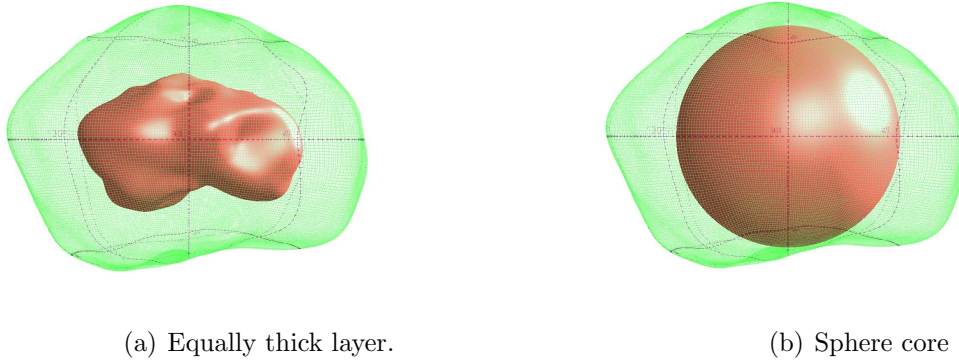


Figure 38: Simple density models of Phobos. The outer layer was modeled to have the bulk density of regolith of 1.6 g/cm^3 . While the scenario (a) would agree to the observed forced libration amplitude, the situation in (b) leads to a decreased libration amplitude.

Hence, the second model assuming a dense sphere inside Phobos was introduced (Fig. 38(b)). The radius of the sphere was determined by the smallest radius of a point ($r_{min}=8054 \text{ m}$) computed from the harmonic expansion model. This scenario decreases the forced libration amplitude and is thus equally implausible as the first model.

Another approach was to assume a certain density for the core and the layer. To model the observed libration amplitude, a layer of 1850 m would be necessary when the core has a density of 2.5 g/cm^3 and the mean density of the layer is assumed to be 1.0 g/cm^3 . Regarding the density of the core as grain density and assuming that Phobos' composition is similar throughout the body, the layer would have a porosity of 60 %. Since such a high porosity is believed to be unlikely, the layer must be less dense than the core. Assuming a maximum porosity of 40 % (Wilson et al., 1999), the layer would consist of material with a grain density of approx. 1.6 g/cm^3 . According to this model, Phobos could be considered as differentiated.

One further alternative was tested to bring the model of the forced libration into agreement with the observation. Here the top layer was set to a zero density, basically shrinking Phobos. In this case the observed forced libration amplitude can be modelled by reducing the radii of the surface points by 800 m. This could be an indication that larger void spaces exist below the surface. The remaining body of Phobos would then have a density of 2.3 g/cm^3 . The influence of a mass element on the principle moment of inertia is much higher the further it is located away from the corresponding principle axis (cf. Equation (28)). Hence, if void spaces were inside Phobos, these would need to occupy

a larger space than the computed 20 % of the total volume to compensate the higher influence of the outer mass elements and thus have the same effect on the forced libration amplitude. For such a density model, the porosity of Phobos is expected to be larger than 20 %.

All models have in common that the ratio between the moments of inertia A , B and C is not significantly changed. $\hat{\gamma}$ is the only variable in Eq. (35), since the eccentricity $e = 0.0151$ is well known (Burns, 1992). Hence, the modeled forced libration amplitude only changes significantly when the relation between the moments of inertia ($B - A$) and C is varying.

Table 22: Comparison of different mass distribution and the resulting forced libration amplitude.

Model	Thickness/ Radius	Layer Density	‘Core’ Density	Forced Libration Amplitude
A	5000 m	1.6 g/cm ³	3.18 g/cm ³	−1.18°
A	1850 m	1.0 g/cm ³	2.52 g/cm ³	−1.24°
B	8054 m	1.6 g/cm ³	2.31 g/cm ³	−0.98°
A	800 m	0.0 g/cm ³	2.35 g/cm ³	−1.24°

A) Constant thickness layer

B) Sphere inside

9 Discussion and Conclusions

The High Resolution Stereo Camera obtained several hundred images of the Martian moon Phobos. Based on these images a comprehensive study was commenced to constrain the knowledge of the motion, orientation, shape, and interior structure of this irregularly shaped natural satellite.

9.1 Motion in the Orbit

In the first part of the study, existing ephemerides models were compared to astrometric observations obtained from SRC fly-by images and observations of Phobos' shadow on the Martian surface. The position of Phobos could not be constrained clearly by the shadow observations as the results varied significantly in comparison with the orbit prediction models. The reasons for the scattering results are manifold. The definition of the point of the projection of the COM of Phobos onto Mars is one example. Due to the push-broom principle of the camera systems, which imaged the shadow, the shadow is not observed at an instant of time but over a period of time. It moves across the surface during this period forming an elongated shadow ellipse. Even though the center of the ellipse is well defined it may not coincide with the projection of the COM of Phobos which introduces an uncertain component into the analysis. Additional errors are introduced by the measurement of the line/sample coordinate of the shadow center, influencing the time and the location of the observation. While the scattering results did not permit to draw any conclusion of the size of the discrepancy between observation and prediction, the observations consistently indicated that Phobos is ahead of its predicted position which confirms previous astrometric observations.

The fly-by images together with a control point network (Duxbury, 1991) provided the opportunity to develop a method to obtain redundant information on the center of mass from one fly-by image. One of the largest error sources of such observations, the camera pointing, was eliminated due to the observation and analysis of background stars during each fly-by.

The results of the analysis of the fly-by images are much more consistent with orbit prediction models in comparison to the results of the shadow observations. Figure 19 indicates a small trend of increasing differences to the orbit model (Lainey et al., 2007). The trend is in the order of $\Delta Phobos = 2 \pm 0.5$ km over a time span of $\Delta t = 3.36$ years. Assuming that these differences describe only along-track variations, the mean acceleration, \hat{a}_{mean} , can be expressed by

$$\hat{a}_{mean} = \frac{\arctan \frac{\Delta Phobos}{a}}{\Delta t^2}, \quad (36)$$

where $a = 9377.2$ km equals the mean orbital radius of Phobos. Hence the derived astrometric data suggest an acceleration of $108.24 \times 10^{-5} \pm 0.47 \times 10^{-5}$ deg/year². Since all orbit prediction models do already account for a secular acceleration (Table 23), the observed $108.24 \times 10^{-5} \pm 0.47 \times 10^{-5}$ deg/year² would state an additional acceleration which appears to be relatively large when compared to the acceleration of 127.0×10^{-5} deg/year² already modeled in the respective ephemerides. Comparing the observations to the latest ephemerides models for Phobos (Jacobson, 2008, and the unpublished ROB model, Fig 39), no increasing difference between observations and ephemerides model can be observed. The current orbit model (MAR080) accounts for an acceleration which is slightly

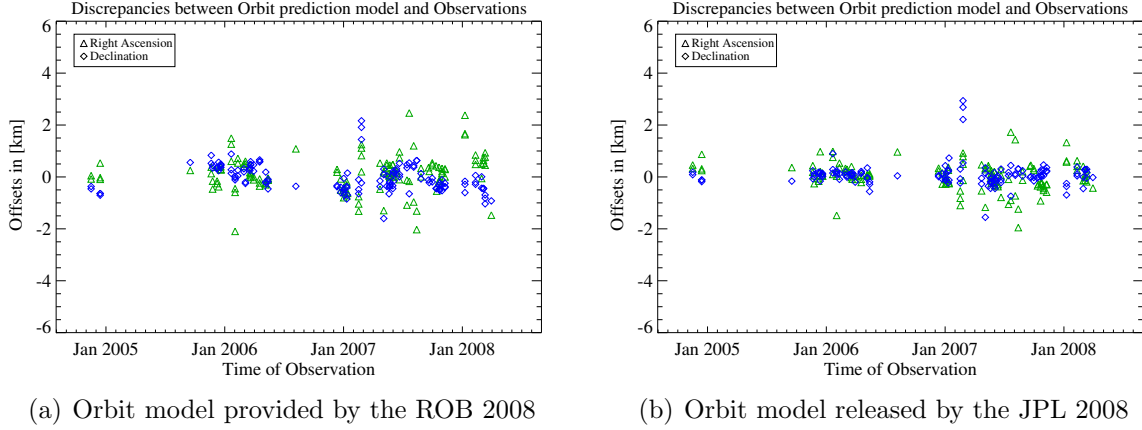


Figure 39: Comparing the astrometric observations to orbit prediction models of Phobos of 2008. No increase of the discrepancy over time is apparent.

larger than the acceleration derived from the previous orbit model MAR063 (cf. Table 23). This disparity is much smaller than the above computed acceleration.

Jacobson (2008) compares the in-orbit (along-track) differences of the two orbit model solutions (MAR063 and MAR080). Figure 40 indicates that there is a change in the mean motion and the acceleration. Whether the secular trend is due to uncertainties of the orbit prediction model MAR063 or a real effect is uncertain. The diagram (Fig. 40) also shows that for the time period of the observations of this study an increase of the along-track discrepancies of approximately 700 m is expected. Hence, it is concluded that no acceleration, other than the secular effect, which orbit models already account for, can directly be observed in the derived astrometric observations. Fitting the mean longitude to the observations might reveal a slight acceleration.

Table 23: Observed and fitted secular accelerations for Phobos. The latest orbit prediction models already include these accelerations.

Reference	Determined from fit to	Secular Acceleration $\hat{a}_{mean} \times 10^{-5} \text{deg/year}^2$
Jacobson et al. (1989)	Orbit model	124.9 ± 1.8
Bills et al. (2005)	MOLA Observations	136.7 ± 0.6
Rainey and Aharonson (2006)	MOC Observations	133.4 ± 0.6
Jacobson and Rush (2006)	Orbit model (MAR063)	124.4 ± 0.5
Lainey et al. (2007)	Orbit model	127.0 ± 1.5
Jacobson (2008)	Orbit model (MAR080)	125.4 ± 0.4

9.2 Shape and Physical Parameters

Control points were measured and a control network computed during the second phase of this study. Observations were based on SRC and Viking Orbiter images. The control network includes 3D-coordinates of 665 control points and is independent from any previous control network. Least-squares bundle block adjustments, relying on the principle of forward ray intersections and the collinearity equations, were solved to determine the 3D-coordinates. To add constraints to the spherical harmonic function model, points

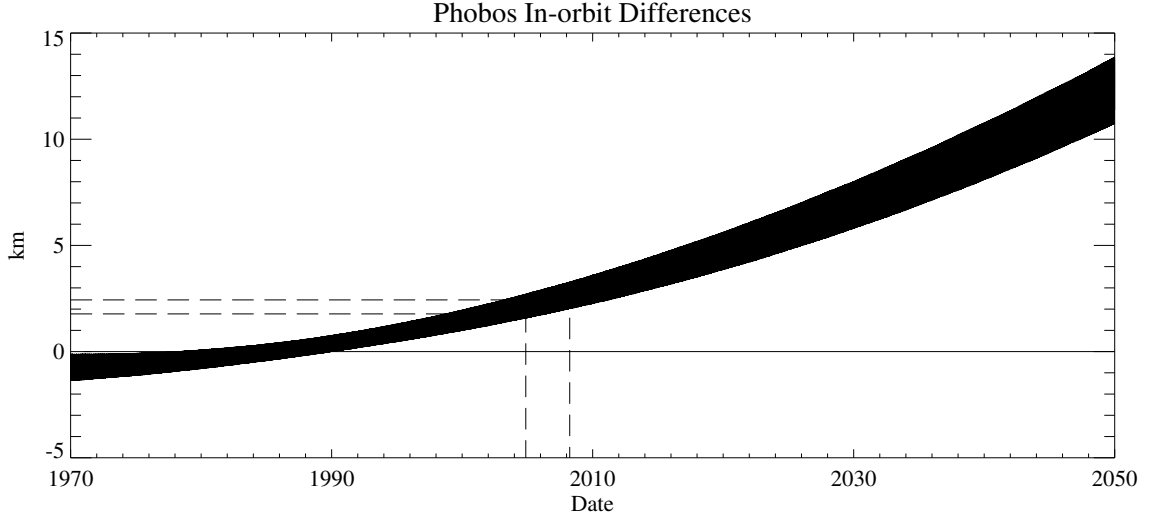


Figure 40: Difference of MAR080 minus MAR063 orbit model in along-track direction (Jacobson, 2008). The value of the secular acceleration changes only slightly from the previous orbit model to the current orbit model and seems to indicate an acceleration of Phobos. The dashed lines show the time period of the current astrometric observations. An advance of Phobos in its orbit by approx. 700 m appears to be likely.

observed in HRSC images were added to the control point network. Mean accuracies of the derived 3D-coordinates are in the order of the mean pixel resolution of the images of ± 17 m. The coverage map with control point locations and their errors (Fig. 25) gives a clear indication which areas were covered by VO images. Here, the uncertain navigation information decreased the quality of the determined control points significantly.

Based on the control points, coefficients of a spherical harmonic function of degree and order 17 were determined. A volume of $5689 \pm 60 \text{ km}^3$ and a corresponding bulk density of $1.875 \pm 0.008 \text{ g/cm}^3$ were computed considering the determined shape model and the latest mass estimates for Phobos (Jacobson, 2008; Andert et al., 2008). Compared to previous volume estimates the accuracy has significantly improved by this study. Assuming a homogeneous mass distribution, the principle moments of inertia A , B and C were derived by numerical integration of the spherical expansion model. The values of $A=0.3362$, $B=0.3871$ and $C=0.4773$ were computed which were used to model the forced libration amplitude.

Section 8.4.1 describes that the solution of the control network involves the transformation of the spacecraft orientation data into the body fixed frame of Phobos, implicitly applying the IAU recommended orientation parameters (cf. Section 4.2.1). This was exploited to re-estimate the forced libration amplitude of Phobos. An amplitude of -1.24° , significantly differing from the IAU recommended value, was observed. This agrees well with the value of -1.06° determined by Jacobson (2008) derived from an orbit fit to spacecraft astrometric observations. The observation was also confirmed by the spherical harmonic expansion model computed within the scope of this study assuming a homogeneous mass distribution. Here an amplitude of -1.1° was modeled.

Even though the modeled and the observed libration amplitudes are statistically equal, it was tried to bring the model into exact agreement with the observation. It was anticipated that this provides further clues on the interior structure of Phobos since the modeled libration is dependent on the mass distribution. A perfect agreement between the modeled and observed forced libration amplitude is reached when a layer of zero density and 800 m

thickness is assumed, literally shrinking Phobos. This could be an indication that large void spaces or volumes filled with low density material, such as water-ice, are present within Phobos. Assuming that the remaining body is free of any porosity, a grain density of 2.3 g/cm^3 is derived.

An estimate on the composition of Phobos can be made on the basis of the bulk density and the surface reflectance. The determined bulk density of Phobos is comparable to the density measured for the meteorite Orgueil (Britt and Consolmagno, 1997). The grain density of the meteorite, 2.1 g/cm^3 , is in good agreement with the computed grain density of Phobos – cf. Table 22, where it is assumed that the core density of the last entry equals the grain density. This corresponds to a porosity of approximately 20 %. Hence, there is a possibility that Phobos is of similar composition as Orgueil which is classified as carbonaceous chondrite of the CI class. If the computed 20 % porosity were entirely due to macroporosity – large voids due to fractures or cracks in contrast to microporosity which accounts for inclusions within grains and micro cracks – than this would be an indication that Phobos is extensively fractured (Britt and Consolmagno, 2001) which in turn would correspond to the heavily cratered surface of Phobos. The low albedo of Phobos (Simonelli et al. (1998) reported of a reflectance of approximately 0.07) also speaks for carbonaceous material.

However, spectral observations of the satellite with the Imager for Mars Pathfinder, suggested that organic-rich compositions or optical altered mafic (magnesium and Fe-rich) compositions are possibly present (Murchie et al., 1998) and that Phobos is spectrally different from other C-type asteroids – dark carbonaceous objects – since it is much redder. Since the shape and expansion of Phobos was determined with a high certainty during this study, the void spaces, preliminary modeled as top layer, must be located inside Phobos. Hence, masses are moved further away from the principle axes having a greater influence on the momentum. To meet the constraint of the forced libration amplitude, the total volume of the voids would need to increase to compensate the shift of masses. This in turn would increase the grain density of Phobos and the porosity of Phobos. Wilson et al. (1999) showed that asteroids are likely to be fractured by collisional break-up and subsequent gravitational reassembly leading to porosities of approximately 40 %. Further impacts would not greatly reduce the porosity because of the scattering of the impact energy through the existing porosity. Assuming a porosity of 40 % the grain density for Phobos would be on the order of 3.1 g/cm^3 . A similar grain density is known for Olivine which can also have a reddish visual nature (depending on the content of ferric elements) and has a relatively low albedo (Matthes, 2001). Since Phobos is orbiting deep in the gravity field of Mars it is exposed to continuous forces originating from the Martian gravity field. A body with a porosity of 40 % is unlikely to withstand such torques over long time periods. Thus, it is highly unlikely that Phobos has a high porosity.

Even though this study places further constraints on composition models for Phobos a certain conclusion can not be drawn. The two theories on the composition of Phobos discussed above represent equally likely possibilities. These are based on a two layer mass distribution model which does not account for local variations of the mass distribution, e.g. in the area of Stickney, where the impact could have compacted materials.

The map and the digital terrain model determined during this study contribute to the Phobos-Grunt mission to be launched in 2011. While the map was already in use for the exact determination of the recently selected landing site candidates (Basilevsky et al., 2009), the DTM might be implemented into the on-board processing to assure a safe automated landing of the probe selecting the return sample.

The determined spherical harmonic function model can also contribute to Phobos-Grunt and future mission to Phobos. It can be used to establish a first approximation of the low degree and order gravity coefficients. Canadian mission planners also identified Phobos as a possible science target (Lee et al., 2008).

9.3 Outlook

Currently, the Mars Express Mission is in its second extension, and is going to be extended further until the end of 2009. This will provide additional opportunities to observe Phobos in its orbit. Furthermore, images, which were not yet analyzed, need to be processed to exploit the entire information available from the HRSC data for orbit fitting procedures. Astrometric observations derived from HRSC images could be complemented by observations obtained by other instruments on Mars Express. The Visible and Infrared Mineralogical Mapping Spectrometer (OMEGA) and the Sub-Surface Sounding Radar Altimeter (MARSIS), for example, have observed Phobos during fly-bys. It needs to be evaluated whether these observations are suitable to retrieve astrometric observations of Phobos or if it is possible to combine for instance range measurements of MARSIS with observations by the HRSC.

With more close range observations of Phobos through the SRC and HRSC, the control network can be densified. This could subsequently lead to a spherical expansion model of higher degree and order, as more control points are determined. A re-determination of rotational parameters for Phobos would also be desirable and is more and more feasible with the increasing time period of continuous observations. An estimation of rotational parameters should be obtained by integrating the solution for the rotational elements into the least-squares bundle block adjustment rather than by empirical means. This would also provide a verification for current estimates of the forced libration amplitude and could further constrain a density distribution model.

The determined digital terrain model is currently the best available for Phobos. However, it does have deficits, especially in regions where Viking orbiter images are used. Further optimization would be welcome and necessary to support the Russian Phobos-Grunt mission.

The Russian-led mission is also expected to further the knowledge of the gravity field of Phobos, and thus on the mass distribution. Since the spacecraft is supposed to orbit Phobos several times at distances of approximately 50 km to the surface (Tuchin, 2007), it is anticipated that the gravity field can be determined from tracking data, which need to be known accurately to assure a safe landing of the probe.

List of Abbreviations

CCD	Charge-Coupled Device
COF	Center of Figure
COM	Center of Mass
DLR	Deutsches Zentrum für Luft- und Raumfahrt / German Aerospace Center
DTM	Digital Terrain Model
ET	Ephemeris Time
FOV	Field of View
HRSC	High Resolution Stereo Camera; Camera system on the European Mars Express Mission
JPL	Jet Propulsion Laboratory
MDIM	Mars Digital Image Model
MEX	Mars Express
MGS	Mars Global Surveyor; NASA operated spacecraft
MOC	Mars Observer Camera
MOC	Mars Orbiter Camera; Camera on-board the Mars Global Surveyor Mission
MOLA	Mars Orbiter Laser Altimeter
MRO	Mars Reconnaissance Orbiter
NAC	Narrow Angle Camera
NAIF	Navigation and Ancillary Information Facility
ROB	Royal Observatory of Belgium
SPICE	Information system to assist scientist and engineers working with scientific data from planetary exploration mission and designing space mission
SRC	Super Resolution Channel; Channel of the HRSC with a separate optical system and sensor system
TDB	Dynamical Barycentric Time
UTC	Coordinated Universal Time
VIS	Visual-Imaging System; Camera system of the Viking Orbiters
VO	Viking Orbiter
WAC	Wide Angle Camera

List of Symbols

α, β, γ	Rotation angle about the x, y and z axis, respectively
α_0	Right ascension of the rotation axis
a	Semi major axis of the orbital ellipse
A, B, C	Principle moments of inertia
A_{nm}, B_{nm}	Coefficients of the surface harmonic expansion
C_{20}, C_{22}	Gravitation coefficients
δ_0	Declination of the rotation axis
d	Time interval of one day
\bar{E}	Identity matrix
$\vec{e}_x, \vec{e}_y, \vec{e}_z, \vec{e}_r$...	Unit vector with respect to coordinate axes
E	Kinetic energy
e	Eccentricity of the Phobos orbit
\mathbf{F}	Cartesian coordinate vector
ϕ	Latitude of a point with respect to the body-fixed frame
f	Focal length of a camera lens
F_r	Element of a spherical coordinate vector
F_x, F_y, F_z	Elements of the Cartesian coordinate vector
G	The gravitational constant, $G = 6.67259 \times 10^{-20} kg^{-1} km^3 sec^{-2}$
I	Eigenvalue
i	Inclination of the Phobos orbit w.r.t. the Martian equator
$\hat{\mathbf{J}}$	Inertia Tensor diagonalized
\mathbf{J}	Moment of Inertia tensor
J_2	Gravity field coefficient defining the oblateness of the field
$J_2(t)$	Time dependent Martian gravity coefficient
λ	Longitude of a point with respect to the body-fixed frame
M	The mass of a body
m_i	Mass of one mass element
n, m	Degree and order, respectively, related to the spherical harmonic function

$\dot{\Omega}$	Time dependent variation of the angle between the vernal equinox and the ascending node
$\hat{\omega}^{(i)}$	Eigenvector
$\vec{\omega}$	Angular velocity
$P(x)$	Associated Legendre polynomial
pix	Metric size of one pixel element
$\rho(\vec{x})$	Density of a mass element at the position \vec{x}
r	Radius of radial distance
σ	Error estimate of an observed or computed value
θ_A	Forced libration amplitude
T	Time interval in Julian centuries of 36525 days
TA	The true anomaly
$u(\phi, \lambda)$	Function of the radius
\vec{V}	Translational velocity vector
\vec{v}	Velocity vector
V	Volume
W	Angle between the ascending node and the prime meridian measured along the equator
\vec{x}	Positional vector
x, y	Coordinates with respect to the image coordinate frame
X, Y, Z	Coordinates with respect to the inertial coordinate frame
x_0, y_0	Line/sample coordinates of the principle point of a camera

List of Figures

1	Samples of HRSC and SRC images of Phobos.	6
2	Scheme of the study.	7
3	The orbits of Deimos, Phobos and Mars Express about Mars as in August 2008.	9
4	Views of Phobos as observed during different fly-bys.	10
5	Diagramm of the Viking Orbiter Visual-Imaging System.	14
6	Diagram of the Viking Orbiter Visual-Imaging System.	15
7	HRSC viewing geometry and operating principle.	16
8	Image of the flight model of the HRSC with SRC.	18
9	SRC background star observations.	19
10	Coordinate frame tree of the HRSC.	21
11	Geometry of eclipse through Phobos.	28
12	Ground tracks of Phobos' shadow and MEX spacecraft.	29
13	Dependency of the shadow location on the height of the terrain.	30
14	Phobos shadow projected onto differently declined surfaces	31
15	Across- and along-track discrepancies of observations.	33
16	Along- and across-track discrepancies between shadow observations and orbit models.	34
17	Reconstructed shadow ellipse.	35
18	Fly-by distances during SRC observations.	38
19	Fly-by discrepancies compared to the ROB orbit prediction model.	43
20	Along-track discrepancies between orbit model and astrometric observations.	44
21	The first Phobos control point network.	48
22	Geometric correction of Viking Orbiter images.	50
23	Uncertainties in object space depending on the error source.	51
24	Flow chart of control point analysis.	52
25	Overview of control point locations and their accuracies.	54
26	Schematic diagram of stereo covered areas during one fly-by.	57
27	HRSC sample image from orbit 0756	58
28	HRSC sample image from orbit 5851	58
29	Percent of accepted conjugate points.	62
30	Scheme of the mosaicking process of the global DTM for Phobos	63
31	Color coded and shaded Global DTM.	64
32	Accuracy map of the global DTM.	64
33	Zonal, Sectorial and Tesseral harmonics.	66
34	Control point residuals over degree and order development	67

35	Details of the expansion model in comparison with one observation	69
36	Difference of analytic computed values and values determined by numeric integration.	73
37	Observation of the forced libration amplitude.	78
38	Visualization of simple density models.	79
39	Comparison of 2008 orbit models to astrometric observations.	82
40	Along-track discrepancies of different orbit models	83
41	Map Stickney showing the leading side of Phobos from 0° to 180° West in the central latitudes.	105
42	Map Roche showing the trailing side of Phobos from 180° to 360° West in the central latitudes.	106
43	Map sheet including the pole areas of Phobos. Grildrig and Hall are the largest surface features closest to the poles.	107

List of Tables

1	Estimates of Phobos' properties as currently published.	9
2	Missions returning image date of Phobos	12
3	HRSC channel properties.	17
4	Common image compression modes for Phobos fly-by imaging with the HRSC.	17
5	Geometric properties of the SRC camera (Oberst et al., 2008).	18
6	Values used to compute the secular motion of the ascending node Ω	23
7	SPICE is an acronym. Information in the SPICE system is stored in Kernels which contents is summarized in this table (Acton and Baalke, 2007).	25
8	Phobos shadow observations by the HRSC	29
9	Differences of observed line coordinates to traced line coordinates of the shadow center in comparison with results from different software tools.	32
10	Results of shadow observations in HRSC images.	36
11	Number of HRSC images depicting Phobos.	38
12	Comparison of star catalogues.	40
13	Estimated accuracies of the JPL- and ROB orbit prediction models.	43
14	Comparison of orbit models with fly-by observations.	45
15	Differences between the ROB-model (Lainey et al., 2007) and the JPL-model (Jacobson and Rush, 2006)	46
16	Advantages and disadvantages of the different data sets regarding control point determination.	49
17	Object point accuracies for the different bundle block adjustment models.	53
18	Methods that were used to model Phobos' shape.	55
19	Map projections used for pre-rectification during matching procedures	60
20	Possible geometries of point observations.	61
21	Computed bulk density depending on current mass estimates.	74
22	Comparison of different mass distribution and the resulting forced libration amplitude.	80
23	Observed and fitted secular accelerations for Phobos.	82
24	Results of the analysis of Phobos' shadow images.	100
25	Observed Phobos astrometric positions between Nov. 16, 2004 and Mar. 29, 2009.	101
26	Degree and order 17 coefficients	103

Bibliography

- C. Acton and R. Baalke. The navigation and ancillary information facility, October 2007. URL <http://naif.jpl.nasa.gov/naif/pds.html>. Last visited: 13. Feb. 2007.
- C. H. Acton. SPICE Products Available to the Planetary Science Community. In *Lunar and Planetary Institute Conference Abstracts*, volume 30 of *Lunar and Planetary Institute Conference Abstracts*, pages 1233–+, March 1999.
- A. L. Albee, R. E. Arvidson, F. Palluconi, and T. Thorpe. Overview of the Mars Global Surveyor mission. *Journal of Geophysical Research* , 106:23291–23316, October 2001. doi: 10.1029/2000JE001306.
- T. P. Andert, M. Pätzold, and B. Häusler. Precise mass determination of the Mars moon Phobos from Mars Express close flybys. *AGU Fall Meeting Abstracts*, pages A1431+, December 2008.
- B. A. Archinal, R. L. Kirk, T. C. Duxbury, E. M. Lee, R. Sucharski, and D. Cook. Mars Digital Image Model 2.1 Control Network. In S. Mackwell and E. Stansbery, editors, *Lunar and Planetary Institute Conference Abstracts*, volume 34 of *Lunar and Planetary Institute Conference Abstracts*, pages 1485–+, March 2003.
- G. A. Avanesov, B. I. Bonev, V. Boicheva, F. Kempe, A. T. Bazilevskii, and T. Duxbury. Television observations of Phobos. *Nature* , 341:585–587, October 1989. doi: 10.1038/341585a0.
- W. Baarda. *A testing procedure for use in Geodetic networks*, volume 2 of *Publications on Geodesy, New Series*. Netherlands Geodetic Commission, Rijkscommissie voor Geodesie, Kanaalweg 4, Delft, Netherlands, 1968.
- W. B. Banerdt and G. A. Neumann. The Topography (and Ephemeris) of PHOBOS from MOLA Ranging. In *Lunar and Planetary Institute Conference Abstracts*, pages 2021–+, March 1999.
- A. T. Basilevsky, G. Neukum, G. Michael, A. Dumke, T. Roatsch, H. Hoffmann, J. Oberst, M. Wählisch, K. Willner, T. V. Shingareva, E. A. Akim, A. G. Tuchin, V. P. Fedotov, E. G. Ruzskiy, A. V. Zakharov, and T. C. Duxbury. The MEX HRSC / SRC images of PHOBOS as a support of FOBOS-GRUNT mission. Mars Exploration workshop , ESTEC, The Netherlands, January 2009.
- R. M. Batson, K. Edwards, and T. C. Duxbury. *Geodesy and cartography of the Martian satellites*, pages 1249–1256. Mars, 1992.
- J. Beck, S. Hulme, R. Baalke, C. Waste, R. Passaniti, C. Johnson, S. Lievense, L. Doran, and C. Sharkey. NASA’s Mars Exploration Programm. WWW, 2008. URL <http://mars.jpl.nasa.gov/missions/>. Last visited: 06. Aug. 2008.
- J. F. Bell, M. T. Lemmon, T. C. Duxbury, M. Y. H. Hubbard, M. J. Wolff, S. W. Squyres, L. Craig, and J. M. Ludwinski. Solar eclipses of Phobos and Deimos observed from the surface of Mars. *Nature* , 436:55–57, July 2005. doi: 10.1038/nature03437.
- J. Bendig. Kartierung und Vermessung der Schatten vom Marsmond Phobos. Diploma thesis, Technische Fachhochschule Berlin, October 2006.

- B. G. Bills and R. L. Comstock. Spatial and temporal patterns of solar eclipses by Phobos on Mars. *JGR*, 110(E9):4004–+, April 2005. doi: 10.1029/2003JE002209.
- B. G. Bills, G. A. Neumann, D. E. Smith, and M. T. Zuber. Improved estimate of tidal dissipation within Mars from MOLA observations of the shadow of Phobos. *JGR*, 110(E9):7004–+, July 2005. doi: 10.1029/2004JE002376.
- D. T. Britt and G. J. Consolmagno. The porosity of meteorites and asteroids - Results from the Vatican Collection of meteorites. In *Lunar and Planetary Institute Conference Abstracts*, volume 28 of *Lunar and Planetary Inst. Technical Report*, pages 159–+, March 1997.
- D. T. Britt and G. J. Consolmagno. Asteroid Bulk Density: Implications for the Structure of Asteroids. In *Lunar and Planetary Institute Conference Abstracts*, volume 32 of *Lunar and Planetary Institute Conference Abstracts*, pages 1611–+, March 2001.
- J. A. Burns. *Contradictory clues as to the origin of the Martian moons*, pages 1283–1301. Mars, 1992.
- M. Bursa, Z. Martinec, and K. Pec. Principal moments of inertia, secular love number and origin of PHOBOS. *Advances in Space Research*, 10:67–70, 1990. doi: 10.1016/0273-1177(90)90328-W.
- M. W. Busch, S. J. Ostro, L. A. M. Benner, J. D. Giorgini, C. Magri, E. S. Howell, M. C. Nolan, A. A. Hine, D. B. Campbell, I. I. Shapiro, and J. F. Chandler. Arecibo radar observations of Phobos and Deimos. *Icarus*, 186:581–584, February 2007. doi: 10.1016/j.icarus.2006.11.003.
- M. Caplinger. Software Interface Specification Narrow Angle and Wide Angle Standard Data Products. Technical report, Malin Space Science Systems, Inc., September 1999. URL http://pds-imaging.jpl.nasa.gov/data/mgs-m-moc-na_wa-2-sdp-10-v1.0/mgsc_1182/document/mocsis.pdf.
- B. Fong Chao and D. P. Rubincam. The Gravitational Field of Phobos. *Geophysical Research Letters*, 16(8):859+–, August 1989.
- A. Chicarro. The Mars-Express Mission: Status and Scientific Objectives. In B. H. Foing and M. Perry, editors, *Exploration and Utilisation of the Moon*, volume 462 of *ESA Special Publication*, pages 383–+, September 2000.
- A. Cicchetti, D. Calabrese, E. Flamini, S. Giuppi, C. Nenna, R. Noschese, R. Orosei, J. J. Plaut, A. Safaeinili, and R. Seu. Radar Sounding of Phobos by MARSIS. *AGU Fall Meeting Abstracts*, pages A6+, December 2008.
- T. Duxbury, M. Wang, and H. Herkenhoff. The Figure of Phobos: an Update from the PHOBOS Mission. In *Lunar and Planetary Institute Conference Abstracts*, volume 22 of *Lunar and Planetary Inst. Technical Report*, pages 327–+, March 1991.
- T. C. Duxbury. PHOBOS - Control network analysis. *Icarus*, 23:290–299, October 1974.
- T. C. Duxbury. The figure of PHOBOS. *Icarus*, 78:169–180, March 1989. doi: 10.1016/0019-1035(89)90075-4.

- T. C. Duxbury. An analytic model for the PHOBOS surface. *Planetary and Space Science*, 39:355–376, February 1991. doi: 10.1016/0032-0633(91)90157-6.
- T. C. Duxbury and J. D. Callahan. PHOBOS and Deimos Cartography. In *Lunar and Planetary Institute Conference Abstracts*, volume 13 of *Lunar and Planetary Inst. Technical Report*, pages 190–+, March 1982.
- T. C. Duxbury and J. D. Callahan. PHOBOS and Deimos astrometric observations from Viking. *A&A*, 201:169–176, July 1988.
- T. C. Duxbury and J. D. Callahan. PHOBOS and Deimos astrometric observations from Mariner 9. *A&A*, 216:284–293, June 1989a.
- T. C. Duxbury and J. D. Callahan. PHOBOS and Deimos control networks. *Icarus*, 77: 275–286, February 1989b. doi: 10.1016/0019-1035(89)90090-0.
- P. Ehrenfreund, D. P. Glavin, O. Botta, G. Cooper, and J. L. Bada. Extraterrestrial amino acids in Orgueil and Ivuna: Tracing the parent body of CI type carbonaceous chondrites. *Proceedings of the National Academy of Sciences of the United States of America*, 98(5):2138–2141, 2001. doi: 10.1073/pnas.051502898. URL <http://www.pnas.org/content/98/5/2138.abstract>.
- E. J. Garboczi. Three-dimensional mathematical analysis of particle shape using x-ray tomography and spherical harmonics: Application to aggregates used in concrete. *Cement and Concrete Research*, 32(10):1621 – 1638, October 2002. URL <http://fire.nist.gov/bfrlpubs/build02/PDF/b02018.pdf>.
- P. Gläser. Implementierung eines Bahnintegrators und Untersuchung von Störbeschleunigungen am Beispiel des Marsmondes Deimos. Diploma thesis, Universität Stuttgart, March 2008.
- H. Goldstein. *Classical Mechanics*. Addison-Wesley, 2. ed. edition, 1980. XIV, 672 S.
- R. Greeley and R. M. Batson. *Planetary Mapping*. Planetary Mapping, 1990.
- K. Gwinner, F. Scholten, M. Spiegel, R. Schmidt, B. Giese, J. Oberst, R. Jaumann, G. Neukum, and HRSC Co-Investigator Team. Hochauflösende digitale Geländemodelle auf der Grundlage von Mars Express HRSC-Daten. *Photogrammetrie Fernerkundung Geoinformation*, Jahrgang 2005(5):387 – 394, 2005. ISSN 1432-8364.
- C. Heipke. Overview of Image Matching Techniques. In *Proceedings of the OEEPE-Workshop on Application of Digital Photogrammetric Workstations.*, 1996. Lausanne 4-6 March 1996.
- C. Heipke, J. Oberst, J. Albertz, M. Attwenger, P. Dorninger, E. Dorrer, M. Ewe, S. Gehrke, K. Gwinner, H. Hirschmüller, J. R. Kim, R. L. Kirk, H. Mayer, J.-P. Muller, R. Rengarajan, M. Rentsch, R. Schmidt, F. Scholten, J. Shan, M. Spiegel, M. Wählisch, G. Neukum, and the HRSC Co-Investigator Team. Evaluating planetary digital terrain models—The HRSC DTM test. *Planetary and Space Science*, 55:2173–2191, November 2007. doi: 10.1016/j.pss.2007.07.006.
- R. A. Jacobson. Ephemerides of the Martian Satellites - MAR080. IOM 343R-08-006, JPL, Sep 2008.

- R. A. Jacobson. The Orbits of the Martian Satellites. In *AAS/Division for Planetary Sciences Meeting Abstracts*, volume 40 of *AAS/Division for Planetary Sciences Meeting Abstracts*, pages 46.05–+, September 2008.
- R. A. Jacobson and B. Rush. Ephemerides of the martian satellites - mar063. JPL IOM 343R-06-004, April 2006.
- R. A. Jacobson, S. P. Synnott, and J. K. Campbell. The orbits of the satellites of Mars from spacecraft and earthbased observations. *A&A*, 225:548–554, November 1989.
- R. Jaumann, G. Neukum, T. Behnke, T. C. Duxbury, K. Eichentopf, J. Flohrer, S. v. Gasselt, B. Giese, K. Gwinner, E. Hauber, H. Hoffmann, A. Hoffmeister, U. Köhler, K.-D. Matz, T. B. McCord, V. Mertens, J. Oberst, R. Pischel, D. Reiss, E. Ress, T. Roatsch, P. Saiger, F. Scholten, G. Schwarz, K. Stephan, and M. Wählisch. The high-resolution stereo camera (HRSC) experiment on Mars Express: Instrument aspects and experiment conduct from interplanetary cruise through the nominal mission. *Planetary and Space Science*, 55:928–952, May 2007.
- Y. Kolyuka, V. Tikhonov, N. Ivanov, V. Polyakov, G. Avanesov, V. Heifetz, B. Zhukov, E. Akim, V. Stepanyants, O. Papkov, and T. Duxbury. PHOBOS and Deimos astrometric observations from the PHOBOS mission. *A&A*, 244:236–241, April 1991.
- A. S. Konopliv, C. F. Yoder, E. M. Standish, D.-N. Yuan, and W. L. Sjogren. A global solution for the Mars static and seasonal gravity, Mars orientation, Phobos and Deimos masses, and Mars ephemeris. *Icarus*, 182:23–50, May 2006. doi: 10.1016/j.icarus.2005.12.025.
- V. Lainey. personal communication, 2007.
- V. Lainey, V. Dehant, and M. Pätzold. First numerical ephemerides of the Martian moons. *A&A*, 465:1075–1084, April 2007. doi: 10.1051/0004-6361:20065466.
- P. Lee, A. R. Hildebrand, R. Richards, and Prime Mission Team. The PRIME (Phobos Reconnaissance and International Mars Exploration) Mission and Mars Sample Return. In *Lunar and Planetary Institute Conference Abstracts*, volume 39 of *Lunar and Planetary Institute Conference Abstracts*, pages 2268–+, March 2008.
- T. M. MacRobert. *Spherical Harmonics*, volume 98. Pergamon Press Ltd., 3rd edition, 1967.
- M. C. Malin, G. E. Danielson, M. A. Ravine, and T. A. Soulanille. Design and development of the mars observer camera. *International Journal of Imaging Systems and Technology*, 3(2):76–91, 1991. doi: 10.1002/ima.1850030205. URL <http://dx.doi.org/10.1002/ima.1850030205>. Copyright ©1991 John Wiley & Sons, Inc.
- C. Markwardt. Markwardt IDL Library. Webpage, 2008. URL <http://cow.physics.wisc.edu/~craigm/idl/>. Last visited: 18. Dec. 2008.
- M. S. Matthes. *Mineralogie: Eine Einführung in die spezielle Mineralogie, Petrologie und Lagerstättenkunde*. Springer Verlag, Berlin, Heidelberg, 2001.
- D. D. McCarthy and G. Petit. *IERS Conventions (2003)*. IERS Technical Note; 32. Verlag des Bundesamts für Kartographie und Geodäsie, 2004. ISBN 3-89888-884-3. paperback.

- R. Z. Sagdeev and A. V. Zakharov. A Brief History of the Expedition to PHOBOS. *Soviet Astronomy Letters*, 16:125–+, April 1990.
- P. P. Saiger. *Entwicklung, Implementierung und Erprobung eines planetaren Informationssystems auf Basis von ArcGIS*. PhD thesis, Mathematisch - Naturwissenschaftliche Fakultät der Universität Potsdam, Dez 2007. URL http://opus.kobv.de/ubp/volltexte/2007/1587/pdf/saiger_diss.pdf.
- F. Scheck. *Theoretische Physik 1, Mechanik*. Springer, XIX, 573 S. edition, 2007.
- F. Scholten, K. Gwinner, T. Roatsch, K.-D. Matz, M. Wählisch, B. Giese, J. Oberst, R. Jaumann, G. Neukum, and HRSC Co-I-Team. Mars Express HRSC Data Processing - Methods and Operational Aspects. *PERS*, 71(10):1143 – 1152, 10 2005.
- P. K. Seidelmann, V. K. Abalakin, M. Bursa, M. E. Davies, C. d. Bergh, J. H. Lieske, J. Oberst, J. L. Simon, E. M. Standish, P. Stooke, and P. C. Thomas. Report of the IAU/IAG Working Group on Cartographic Coordinates and Rotational Elements of the Planets and Satellites: 2000. *Celestial Mechanics and Dynamical Astronomy*, 82: 83–111, January 2002.
- P. K. Seidelmann, B. A. Archinal, M. F. A’Hearn, D. P. Cruikshank, J. L. Hilton, H. U. Keller, J. Oberst, J. L. Simon, P. Stooke, D. J. Tholen, and P. C. Thomas. Report of the IAU/IAG Working Group on Cartographic Coordinates and Rotational Elements: 2003. *Celestial Mechanics and Dynamical Astronomy*, 91:203–215, March 2005. doi: 10.1007/s10569-004-3115-4.
- P. K. Seidelmann, B. A. Archinal, M. F. A’Hearn, A. Conrad, G. J. Consolmagno, D. Hestroffer, J. L. Hilton, G. A. Krasinsky, G. Neumann, J. Oberst, P. Stooke, E. F. Tedesco, D. J. Tholen, P. C. Thomas, and I. P. Williams. Report of the IAU/IAG Working Group on cartographic coordinates and rotational elements: 2006. *Celestial Mechanics and Dynamical Astronomy*, 98:155–180, July 2007. doi: 10.1007/s10569-007-9072-y.
- S. Semm. Erstellung eines Bildatlanten des Mars-Mondes Phobos aus hochauflösenden Bilddaten zweier Weltraum-Missionen. Bachelor thesis, Technische Fachhochschule Berlin, 2008.
- D. P. Simonelli, P. C. Thomas, B. T. Carcich, and J. Veverka. The generation and use of numerical shape models for irregular Solar System objects. *Icarus*, 103:49–61, May 1993. doi: 10.1006/icar.1993.1057.
- D. P. Simonelli, M. Wisz, A. Switala, D. Adinolfi, J. Veverka, P. C. Thomas, and P. Helfenstein. Photometric Properties of PHOBOS Surface Materials From Viking Images. *Icarus*, 131:52–77, January 1998. doi: 10.1006/icar.1997.5800.
- A. T. Sinclair. The orbits of the satellites of Mars determined from earth-based and spacecraft observations. *A&A*, 220:321–328, August 1989.
- S. F. Singer. Origin of the Martian Satellites Phobos and Deimos. In *Exploration of Phobos and Deimos*, pages 36–+, 2007.
- D. E. Smith, M. T. Zuber, H. V. Frey, J. B. Garvin, J. W. Head, D. O. Muhleman, G. H. Pettengill, R. J. Phillips, S. C. Solomon, H. J. Zwally, W. B. Banerdt, T. C. Duxbury, M. P. Golombek, F. G. Lemoine, G. A. Neumann, D. D. Rowlands, O. Aharonson,

- P. G. Ford, A. B. Ivanov, C. L. Johnson, P. J. McGovern, J. B. Abshire, R. S. Afzal, and X. Sun. Mars Orbiter Laser Altimeter: Experiment summary after the first year of global mapping of Mars. *Journal of Geophysical Research* , 106:23689–23722, October 2001a. doi: 10.1029/2000JE001364.
- D. E. Smith, M. T. Zuber, and G. A. Neumann. Seasonal Variations of Snow Depth on Mars. *Science*, 294:2141–2146, December 2001b. doi: 10.1126/science.1066556.
- D. E. Smith, M. T. Zuber, G. A. Neumann, E. A. Guinness, and S. Slavney. Mars Global Surveyor Laser Altimeter Mission Experiment Gridded Data Record. MGS-M-MOLA-5-MEGDR-L3-V1.0, NASA Planetary Data System, 2003. Available Online: <http://pds-geosciences.wustl.edu/missions/mgs/mola.html>.
- M. Spiegel. *Kombinierte Ausgleichung der Mars Express HRSC Zeilenbilddaten und des Mars Global Surveyor MOLA DGM*. PhD thesis, Technische Universität München, Fakultät für Bauingenieur- und Vermessungswesen, 2007.
- N. Thomas, D. T. Britt, K. E. Herkenhoff, S. L. Murchie, B. Semenov, H. U. Keller, and P. H. Smith. Observations of Phobos, Deimos, and bright stars with the Imager for Mars Pathfinder. *Journal of Geophysical Research* , 104:9055–9068, April 1999. doi: 10.1029/98JE02555.
- P. Thomas. Surface features of PHOBOS and Deimos. *Icarus*, 40:223–243, November 1979. doi: 10.1016/0019-1035(79)90069-1.
- P. Thomas, J. Veverka, J. Bell, J. Lunine, and D. Cruikshank. *Satellites of Mars - Geologic history*, pages 1257–1282. Mars, 1992.
- P. C. Thomas. The shapes of small satellites. *Icarus*, 77:248–274, February 1989. doi: 10.1016/0019-1035(89)90089-4.
- W. Torge. *Geodesy*. Walter de Gruyter, Berlin, New York, 3rd - completely rev. and extended - edition, 2001. ISBN 3-11-017072-8.
- A. G. Tulin. Quasi-synchronous orbits and their employment for the approach of a spacecraft to Phobos. *Cosmic Research*, 45(2):131 – 136, April 2007. doi: 10.1134/S0010952507020062. URL <http://www.springerlink.com/content/m307654157463205>.
- R. J. Turner. A model of PHOBOS. *Icarus*, 33:116–140, January 1978. doi: 10.1016/0019-1035(78)90028-3.
- C. H. Veiga. Phobos and Deimos CCD observations. *A&A* , 487:755–758, August 2008. doi: 10.1051/0004-6361:200809498.
- J. Veverka, M. Noland, C. Sagan, J. Pollack, L. Quam, R. Tucker, B. Eross, T. Duxbury, and W. Green. A Mariner 9 Atlas of the moons of Mars. *Icarus*, 23:206–289, October 1974.
- M. Wählisch, K. Willner, J. Oberst, K.-D. Matz, F. Scholten, T. Roatsch, H. Hoffmann, S. Semm, and G. Neukum. A new topographic image atlas of Phobos. *Earth and Planetary Science Letters*, HRSC special Issue, 2009.

- D. R. Williams. Viking Project Information, 2008. URL <http://nssdc.gsfc.nasa.gov/planetary/viking.html>. Last visited: 07. Aug. 2008.
- K. Willner, J. Oberst, M. Wählisch, K.-D. Matz, H. Hoffmann, T. Roatsch, R. Jaumann, and V. Mertens. New astrometric observations of Phobos with the SRC on Mars Express. *A&A* , 488:361–364, September 2008a. doi: 10.1051/0004-6361:200809787.
- K. Willner, J. Oberst, M. Wählisch, K.-D. Matz, H. Hoffmann, T. Roatsch, R. Jaumann, and V. Mertens. Mars Express astrometric observations of Phobos (Willner+, 2008). *VizieR Online Data Catalog*, 348:80361–+, May 2008b.
- L. Wilson and J. W. Head, III. Dynamics of Groove Formation on Phobos by Ejecta from Stickney Crater: Predictions and Tests. In S. Mackwell and E. Stansbery, editors, *36th Annual Lunar and Planetary Science Conference*, volume 36 of *Lunar and Planetary Inst. Technical Report*, pages 1186–+, March 2005.
- L. Wilson, K. Keil, and S. J. Love. The internal structures and densities of asteroids. *Meteoritics and Planetary Science*, 34:479–483, May 1999.
- S. S. C. Wu, A. A. Elassal, R. Jordan, and F. J. Schafer. Photogrammetric application of Viking orbital photography. *Planetary and Space Science* , 30:45–53, January 1982. doi: 10.1016/0032-0633(82)90071-X.
- W. Zeitler. *Simultane Neuausgleichung des globalen 3D-Mars-Netzes*. PhD thesis, Bayerische Akademie der Wissenschaften, Deutsche Geodätische Kommission, 1999. Reihe C: Dissertationen.

A Shadow Observations

Table 24: Results of the analysis of Phobos' shadow images. Stellar coordinate of Phobos are given with respect to the center of the shadow observation. Coordinates of the observed shadow center are given with respect to the Mars body fixed frame, IAU_MARS.

Image	Time of Observation [UTC]	X [km] w.r.t. IAU_MARS	Y [km]	Z [km]	RA [deg] observed	DEC [deg]
M0401793	1999-08-19T11:11:59.707	-2486.15	2261.25	465.16	96.2762	24.6488
M0401795	1999-08-19T11:12:02.897	-2483.13	2265.38	461.06	96.2763	24.6488
M0403239	1999-08-26T04:00:30.687	2179.51	-2521.99	636.04	100.5773	24.5048
M0403241	1999-08-26T04:00:32.657	2177.28	-2524.04	635.77	100.5773	24.5048
M1500561	2000-05-08T16:50:49.995	1441.69	2993.13	709.74	251.8063	-23.1369
M1500791	2000-05-12T05:08:54.135	770.82	-3245.10	631.98	253.7615	-23.4034
M1501198	2000-05-18T21:54:49.535	-106.67	3358.34	465.44	257.4785	-23.8404
M1600263	2000-06-04T19:44:49.775	1033.82	-3237.92	40.31	266.7687	-24.5324
M1700546	2000-07-22T00:59:14.406	1879.01	-2578.85	-1159.81	291.5705	-23.5799
E0501705	2001-06-18T20:28:01.456	2941.07	-1683.78	178.31	85.1942	24.4551
E1300675	2002-02-08T09:00:10.845	-1288.55	-2576.57	1794.63	225.8929	-17.2514
E1400754	2002-03-13T05:42:42.914	-1268.95	-2994.10	984.64	244.3024	-21.8796
E1601447	2002-05-21T03:37:18.495	-2639.88	-2062.57	-559.56	281.9042	-24.4356
E1701413	2002-06-23T00:16:02.306	-2290.19	-2126.65	-1327.17	298.5000	-22.5857
R0400079	2003-04-02T15:32:19.014	-2806.07	-1722.83	-826.15	64.9100	21.9953
R0401680	2003-04-22T10:18:30.714	-1814.65	2861.96	-247.83	76.3896	23.7219
R0500118	2003-05-02T07:41:28.215	-729.61	-3322.72	49.39	82.3762	24.2765
R1402352	2004-02-22T10:03:29.015	-3321.28	-634.52	269.41	257.7985	-23.8741
R1700528	2004-05-07T01:46:53.115	2145.62	-2321.73	-1235.72	297.0861	-22.8145
h2345_gr	2005-11-10T08:38:33.517	-598.03	2927.12	1598.37	224.2084	-16.7235
h2345_nd	2005-11-10T08:39:26.517	-699.53	2907.04	1593.72	224.2088	-16.7236
h2345_bl	2005-11-10T08:40:24.317	-811.97	2882.49	1584.71	224.2091	-16.7237
h2451_nd	2005-12-10T00:38:59.317	-2099.52	2525.63	845.42	240.8350	-21.1746
h2451_bl	2005-12-10T00:40:06.717	-2213.46	2431.11	833.33	240.8354	-21.1746
h2549_nd	2006-01-06T11:02:50.716	-2594.26	-2179.99	200.04	256.1550	-23.6961
h2549_bl	2006-01-06T11:04:24.916	-2431.66	-2364.40	189.82	256.1556	-23.6961
h2598_nd	2006-01-20T04:15:53.516	155.91	3391.04	-136.86	263.7221	-24.3692
h2729_nd	2006-02-25T20:45:34.415	-3212.96	229.10	-1070.65	283.3454	-24.3479

B Astrometric Observations

Table 25: Observed Phobos astrometric positions between Nov. 16, 2004 and Mar. 29, 2008. Data is archived online (Willner et al., 2008b).

ImageID	Image Time UTC	Observed Phobos position ¹		Error σ [deg]	Spacecraft coordinates ²		
		RA [deg]	DEC [deg]		x [km]	y [km]	z [km]
h1064.0005	2004-11-16T14:21:50.946	128.1825	-32.6734	0.0064	-1389.10	-11517.73	604.70
h1064.0006	2004-11-16T14:22:00.751	128.2033	-32.9930	0.0063	-1380.41	-11510.84	615.04
h1163.0002	2004-12-14T08:05:08.883	151.7854	-24.8394	0.0076	-1684.35	-9665.53	392.82
h1163.0003	2004-12-14T08:05:13.248	151.8718	-25.0207	0.0075	-1679.39	-9661.38	398.24
h1163.0004	2004-12-14T08:05:18.149	151.9776	-25.2221	0.0080	-1673.81	-9656.70	404.33
h2151.0005	2005-09-16T23:24:21.222	311.6387	28.3537	0.0075	4632.53	9039.67	-2290.34
h2381.0005	2005-11-20T09:06:19.796	332.2536	-32.9532	0.0085	5459.94	5823.37	-230.35
h2381.0006	2005-11-20T09:06:24.701	332.4769	-32.7576	0.0085	5450.63	5822.59	-237.49
h2397.0002	2005-11-24T20:38:56.692	30.3706	3.1851	0.0149	5107.98	5581.41	-394.80
h2397.0003	2005-11-24T20:38:59.962	30.4576	3.4449	0.0178	5101.41	5580.75	-399.71
h2446.0004	2005-12-08T13:44:00.307	47.7123	-20.3374	0.0141	5590.41	4984.16	296.15
h2446.0005	2005-12-08T13:44:04.122	47.7351	-19.9902	0.0140	5583.05	4984.55	289.86
h2463.0004	2005-12-13T08:02:51.150	341.4132	-33.1388	0.0079	4779.93	4797.28	-266.33
h2463.0005	2005-12-13T08:02:56.055	341.5824	-32.9380	0.0067	4769.22	4796.98	-274.68
h2487.0003	2005-12-20T01:15:06.755	43.1438	-12.9480	0.0108	5063.02	4532.29	97.71
h2487.0004	2005-12-20T01:15:09.480	43.1534	-12.7516	0.0108	5057.28	4532.63	92.85
h2487.0005	2005-12-20T01:15:12.205	43.1626	-12.5558	0.0108	5051.53	4532.96	88.00
h2487.0006	2005-12-20T01:15:14.385	43.1727	-12.4002	0.0108	5046.93	4533.22	84.11
h2601.0005	2006-01-20T23:07:43.213	104.9109	0.8364	0.0055	5888.36	2962.75	1717.88
h2601.0006	2006-01-20T23:07:49.753	104.9246	1.0678	0.0055	5877.82	2968.71	1704.52
h2601.0007	2006-01-20T23:07:55.507	104.9255	1.2810	0.0055	5868.52	2973.95	1692.75
h2643.0004	2006-02-01T17:26:22.171	30.9473	-53.2045	0.0063	5560.77	2618.83	1650.09
h2643.0005	2006-02-01T17:26:28.166	30.9485	-52.9884	0.0061	5551.04	2625.17	1637.04
h2643.0006	2006-02-01T17:26:33.616	30.9285	-52.7910	0.0060	5542.17	2630.92	1625.17
h2673.0004	2006-02-10T04:40:21.065	179.5426	-31.2876	0.0256	-5357.66	-6052.50	1835.73
h2673.0005	2006-02-10T04:40:24.880	179.5110	-31.5923	0.0135	-5356.55	-6058.46	1842.15
h2739.0004	2006-02-28T16:24:42.868	143.1119	-0.6976	0.0160	-6359.86	-6184.14	1569.33
h2739.0005	2006-02-28T16:24:47.229	143.0556	-1.0774	0.0178	-6359.42	-6190.64	1575.94
h2756.0004	2006-03-05T11:05:35.566	117.7762	-18.1318	0.0074	-6269.17	-7899.87	3395.74
h2756.0005	2006-03-05T11:05:42.106	117.7872	-18.3629	0.0071	-6266.25	-7906.72	3404.44
h2805.0022	2006-03-19T04:19:04.148	103.0179	-9.7457	0.0147	-7415.78	-6926.13	1941.02
h2805.0023	2006-03-19T04:19:07.963	102.9667	-10.0343	0.0147	-7415.32	-6930.87	1946.06
h2805.0024	2006-03-19T04:19:11.778	102.8938	-10.3183	0.0148	-7414.85	-6935.61	1951.10
h2813.0004	2006-03-21T09:58:56.585	91.1272	-5.8741	0.0344	-7574.98	-6345.91	1301.48
h2813.0005	2006-03-21T09:58:58.765	90.9983	-6.2663	0.0345	-7575.05	-6348.86	1304.38
h2813.0006	2006-03-21T09:59:01.490	90.8268	-6.7439	0.0347	-7575.13	-6352.54	1308.02
h2846.0006	2006-03-30T15:54:53.716	69.3914	-2.3372	0.0219	-8153.44	-6620.41	1392.19
h2846.0007	2006-03-30T15:54:57.531	69.2395	-2.7533	0.0230	-8153.48	-6625.14	1396.96
h2912.0004	2006-04-18T03:46:10.245	52.7745	5.6982	0.0120	-9328.87	-6930.90	1385.56
h2912.0005	2006-04-18T03:46:14.605	52.6752	5.4585	0.0120	-9328.74	-6935.47	1390.42
h2912.0006	2006-04-18T03:46:19.510	52.5738	5.1853	0.0130	-9328.57	-6940.60	1395.87
h2979.0005	2006-05-06T23:15:08.280	77.4882	-25.5293	0.0070	-9110.91	-9016.32	4212.27
h2979.0006	2006-05-06T23:15:16.455	77.4682	-25.7499	0.0059	-9105.18	-9019.56	4219.19
h2979.0007	2006-05-06T23:15:24.086	77.4487	-25.9510	0.0062	-9099.82	-9022.58	4225.64
h3005.0005	2006-05-13T23:41:03.708	83.0564	-35.1959	0.0056	-8521.66	-9123.30	4868.87
h3005.0006	2006-05-13T23:41:12.428	83.0599	-35.4198	0.0060	-8513.80	-9125.02	4875.38
h3005.0007	2006-05-13T23:41:21.449	83.0633	-35.6565	0.0054	-8505.66	-9126.80	4882.11
h3310.0003	2006-08-07T10:50:42.982	127.2587	-41.3040	0.0472	-7807.43	-4938.83	2442.99
h3761.0004	2006-12-11T21:23:53.534	298.6407	41.0409	0.0140	7549.34	4383.54	-4445.50
h3761.0005	2006-12-11T21:24:00.075	298.6963	41.4933	0.0143	7548.20	4390.61	-4455.96
h3802.0003	2006-12-23T08:54:31.697	272.4611	19.4971	0.0324	8285.09	3690.14	-3522.08
h3802.0004	2006-12-23T08:54:33.877	272.4388	19.8696	0.0327	8285.30	3692.57	-3525.57
h3835.0005	2007-01-01T14:51:48.802	241.1643	24.9185	0.0229	8879.67	3815.13	-3793.12
h3835.0006	2007-01-01T14:51:52.072	241.0446	25.2913	0.0228	8879.89	3818.46	-3798.00
h3835.0007	2007-01-01T14:51:54.551	240.9497	25.6018	0.0231	8880.05	3820.99	-3801.69
h3843.0003	2007-01-03T20:30:11.752	177.2964	-8.1926	0.0453	8920.86	3203.99	-2933.84
h3843.0005	2007-01-03T20:30:15.567	177.0499	-7.3300	0.0440	8921.90	3208.13	-2939.75
h3868.0003	2007-01-10T20:46:41.277	227.7806	11.1298	0.0296	9470.13	3724.81	-3770.76
h3868.0004	2007-01-10T20:46:45.637	227.6603	11.4982	0.0176	9470.48	3728.97	-3776.91
h3868.0005	2007-01-10T20:46:49.452	227.5328	11.8069	0.0173	9470.79	3732.61	-3782.30
h3876.0003	2007-01-13T02:26:09.255	187.5140	-4.3874	0.0243	9526.38	3217.12	-3055.97
h3876.0004	2007-01-13T02:26:12.525	187.3771	-4.0440	0.0233	9527.19	3220.38	-3060.72

¹Right Ascension and Declination of the COM of Phobos

²Coordinates are in a Mars centered J2000 frame.

ImageID	UTC	RA [deg]	DEC [deg]	σ [deg]	x [km]	y [km]	z [km]
h3999.0003	2007-02-16T13:04:40.907	149.8086	-29.5627	0.0314	11156.09	1601.24	-1196.75
h3999.0004	2007-02-16T13:04:46.902	149.7652	-29.3309	0.0089	11159.41	1606.26	-1204.24
h3999.0005	2007-02-16T13:04:52.352	149.7258	-29.1174	0.0081	11162.42	1610.83	-1211.05
h4030.0003	2007-02-25T02:44:11.994	320.8202	1.8003	0.0053	-1898.53	3627.66	-5935.29
h4030.0004	2007-02-25T02:44:19.080	320.9649	1.7517	0.0047	-1910.75	3619.62	-5923.78
h4030.0005	2007-02-25T02:44:26.710	321.1199	1.6942	0.0049	-1923.89	3610.94	-5911.34
h4030.0006	2007-02-25T02:44:33.795	321.2621	1.6356	0.0028	-1936.09	3602.86	-5899.76
h4233.0004	2007-04-22T21:57:57.424	288.2963	67.4375	0.0288	8163.02	3163.43	-5606.43
h4233.0005	2007-04-22T21:58:02.329	289.0240	67.6260	0.0137	8154.64	3164.97	-5608.84
h4274.0003	2007-05-04T09:26:36.124	217.1465	48.9415	0.0287	9008.54	2448.59	-4709.98
h4274.0004	2007-05-04T09:26:39.394	217.0905	49.4085	0.0380	9003.31	2450.02	-4712.19
h4274.0005	2007-05-04T09:26:42.664	216.9611	49.7652	0.0415	8998.07	2451.45	-4714.40
h4307.0003	2007-05-13T15:21:53.264	264.0226	45.4502	0.0518	8477.59	2172.32	-4435.85
h4307.0004	2007-05-13T15:21:54.899	264.3801	45.7718	0.0498	8474.75	2173.09	-4436.99
h4332.0004	2007-05-20T15:36:40.532	311.8546	3.4649	0.0156	7127.51	2210.46	-4561.29
h4332.0005	2007-05-20T15:36:45.437	312.2594	3.6672	0.0155	7117.39	2212.64	-4564.24
h4340.0002	2007-05-22T21:16:37.067	316.3323	0.7662	0.0409	7916.20	1928.07	-4184.06
h4340.0003	2007-05-22T21:16:39.247	316.7477	1.0399	0.0422	7912.08	1929.19	-4185.65
h4340.0004	2007-05-22T21:16:41.427	317.1484	1.3308	0.0427	7907.96	1930.31	-4187.25
h4340.0005	2007-05-22T21:16:43.607	317.5631	1.6252	0.0412	7903.83	1931.43	-4188.84
h4373.0003	2007-06-01T03:10:19.212	325.0556	-19.9523	0.0225	7391.82	1702.55	-3938.23
h4373.0004	2007-06-01T03:10:22.482	325.4232	-19.7021	0.0359	7385.18	1704.40	-3940.77
h4373.0005	2007-06-01T03:10:25.208	325.7129	-19.4696	0.0224	7379.64	1705.94	-3942.88
h4381.0004	2007-06-03T08:53:36.389	36.5148	-15.5830	0.0332	7765.84	1505.18	-3678.91
h4381.0005	2007-06-03T08:53:39.659	36.4893	-15.0814	0.0330	7759.51	1507.16	-3681.70
h4381.0006	2007-06-03T08:53:42.384	36.4751	-14.6848	0.0692	7754.23	1508.81	-3684.02
h4414.0004	2007-06-12T14:48:07.725	12.4254	-21.5720	0.0193	7081.06	1365.21	-3536.93
h4414.0005	2007-06-12T14:48:11.540	12.5449	-21.2002	0.0193	7072.99	1367.72	-3540.32
h4447.0004	2007-06-21T20:39:46.963	353.9558	-32.1766	0.0142	6665.18	1174.23	-3311.26
h4447.0005	2007-06-21T20:39:51.323	354.1398	-31.8279	0.0140	6655.50	1177.40	-3315.47
h4447.0006	2007-06-21T20:39:55.683	354.3750	-31.5067	0.0379	6645.81	1180.56	-3319.68
h4529.0004	2007-07-14T19:45:40.361	29.3524	-50.0708	0.0104	6852.66	320.69	-2198.98
h4529.0005	2007-07-14T19:45:45.266	29.2921	-49.7403	0.0106	6842.72	325.42	-2205.71
h4554.0004	2007-07-21T19:52:10.155	328.6924	-51.4703	0.0083	6163.92	414.17	-2344.68
h4554.0005	2007-07-21T19:52:15.605	328.9710	-51.1995	0.0083	6151.73	419.71	-2352.31
h4603.0005	2007-08-04T13:09:30.302	17.5712	-55.2927	0.0080	6340.54	-100.53	-1635.39
h4603.0006	2007-08-04T13:09:34.117	17.6098	-55.0862	0.0080	6332.93	-96.16	-1641.79
h4636.0004	2007-08-13T19:01:12.550	357.1142	-52.2496	0.0073	5740.03	-33.98	-1744.24
h4636.0005	2007-08-13T19:01:17.455	357.1997	-51.9947	0.0073	5729.44	-27.94	-1752.92
h4683.0005	2007-08-27T00:30:32.831	115.0865	-11.4895	0.0087	-5970.70	-1887.65	5945.57
h4683.0006	2007-08-27T00:30:38.281	115.2121	-11.6940	0.0078	-5968.49	-1893.23	5956.09
h4765.0005	2007-09-18T23:41:12.487	105.1036	-14.5432	0.0148	-7270.62	-1147.70	5506.05
h4773.0004	2007-09-21T05:22:02.716	126.1768	-5.4310	0.0289	-7383.98	-765.45	4813.81
h4806.0005	2007-09-30T11:17:04.147	90.8387	-21.3317	0.0234	-7902.97	-761.14	5291.77
h4806.0006	2007-09-30T11:17:07.417	90.9174	-21.7457	0.0239	-7903.19	-763.87	5297.70
h4847.0005	2007-10-11T22:52:13.457	36.9478	-20.0376	0.0435	-8510.86	-306.26	4947.29
h4855.0004	2007-10-14T04:32:40.341	300.2336	13.7349	0.0365	-8526.53	50.85	4245.81
h4880.0004	2007-10-21T04:48:20.320	23.3368	-23.4034	0.0225	-9069.69	-205.55	5311.28
h4880.0005	2007-10-21T04:48:24.135	23.1266	-23.8298	0.0227	-9070.23	-208.24	5317.49
h4888.0004	2007-10-23T10:27:01.038	336.6883	8.3632	0.0302	-9076.30	221.71	4445.36
h4888.0005	2007-10-23T10:27:03.763	336.5135	7.9846	0.0263	-9077.20	219.82	4450.01
h4888.0006	2007-10-23T10:27:06.488	336.3443	7.6222	0.0274	-9078.10	217.94	4454.65
h4913.0004	2007-10-30T10:42:21.282	20.3234	-11.0178	0.0158	-9598.79	66.06	5317.12
h4913.0005	2007-10-30T10:42:26.187	20.1643	-11.3761	0.0157	-9599.52	62.86	5324.68
h4913.0006	2007-10-30T10:42:31.092	19.9951	-11.7354	0.0168	-9600.23	59.66	5332.23
h4946.0004	2007-11-08T16:37:39.155	15.5066	-6.2994	0.0123	-10122.24	348.35	5323.79
h4946.0005	2007-11-08T16:37:45.150	15.3436	-6.6117	0.0122	-10123.05	344.71	5332.51
h4946.0006	2007-11-08T16:37:51.146	15.1719	-6.9226	0.0127	-10123.84	341.08	5341.23
h5163.0005	2008-01-08T22:04:48.369	74.9996	-55.7037	0.0110	-8250.21	-626.27	8645.71
h5163.0006	2008-01-08T22:04:54.909	75.2741	-55.8834	0.0073	-8241.37	-630.02	8647.55
h5163.0007	2008-01-08T22:05:01.202	75.5517	-56.0637	0.0076	-8232.86	-633.64	8649.31
h5277.0005	2008-02-10T10:49:22.153	138.4722	-38.3558	0.0104	-5954.93	-396.35	7094.82
h5277.0006	2008-02-10T10:49:28.148	138.8245	-38.3366	0.0092	-5943.32	-400.87	7095.02
h5277.0007	2008-02-10T10:49:33.897	139.1696	-38.3141	0.0095	-5932.17	-405.20	7095.21
h5343.0004	2008-02-29T06:21:50.246	122.3605	-42.9080	0.0265	-7349.07	832.38	5911.57
h5343.0005	2008-02-29T06:21:52.971	122.9079	-42.9952	0.0315	-7344.27	829.96	5912.85
h5362.0002	2008-03-05T16:24:03.621	100.9437	-14.8452	0.0296	-7367.94	1024.35	5597.59
h5362.0003	2008-03-05T16:24:05.801	101.2836	-14.9802	0.0276	-7364.09	1022.33	5598.77
h5362.0005	2008-03-05T16:24:10.161	101.9429	-15.2488	0.0270	-7356.37	1018.30	5601.12
h5381.0003	2008-03-11T02:28:52.671	107.6532	-0.2508	0.0229	-7076.38	1046.22	5390.09
h5381.0004	2008-03-11T02:28:55.396	107.9967	-0.3741	0.0233	-7071.37	1043.57	5391.61
h5381.0005	2008-03-11T02:28:58.121	108.3337	-0.5184	0.0225	-7066.35	1040.93	5393.13
h5447.0005	2008-03-29T22:08:20.194	176.8425	55.2067	0.0269	-7129.70	1672.43	4328.42

C Coefficients of the Spherical Expansion Model

Table 26: Degree and order 17 coefficients

Degree	Order	A [m]	σ_A [m]	B [m]	σ_B [m]	Degree	Order	A [m]	σ_A [m]	B [m]	σ_B [m]
0	0	1.09558E+04	2.62E-02	-	-	12	8	-1.07310E-07	3.37E-11	3.82937E-07	3.71E-11
1	0	-2.33906E-01	2.64E-03	-	-	12	9	4.75823E-09	4.11E-12	-2.55509E-08	3.41E-12
1	1	6.45865E-02	3.19E-03	1.37004E-02	3.91E-03	12	10	-1.12345E-09	5.16E-13	-3.96084E-09	5.13E-13
2	0	-2.10702E+03	4.28E-03	-	-	12	11	5.12734E-10	8.55E-14	5.87398E-10	6.72E-14
2	1	-8.80719E+01	1.89E-03	3.48304E+01	2.14E-03	12	12	2.20024E-10	1.71E-14	-1.08662E-11	1.79E-14
2	2	2.37509E+02	1.31E-03	9.33803E+00	1.36E-03	13	0	-6.88193E+01	6.85E-03	-	-
3	0	3.78374E+02	3.67E-03	-	-	13	1	3.04231E+00	7.09E-04	7.76251E+00	8.24E-04
3	1	2.00756E+02	1.54E-03	-4.75122E+01	2.58E-03	13	2	-6.73685E-02	5.54E-05	-6.82951E-01	5.26E-05
3	2	-6.94972E+01	5.85E-04	8.87794E-01	5.15E-04	13	3	-5.21479E-03	3.83E-06	1.39774E-02	4.43E-06
3	3	-6.09782E+00	2.96E-04	3.31166E+01	3.02E-04	13	4	-3.59686E-04	3.25E-07	-2.22230E-04	3.01E-07
4	0	2.09369E+02	5.17E-03	-	-	13	5	-1.63350E-04	2.68E-08	1.16367E-05	2.66E-08
4	1	-1.10159E+02	1.32E-03	3.77340E+00	1.84E-03	13	6	-9.31787E-06	2.42E-09	3.97858E-06	2.23E-09
4	2	1.01905E+01	4.40E-04	-1.03073E+01	4.30E-04	13	7	-1.04065E-06	1.82E-10	-1.44296E-06	1.96E-10
4	3	5.47072E+00	9.63E-05	-3.70178E+00	1.01E-04	13	8	-1.60405E-08	1.90E-11	-1.28296E-08	1.86E-11
4	4	-1.66095E-01	5.07E-05	7.71780E-01	4.12E-05	13	9	2.55088E-09	1.68E-12	-7.57465E-09	1.58E-12
5	0	4.49442E+02	5.43E-03	-	-	13	10	1.63599E-09	1.62E-13	-1.15883E-09	1.89E-13
5	1	6.48754E+01	1.25E-03	3.44804E+01	1.66E-03	13	11	-7.72687E-11	2.45E-14	7.47623E-11	1.86E-14
5	2	6.18899E+01	2.80E-04	2.78281E+00	2.83E-04	13	12	-5.98392E-12	3.13E-15	2.14947E-11	3.63E-15
5	3	-1.69619E+00	5.92E-05	-3.49146E-01	6.49E-05	13	13	-1.66085E-12	6.30E-16	7.03210E-12	7.46E-16
5	4	-2.97101E-01	1.48E-05	-1.59401E-02	1.11E-05	14	0	4.35613E+01	7.01E-03	-	-
5	5	3.36054E-02	5.88E-06	4.16518E-02	5.55E-06	14	1	-7.79773E-01	6.52E-04	-2.26869E+00	7.62E-04
6	0	-5.53226E+01	6.56E-03	-	-	14	2	-5.15411E-01	4.96E-05	5.00234E-01	4.59E-05
6	1	1.81610E+01	1.06E-03	-1.53709E+01	1.33E-03	14	3	-1.13523E-02	3.44E-06	-2.35845E-02	3.44E-06
6	2	-4.96374E+00	2.24E-04	3.87444E+00	2.07E-04	14	4	-1.62337E-03	2.52E-07	1.74124E-03	2.20E-07
6	3	-5.83753E-01	3.26E-05	8.27838E-01	3.63E-05	14	5	-1.33407E-04	1.93E-08	-6.80948E-05	1.66E-08
6	4	-1.75224E-01	7.67E-06	6.34660E-02	6.03E-06	14	6	2.42169E-06	1.55E-09	-6.76590E-06	1.32E-09
6	5	-9.10983E-03	1.53E-06	7.15908E-03	1.21E-06	14	7	6.58183E-07	1.16E-10	-9.72811E-07	1.03E-10
6	6	-1.42914E-02	4.67E-07	-8.52161E-03	5.64E-07	14	8	-1.05004E-08	9.21E-12	-5.47030E-08	8.51E-12
7	0	-2.35599E+02	6.19E-03	-	-	14	9	-1.11464E-09	8.19E-13	-2.15113E-09	7.64E-13
7	1	-4.85610E+01	1.16E-03	-5.70059E+00	1.31E-03	14	10	2.36835E-10	6.25E-14	1.91064E-10	6.79E-14
7	2	2.05813E+00	1.64E-04	-1.28952E+00	1.52E-04	14	11	-1.37806E-11	7.43E-15	6.93495E-12	6.56E-15
7	3	-1.96094E-01	2.38E-05	-5.20892E-01	2.79E-05	14	12	-5.47691E-12	8.28E-16	5.80531E-13	8.76E-16
7	4	-1.95501E-02	3.81E-06	2.26874E-02	3.31E-06	14	13	-7.45144E-13	1.19E-16	-5.86145E-13	1.26E-16
7	5	-2.50715E-03	6.88E-07	-2.09135E-02	5.70E-07	14	14	-7.64240E-14	2.30E-17	-2.82948E-13	2.35E-17
7	6	1.32989E-03	1.28E-07	1.86883E-03	1.10E-07	15	0	-5.60295E+00	6.77E-03	-	-
7	7	1.31325E-03	5.13E-08	-9.97513E-05	3.22E-08	15	1	-2.45441E+00	6.40E-04	-2.67683E+00	7.39E-04
8	0	-2.18965E+01	6.58E-03	-	-	15	2	-1.48374E-01	4.03E-05	-1.76340E-01	4.13E-05
8	1	1.37907E+01	9.68E-04	-1.75152E+01	1.24E-03	15	3	-1.45855E-03	2.57E-06	4.67504E-03	2.85E-06
8	2	-2.81502E+00	1.26E-04	-2.95128E+00	1.30E-04	15	4	-1.37556E-03	1.95E-07	-1.14607E-03	1.72E-07
8	3	1.74125E-02	1.54E-05	8.17064E-02	1.84E-05	15	5	1.03960E-06	1.33E-08	5.09401E-05	1.16E-08
8	4	2.14595E-02	2.57E-06	-1.16711E-02	2.02E-06	15	6	-5.40273E-07	9.05E-10	-7.42870E-06	8.60E-10
8	5	2.42413E-03	3.20E-07	3.16710E-04	2.72E-07	15	7	-3.43342E-07	6.03E-11	-5.82511E-07	7.00E-11
8	6	7.60126E-04	4.50E-08	2.54701E-04	5.26E-08	15	8	2.74411E-08	4.65E-12	2.04080E-08	4.81E-12
8	7	1.11372E-04	9.26E-09	1.09571E-04	8.23E-09	15	9	8.92864E-10	4.08E-13	4.99247E-10	3.54E-13
8	8	-4.99479E-05	2.83E-09	6.31086E-05	3.02E-09	15	10	-2.26173E-10	3.01E-14	-8.78498E-12	3.46E-14
9	0	1.93807E+02	7.64E-03	-	-	15	11	2.08170E-12	2.68E-15	8.82396E-12	2.39E-15
9	1	6.28388E+00	8.10E-04	-6.51824E-02	1.04E-03	15	12	-7.48654E-13	2.45E-16	-3.78730E-13	2.73E-16
9	2	8.77900E-02	1.10E-04	8.91937E-01	1.18E-04	15	13	1.24488E-13	2.77E-17	-2.87849E-13	3.17E-17
9	3	4.71620E-02	1.08E-05	-8.29072E-02	1.23E-05	15	14	-2.30198E-14	4.04E-18	-7.70635E-15	4.34E-18
9	4	-1.61476E-02	1.65E-06	-1.94782E-02	1.22E-06	15	15	4.38348E-15	9.40E-19	-6.36923E-16	6.43E-19
9	5	-7.17541E-04	1.98E-07	2.51797E-04	1.68E-07	16	0	-2.13064E+00	6.66E-03	-	-
9	6	1.57761E-04	2.04E-08	2.01140E-05	2.17E-08	16	1	-4.57972E+00	5.91E-04	-4.91188E-02	6.95E-04
9	7	-1.98357E-05	3.83E-09	-1.56640E-05	2.87E-09	16	2	-5.17254E-02	3.76E-05	1.22624E-01	3.62E-05
9	8	-3.18102E-06	4.94E-10	4.69289E-06	6.29E-10	16	3	-6.56927E-03	2.11E-06	-3.87900E-03	2.11E-06
9	9	-2.98329E-08	1.73E-10	-9.47182E-07	1.73E-10	16	4	1.19968E-03	1.43E-07	2.70905E-04	1.35E-07
10	0	7.40910E+00	6.32E-03	-	-	16	5	-1.17485E-05	8.70E-09	-1.44344E-05	8.59E-09
10	1	1.91166E+01	9.47E-04	-3.15978E+00	1.12E-03	16	6	2.60990E-06	5.72E-10	-5.76391E-06	5.63E-10
10	2	2.24427E-01	8.73E-05	1.05775E+00	7.80E-05	16	7	1.74110E-07	3.77E-11	-6.34099E-08	3.90E-11
10	3	-6.68241E-02	9.48E-06	-4.39010E-02	1.04E-05	16	8	-1.59538E-08	2.91E-12	9.40549E-09	2.37E-12
10	4	-1.31036E-02	1.01E-06	5.31005E-03	7.73E-07	16	9	-8.77722E-10	1.95E-13	1.79877E-09	1.82E-13
10	5	-3.69993E-04	1.09E-07	-3.95882E-04	1.09E-07	16	10	-1.10841E-10	1.29E-14	-2.14520E-11	1.62E-14
10	6	2.73735E-05	1.10E-08	-2.28392E-04	1.35E-08	16	11	5.58910E-12	1.19E-15	-3.48092E-12	1.12E-15
10	7	-4.71958E-06	1.54E-09	2.32433E-05	1.10E-09	16	12	-2.80690E-13	8.41E-17	1.66621E-13	9.16E-17
10	8	3.65951E-06	1.86E-10	-1.22941E-06	2.05E-10	16	13	-4.44738E-14	8.83E-18	-3.92159E-14	9.06E-18
10	9	-8.98277E-08	3.23E-11	-1.29452E-07	3.21E-11	16	14	2.97992E-16	9.58E-19	3.06475E-15	1.04E-18
10	10	1.37178E-07	7.71E-12	1.46090E-07	1.04E-11	16	15	4.08122E-16	1.45E-19	-2.05937E-16	1.32E-19
11	0	-1.45455E+01	7.32E-03	-	-	16	16	-1.81351E-16	2.21E-20	-5.44637E-17	2.53E-20
11	1	-2.77050E+00	8.31E-04	1.65245E+01	8.80E-04	17	0	1.06715E+01	6.97E-03	-	-
11	2	2.81813E-01	8.05E-05	-5.54202E-01	8.02E-05	17	1	3.17137E+00	5.02E-04	-7.45018E-01	6.04E-04
11	3	-4.83176E-02	6.28E-06	8.33467E-02	6.54E-06	17	2	-8.17169E-03	3.46E-05	-2.63351E-01	3.27E-05
11	4	7.93013E-04	8.18E-07	-9.66135E-03	5.96E-07	17	3	-1.86805E-03	1.65E-06	2.12420E-03	1.84E-06
11	5	-2.02910E-04	6.02E-08	-2.93989E-04	6.27E-08	17	4	3.41733E-04	1.00E-07	3.36152E-04	1.07E-07
11	6	3.26150E-05	6.42E-09	-6.19103E-05	7.64E-09	17	5	3.40036E-05	6.55E-09	-4.58320E-05	6.51E-09
11	7	1.61631E-06	7.33E-10	2.87121E-06	6.58E-10	17	6	2.52123E-06	3.76E-10	5.72466E-07	3.81E-10
11	8	-1.46625E-06	6.69E-11	2.80994E-07	8.24E-11	17	7	1.39415E-08	2.26E-11	-5.42432E-08	2.64E-11
11	9	4.64073E-08	1.15E-11	6.84893E-08	9.68E-12	17	8	-2.48253E-09	1.56E-12	5.76176E-09	1.48E-12
11	10	-7.47243E-09	1.66E-12	-8.02677E-09	1.73E-12	17	9	4.00201E-10	1.04E-13	7.07754E-10	1.01E-13
11	11	-3.87837E-09	4.72E-13	-8.34497E-10	3.58E-13	17	10	-2.13416E-11	6.74E-15	-2.94269E-11	7.69E-15
12	0	-8.01368E+01	7.19E-03	-	-	17	11	-1.87566E-12	5.16E-16	-1.01507E-12	5.21E-16
12	1	-2.07918E+00	6.87E-04	-5.12979E+00	8.97E-04	17	12	7.47835E-14	3.73E-17	5.01437E-13	4.02E-17
12	2	-1.03030E-02	6.57E-05	8.03371E-01	6.54E-05	17	13	-1.83191E-14	2.90E-18	-7.11674E-15	2.89E-18
12	3	-3.43199E-03	5.33E-06	-2.18611E-02	4.97E-06	17	14	8.51255E-16	2.63E-19	-4.47586E-16	2.89E-19
12	4	3.72458E-04	4.75E-07	-1.15788E-03	4.03E-07	17	15	-1.99510E-17	3.05E-20	1.02616E-16	2.95E-20
12	5	1.12960E-05	4.15E-08	-1.90445E-04	4.18E-08	17	16	-1.56652E-17	3.71E-21	1.35390E-17	3.94E-21
12	6	-1.70696E-05	3.41E-09	3.7716E-05	3.56E-09	17	17	5.32980E-18	6.		

D Phobos Map

The map sheets of the Phobos atlas, which were produced during this study, are exemplarily displayed on the next pages. A full resolution printout results in map sheets of 1,000 mm width and 800 mm height with an acceptable print scale of 3.7 pixel/mm. Surface features were named according to the IAU nomenclature.

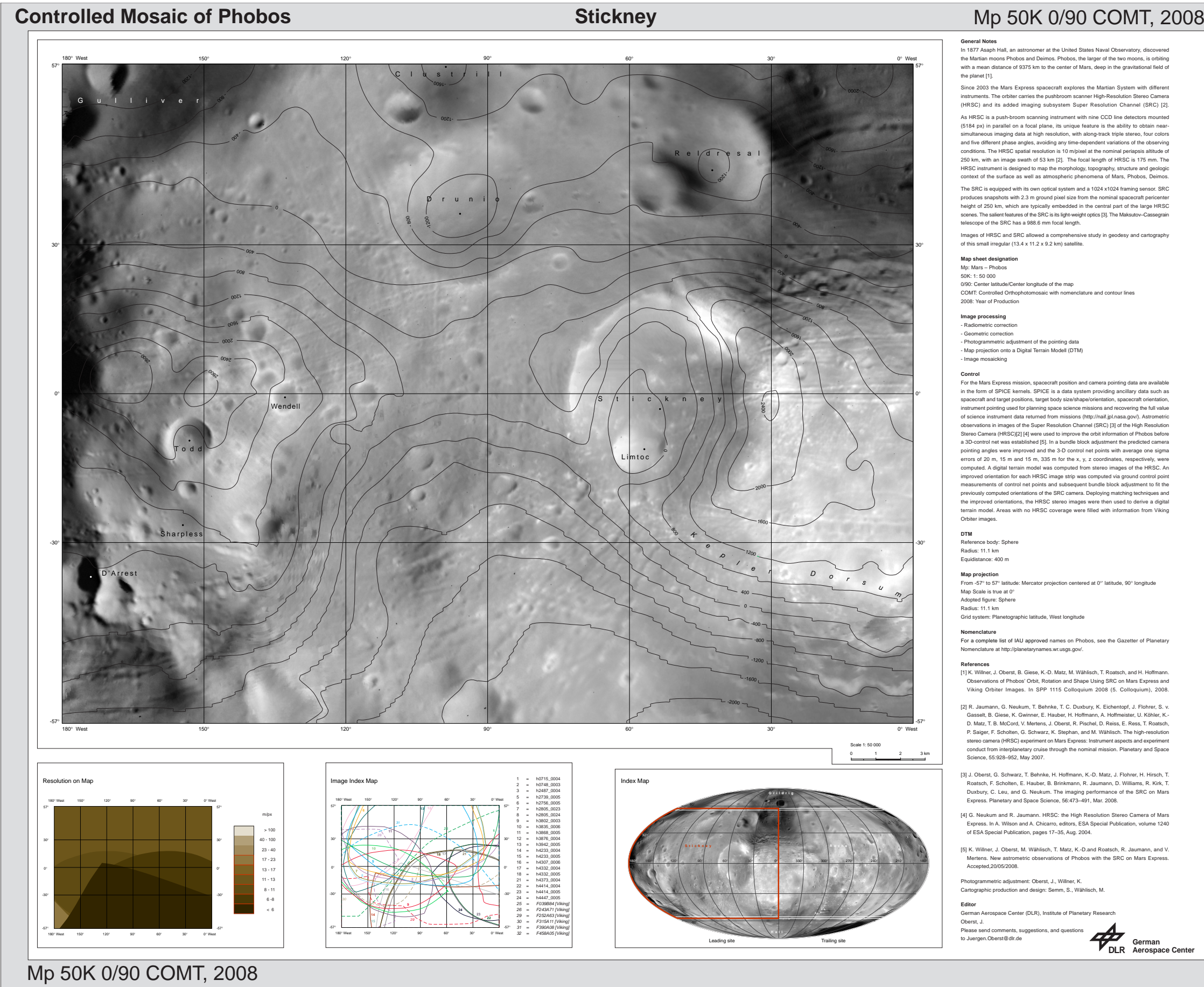


Figure 41: Map Stickney showing the leading side of Phobos from 0° to 180° West in the central latitudes.

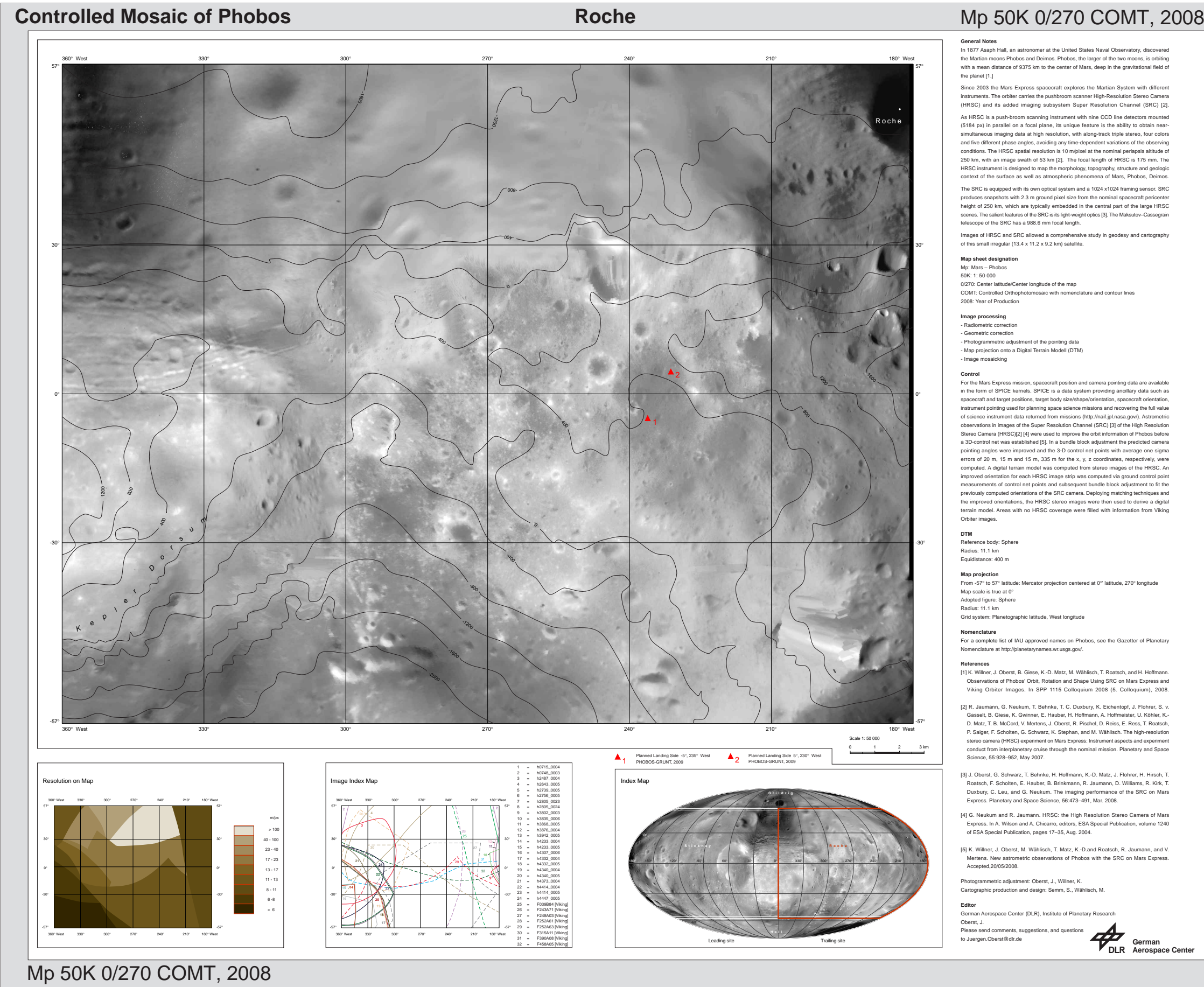


Figure 42: Map Roche showing the trailing side of Phobos from 180° to 360° West in the central latitudes.

